ABSTRACT

PORE STRUCTURE OF OPAL-CT AND QUARTZ PORCELANITES,

MONTEREY FORMATION,

CALIFORNIA

By

Tesfalidet G. Kassa

August 2016

Secondary and backscattered electron scanning electron microscopy of argon-ion polished or focused-ion beams' cut surfaces reveal significant differences in pore size, shape and complexity between opal-CT and quartz-phase porcelanites, but also between rocks of the same silica phase with distinct silica content or sedimentary fabric. Previous studies of these important petroleum reservoir rocks measured an order-of-magnitude lower permeability in opal-CT than quartz-phase porcelanites. Detrital-poor quartz-phase porcelanite (> 80% silica) has massive or laminated microfabrics. The massive type consists of low-porosity matrix and high-porosity lenticular patches with 17-20% bulk porosity. In contrast, a laminated detrital-poor porcelanite (26% bulk porosity) has ~100 µm-thick layers that alternate between well connected, highly porous (35% and low-porosity layers (19%) with isolated pores. Massive detrital-rich porcelanites have porosity of 10% with and poor connectivity.

Opal-CT porcelanites also have two detrital-poor (>75% silica) and one detrital-rich (<60% silica) microfabrics. One detrital-poor porcelanite with 30% bulk porosity

has a pervasive lepispheric fabric in which lepispheric cores and interlepisphere porosity each comprise ~1/2 of the total porosity (3-138 nm size). Lepisphere core are mostly isolated by a surrounding, virtually pore-free, impermeable mantle. The larger and better-connected interlepisphere pores are formed by larger, crosscutting and radiating bladed crystals. The detrital-poor, opal-CT porcelanite is characterized by extraordinarily large and connected vuggy pores with bulk porosity of 60%. This unique pore structure is associated with silica mobility during stalled burial or tectonic uplift of the opal-CT to quartz transition zone. The third fabric is in detrital-rich opal-CT porcelanite that has 18% bulk porosity with poorly connected pores.

PORE STRUCTURE OF OPAL-CT AND QUARTZ PORCELANITES, MONTEREY FORMATION, CALIFORNIA

A THESIS

Presented to the Department of Geological Sciences

California State University, Long Beach

In Partial Fulfillment

of the Requirements for the Degree

Master of Science in Geology

Committee Members

Richard J. Behl, Ph.D. (Chair)
Gregory J. Holk, Ph.D.
Robert D. Francis, Ph.D

College Designee:

Stanley C. Finney, Ph.D.

By Tesfalidet Ghirmay Kassa

M. Sc., 1984, St. Petersburg State Mining Institute, Russia

August 2016

ACKNOWLEDGEMENT

First and foremost, I would express my deepest appreciation to my committee chair, Professor Richard J Behl (CSULB), who supervised my research-work by giving advice and guiding my thesis progress to the end. He taught me the complex nature of Monterey Formation and introduced me to the problem of permeability and the puzzle of porcelanite rocks in petroleum industry. It would have been difficult to accomplish this research without his immense knowledge, continuous guidance and persistent motivating me to tackle the challenges faced in the research.

In addition, my sincere thanks go to my committee members, Professor Gregory J. Holk and Professor Robert D. Francis (CSULB), who provided support to accomplish the research. They allocated time and effort to review my manuscript and share their knowledge and feedback.

I would also express thanks to the University of Southern California (USC) for their laboratory access to use CEMMA - Center of Electron Microscopy and Microanalysis. Particularly, thanks to Ian R. Mcfarlae for assisting in imaging and advising me to use Focused Ion Beam for sample preparation specifically to my porcelanite samples.

I would express my deepest gratitude to the University of University of California Irvine (UCI) which allowed us to use their laboratory: LEXI - Laboratory of Electron and X-ray Instrumentation. Furthermore, I would like to extend my gratitude to Doctor Jian-Guo Zheng, (Director of Irvine Materials Research Institute-UCI) and Timothy James

Montalbano for solving some of the problems we faced in preparation of highly polished samples. Particularly, I am indebted to Timothy for helping me in sample preparation and imaging.

I would like to thank Boeing Corporation for preparing our sample for imaging and micro-analysis. Their instrument assisted us to get highly polished samples with large cross-section and minimum defect which was helpful to acquire the research objective. In particular I am indebted to Paul H. Devaries for preparing highly polished specimens.

Last and not the least, I would express my deepest appreciation to the MARS Project affiliates for support with resources and knowledge which made this research to materialize.

TABLE OF CONTENTS

Page

CHAPTERS Page

LIST OF TABLES

TABLE Page

TABLE Page

LIST OF FIGURES

FIGURE Page

FIGURE Page

FIGURE Page

FIGURE Page

FIGURE Page

CHAPTER 1

INTRODUCTION

Hydrocarbon production from unconventional reservoirs, commonly referred to as shales, has transformed petroleum geology with the use of advanced technology such as horizontal drilling and hydraulic fracturing. Not only has this new source of fossil fuels impacted national and global economics, but it has even had a substantial impact on reducing greenhouse gas emission in the United States by making it economically advantageous to replace coal with shale-hosted natural gas for generation of electrical energy. These unconventional reservoir rocks are characterized by very low permeability and the matrix-related micro- and nanoporosity of these rocks is the main pore system for storage and permeability in these types of reservoirs. The unique characteristics of these pore systems require understanding and characterizing pore-size, connections and tortuosity in a quantitative sense. Traditional methodologies used for conventional reservoir rocks (sandstone or limestone) are insufficient to characterize this microporosity system and consequently, much research has been carried out to develop new methodologies. In particular, Focused Ion Beam and Argon Ion Milling techniques have been used to successfully prepare highly polished surfaces suitable for high-resolution scanning electron microscopy to image and quantify submicron-scale (nanoscale) features. Most of the new work has been accomplished on organic-rich siliciclastic, sparsely siliceous, or calcareous mudstone/shales in North America (e.g., Loucks et al., 2009, 2010; Jobe, 2014). These workers have been able to characterize and compare

Bulk porosity data obtained by mercury or nitrogen gas porosimetry with quantitative microanalysis of porosity by scanning electron microscopy. However, very little work has been done in the highly siliceous rocks of the important reservoirs of the Monterey Formation of California in spite of the oil potential of the siliceous "shale" reservoirs of the Monterey being estimated to be 10 billion barrels of oil in place, with 7 billion barrels in the onshore San Joaquin Basin (SJB) alone (Toronyi, 1997; Montgomery & Morea, 2001). This study focuses specifically on highly siliceous "porcelanite" rocks that form important fractured and matrix reservoir rocks in the Miocene Monterey Formation. These are unusual, high-porosity, low-permeability rocks that altered from originally diatomaceous sediment by a multi-step diagenetic pathway.

The objectives of this study are:

Develop an effective petrographic method for high-resolution, high-quality imaging of pores.

Characterize and quantify the size, shape and distribution of pores in porcelanites of different silica phases and compositions.

Assess what porosity is isolated and ineffective.

The Monterey Formation and equivalent facies that extend along the Pacific Rim accumulated during the middle to late Miocene from ~ 17 to 5 Ma (Bramlette, 1946; Ingle, 1981b; Barron, 1986, Behl, 1999). The widespread Miocene Monterey Formation has a uniquely characteristic biosiliceous and organic-matter-rich composition. It is the main petroleum source rock in California (Bramlette, 1946; Taylor, 1976) as well as an important reservoir rock in some oil fields.

After deposition and accumulation, with sufficient time or burial depth, the diatomaceous sediments underwent two distinct steps of diagenetic transition that altered porosity, permeability, density, brittleness and other properties. The extent and timing of the transformations from highly soluble biogenic silica through a metastable silica phase to stable quartz are influenced by many compositional and environmental factors, but result in increasingly dramatic changes in porosity and permeability (Isaacs 1981; Chaika & Dvorkin, 2000; Eichhubl & Behl, 1998; Schwalbach et al., 2009).

Burial diagenesis of carbonate-free, highly diatomaceous sediments and their diagenetic equivalents result in a stepwise reduction in porosity from 60-65% in diatomaceous rocks to 25-35% in opal-CT-phase rocks to 10-15% in equivalent quartz-phase rocks (Isaacs, 1981). Porosity loss is directly related to the two-step diagenetic transformation of silica at different depths, occurring primarily by compaction associated with silica dissolution and reprecipitation beneath a lithostatic load.

Schwalbach et al. (2009) observed that mercury injection capillary pressure tests indicate higher permeability in quartz porcelanites despite the reduction in matrix porosity during the final phase change from opal-CT to quartz. This study measured an order-of-magnitude lower permeability in opal-CT compared with quartz phase porcelanites. These findings are critically important to understanding and exploiting petroleum reservoirs. Discovery of this unexpected inverse relationship between porosity and permeability in opal-CT and quartz-phase porcelanites was the primary motivation for this thesis study.

In this study, we identify and quantify significant differences in pore size, shape and complexity between opal-CT and quartz-phase porcelanites, but also between rocks

of the same silica phase with distinct silica content or sedimentary fabric using secondary and backscattered electron scanning electron microscopy. With specimen surfaces prepared by argon-ion milling or focused-ion beams it is possible to identify features of pores at the micron to 10's of nanometer scale. This study identifies 3 distinct pore microfabrics in both opal-CT and quartz-phase porcelanites. We measurably demonstrate that lower-porosity quartz-phase porcelanites actually contain larger (but fewer) pores. We document distinctions in pore shapes between rocks of different phase and composition. We also discovered and describe a unique pore fabric that relates to the crystal growth structure of opal-CT that renders much of the porosity inaccessible and ineffective. Finally, we identify a previously unrecognized vuggy dissolution pore fabric related to a complex burial and uplift history not uncommon in tectonically active California.

CHAPTER 2

BACKGROUND

2.1 Monterey Formation

The extensive Miocene Monterey Formation is unique in its highly biosiliceous lithologic character (Bramlette, 1946). It extends inland and along the coast of California with bathyal depocenters in which the Monterey sediments accumulated (Figure 2.1.) (Ingle, 1981a), and is the main petroleum source rock in California (Bramlette, 1946; Taylor, 1976) as well as vital reservoir rock in some areas. Its distinctive lithology and prolific source rocks have made the formation the focus of much study and research (Behl, 1999). The organic-rich Monterey Formation and its equivalent facies that extend along the Pacific Rim accumulated during the middle and upper Miocene from ~ 17 Ma to 5 Ma (Bramlette, 1946; Ingle, 1981b; Barron, 1986). The deposition of these rocks reflects many complexly interrelated climatic, paleoceanographic and tectonic events and conditions. The Monterey Formation was deposited following a major change of plate motion from subduction to transform motion (Atwater, 1970; Blake et al., 1978). Deposition of the Monterey and related formations spanned the Middle Miocene onset of glacial climate that resulted in increased coastal upwelling, enhancing the production of abundant diatoms that accumulated in small, simultaneously formed basins (Ingle, 1981ab). In addition, deposition of the Monterey and its equivalents also coincided with a major switch in marine thermohaline circulation that shifted siliceous deposition from

the North Atlantic to North Pacific oceans and Cenozoic cooling associated with expansion the global cryosphere (Barron, 1986; Behl, 1999).

In many places, the highly siliceous sediments of the Monterey Formation have undergone two steps of diagenetic transformation with time, burial and tectonic deformation that have important effects on rock porosity, permeability, density, brittleness and other properties. These alterations from highly reactive biogenic silica of opal-A to metastable opal-CT to stable quartz are related to many factors and resulted in increasingly modified porosity and permeability depending on composition and phase of the diagenetic rocks (Isaacs, 1981; Chaika and Dvorkin, 2000; Schwalbach et al., 2009). The highly siliceous rocks of Monterey Formation – porcelanite in particular – are important reservoir rocks in some parts of California and the understanding the controls of porosity and permeability of these rocks is critical for petroleum industry.

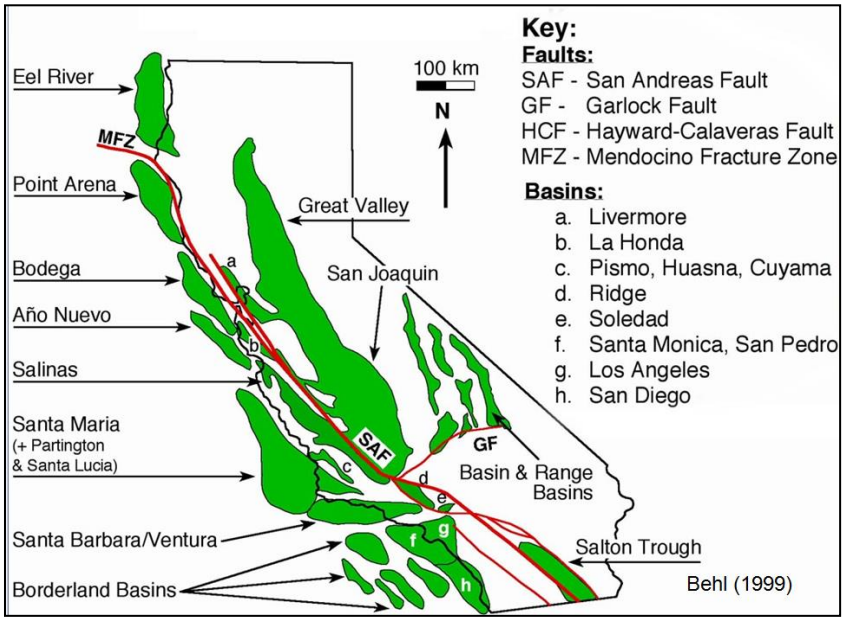

FIGURE 2.1. Present location of Neogene depocenters or sedimentary basins (from Behl, 1999: after Biddle, 1991; Dunkel and Piper, 1997).

2.2 Geologic Setting

Deposition and accumulation of the Monterey Formation and related facies was along the California margin and especially in Neogene basins that formed during the change from a convergent to transform plate margin in California (Taylor, 1976; Ingle, 1981a). The North American Plate came into contact with the spreading ridge system separating the Pacific and Farallon plates at about 29 Ma (Atwater, 1970; Atwater and Molnar, 1973). According to these workers, the onshore and central California basins formed during the tectonic reorganization due to the interception of the Pacific-Farallon plate boundary by the North American plate. Changes of azimuth of relative shear between the Pacific and North American plates through the Neogene resulted in the formation of many Neogene basins, with initial subsidence occurring primarily between ~21-15 Ma, especially in offshore northern and central California (Atwater and Molnar, 1973; Atwater, 1989; Atwater and Stock, 1998). Blake et al. (1978) give detailed description of the formation of the onshore and central California basins and suggest that formation of the Neogene basins could be due to either the contact of the spreading-ridge and the continental margin or by changing plate motions after this contact occurred, or a combination of both phenomena. Furthermore, Nicholson et al. (1994) interpreted the role of microplate formation and capture in the process of tectonic reorganization and basin formation.

With the exception of basins associated with the Western Transverse Ranges, many of the Neogene basins now form an elongated and sub-parallel pattern that may have resulted from combination of pre-Miocene geologic structure, extensive drag effects related to right-lateral movement along the San Andreas fault system and to northeast-

southwest oriented shortening since their formation (Blake et al., 1978). According to these authors, the onshore Santa Maria basin, in which the samples were collected, was formed between the present-day Coast Ranges and Western Transverse Ranges, and consequently includes both northwest-southeast and east-west structural elements consistent with its intermediate position. Furthermore, the Neogene basin initiated as a rift valley that subsided during middle to late Miocene time with regional marine transgression in early middle Miocene, and progressing to an increasing rate of tectonic plus sediment-load subsidence during the Pliocene. This basin with a Neogene thickness of 4,500 meters of marine strata unconformably overlies Franciscan basement with nonmarine units at the top and bottom of the succession. Wide, open folds related to the right–lateral movement on a major fault zone developed in late Quaternary. The petroleum of this basin accumulated in large closed anticlines mostly in fractured chert, porcelanite, and dolostone of the Miocene Monterey Formation (Tennyson & Isaacs, 2001).

The Santa Lucia Bank and Hosgri faults bound the offshore Santa Maria basin (Woodring and Bramlette., 1950). Isolation of the basin related to the uplift of the Santa Lucia Bank (Hoskins and Griffiths, 1971), with thick accumulations of sediment in the structurally isolated lows.

2.3 Stratigraphy and Lithology

The Monterey Formation and related facies form an extensive, irregular and discontinuous blanket of Neogene siliceous (diatomaceous) sediments along the north Pacific Rim including parts of Mexico, the western side of the USA and Canada, the Bering Sea, and Sakhalin Island south to Japan and Korean Peninsula (Ingle, 1981b).

The distal and bathyal Pacific Neogene diatomites imply similar Neogene paleoenvironmental and tectonic histories around much of the north Pacific margin as they generally occur in similar stratigraphic sequences of shelf, slope, and basin lithofacies (Ingle, 1981 ab) (Figure 2.2.). Most have been affected to some degree by diagenetic transformation of silica with the lower strata of the diatomite changed to porcelanite and chert due to burial and thermal histories (Bramlette, 1946; Murata and Larson, 1975; Isaacs, 1980; Pisciotto, 1981). There is some variation between regions, but in California, the Monterey Formation is composed chiefly of interbedded limestones, dolostones, mudstones, shales, and, most characteristically, siliceous rocks (chert, porcelanite, and siliceous mudstone) (Bramlette, 1946; Behl, 1999) which were deposited in largely anoxic basins (Pisciotto and Garrison, 1981). Lithological composition varies

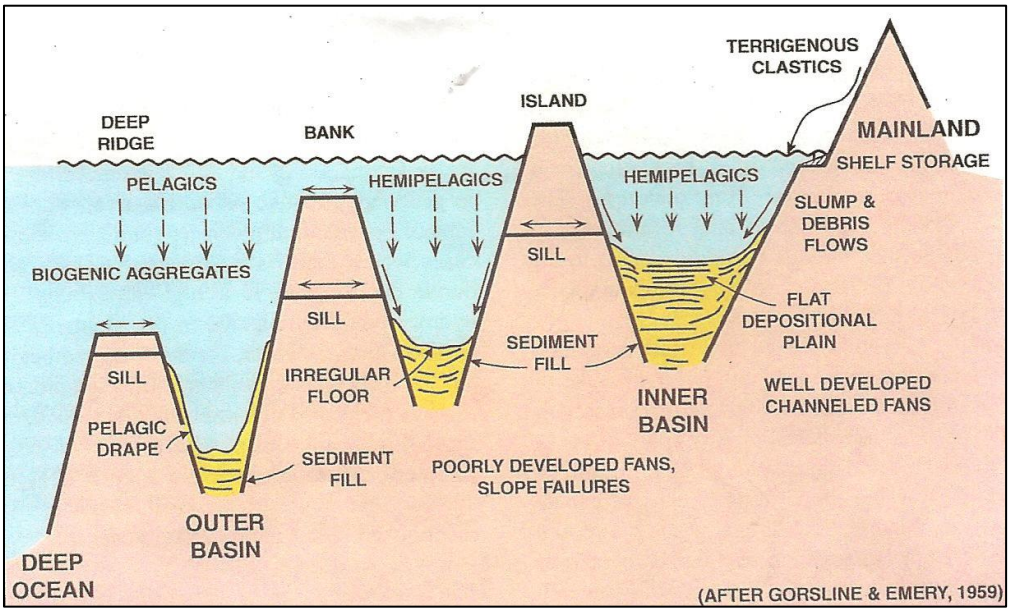

FIGURE 2.2. Schematic cross section of margin configuration of the California Continental Borderland after Gorsline and Emery (1959). Blake (1981) suggested this topographic arrangement could account for many of the characteristics of Monterey Formation depositional systems.

even within a single stratigraphic interval (Isaacs, 1981) yet there are large-scale vertical and lateral compositional trends that permit subdivision into informal members (Pisciotto and Garrison, 1981). However, the siliceous rocks are the most characteristic of the Monterey Formation.

Pisciotto and Garrison (1981) recognized three major consecutive basinal lithofacies in the Monterey Formation succession throughout the central and southern coast of California (Figure 2.3). They consist of: a calcareous facies at the base, a phosphatic facies in the middle, and a siliceous facies at the top. This vertical succession of basinal lithofacies of the general Neogene Monterey Formation sequence in the Coast Ranges is not developed everywhere, and in some places, such as near Santa Maria, the middle Monterey phosphatic interval is also associated with abundant chert (Pisciotto and Garrison, 1981; Behl and Garrison, 1994) and has been further divided into additional lithostratigraphic members (MacKinnon, 1989) (Figure 2.4).

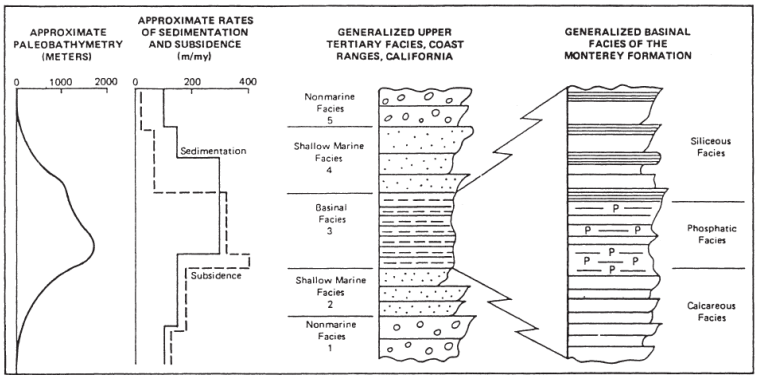

FIGURE 2.3. Generalized upper Tertiary sedimentary facies of the California Ranges, showing the position and facies of the Monterey Formation (Pisciotto and Garrison, 1981).

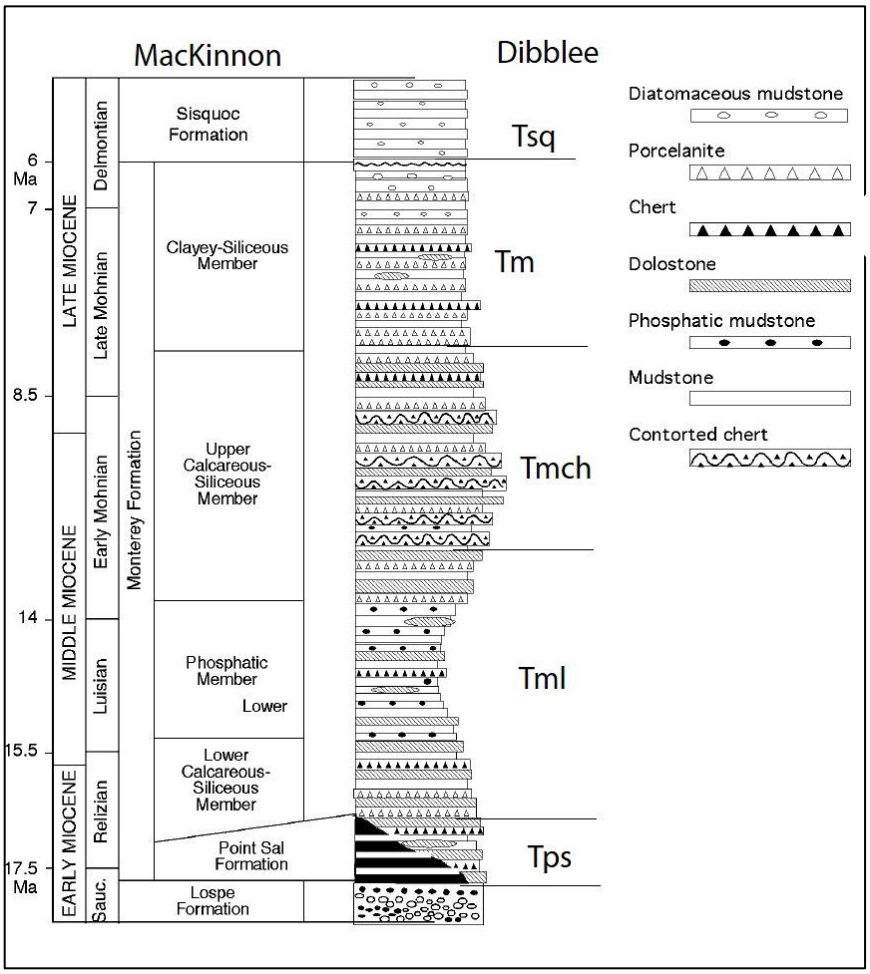

FIGURE 2.4. Composite geologic column and stratigraphic subdivision of the Monterey Formation for the coastal Santa Maria-Lompoc area. Modified from Mackinnon (1989) by Ijeoma (2014) and correlated to Dibblee (1989 ab).

This general sequence of lithofacies is related to changing paleoclimatic and paleoceanographic conditions during the Miocene that occurred simultaneously with basin formation, allowing for their deposition, accumulation and preservation (Pisciotto and Garrison, 1981).

2.4 Calcareous Facies

The middle Miocene was marked by a major global warming and high sea level rise, resulting in the flourishing of calcareous plankton (Barron, 1986); this led to the

formation of the basal calcareous facies (Pisciotto, 1981; Pisciotto and Garrison, 1981). According to Pisciotto (1981), the calcareous facies of the Santa Maria area corresponds approximately with the Dark Brown, Oil Sand, and Siltstone and Shell zones of Canfield (1939) and to the lower member of the Monterey Formation and Point Sal Formation as described by Woodring and Bramlette (1950) (Figure 2.3). This facies primarily consists of massive to thin-bedded foraminiferal and coccolith mudstone and shale together with bedded and concretionary carbonates (limestone or dolostone) and some sandstone beds (Woodring and Bramlette, 1950; Pisciotto, 1981). The calcareous facies of the Monterey Formation is underlain by the marine Point Sal Formation in the Santa Maria basin. Although a separate lithostratigraphic unit in formal nomenclature, this formation is actually a more clastic-rich version of the lower calcareous Monterey facies and is considered part of it by Pisciotto and Garrison (1981).

At the well-studied Lion's Head section, a few miles from the area of this study, the upper part of the calcareous facies is exposed and consists of shale with limestone /dolostone layers and concretions, phosphatic layers and porcelaneous shales (Pisciotto, 1981).

2.5 Phosphatic Facies

According Pisciotto (1981), the phosphatic facies correlates to the Bentonitic-Brown, and upper part of the Dark Brown zones of (Canfield, 1939) and to the upper part of the lower member of the Monterey Formation of Woodring and Bramlette (1950). Pisciotto (1981) described that the main constituents of this facies are phosphatized foraminifer and coccolith mudstone and shale. Cryptocrystalline carbonate-fluorapatite

layers and blebs form the phosphate. The contacts with the lower calcareous and upper siliceous facies are gradational.

Pisciotto (1981) described the rocks in Santa Maria at Lion's Head. The common rocks are phosphatic shales with abundant dolostone that grades upwards to interbedded organic-rich shales and contorted and brecciated quartz cherts. As elsewhere in the Santa Maria and other basins, the phosphatic facies are locally associated with cherty rocks as both accumulate in sediment-starved environments (Behl and Garrison, 1994).

2.6 Siliceous Facies

According Pisciotto (1981), the siliceous facies correlates approximately with the Arenaceous and Cherty zones of Canfield (1939) and with the middle and upper member of the Monterey Formation of Woodring and Bramlette (1950). This facies consists of diatomites, diatomaceous shales, siliceous shale, porcelanites and cherts with sparsely distributed authigenic carbonate layers and concretions (Woodring and Bramlette, 1950). The massive, thinly bedded or laminated diatomaceous rocks stratigraphically overlie their diagenetic equivalents - porcelanite and chert (Pisciotto, 1981).

2.7 Silica Diagenesis

The siliceous rocks (diatomite, chert, porcelanite, and siliceous mudstone) are most characteristic of the Monterey Formation. The diagenetic transformations of the siliceous beds undergo various complex alterations with time, burial and tectonic deformation. The rate and timing of these transitions are related to many factors, including bulk sediment composition, pore-water chemistry, water-rock ratio, and permeability (Kastner et al., 1984; Eichhubl and Behl, 1998).

With burial, there are two steps of crystallographic alteration of the diatomaceous rocks: from opal-A (x-ray-amorphous, hydrous silica) to diagenetic opal-CT (hydrous silica of cristobalite and tridymite structure) and from opal-CT to quartz (Isaacs, 1981; Pisciotto and Garrison, 1981; Behl and Garrison, 1994) (Figure 2.5.). The main controlling factors for their transformation are temperature and burial depth within ranges of ~40-50 °C and ~0.5-2 km from opal-A to opal-CT, and ~65-80 °C and ~1.5-3 km for opal-CT to quartz (Murata and Nakata, 1974; Isaacs, 1981; Pisciotto, 1981), bulk composition (Isaacs, 1982; Behl and Garrison, 1994), and rock properties porosity and permeability (Behl, 1998; Eichhubl and Behl, 1998). The diagenesis of the purest siliceous sediments that will form cherts occurs distinctly earlier than for porcelanites at the range of 2-33 °C and 36-76 °C for both steps of diagenetic silica transformation (Behl and Garrison, 1994).

The silica phase transition zone can form a thick interval of interbedded lithologies of different silica phases within a single stratigraphic sequence (Isaacs, 1982). Furthermore, lateral change in sediment accumulation & burial depth, geothermal gradient or tectonic deformation, can make boundaries between silica phase zones locally discordant to stratigraphy (Figure 2.6.); (Bramlette, 1946; Murata and Larson, 1975; Pisciotto, 1981).

Pores in the opal-CT stage are totally intercrystalline with morphologies defined by the equant to bladed crystal shapes and their angular intersections. As noted by many previous workers (see review in Hesse and Schalcht, 2011), opal-CT in detrital-poor siliceous rocks can form lepispheres (i.e., spheres of twinned and cross-cutting bladed crystals). Previous characterizations were based on SEM images of the outer bladed

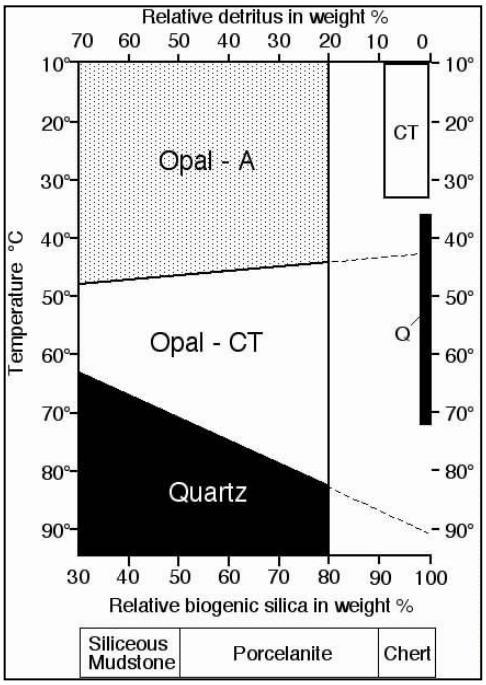

FIGURE 2.5. Diagram showing the relative timing and temperatures of silica phase changes. From Behl and Garrison (1994) after Behl (1992) as modified from Keller and Isaacs (1985) to include data on the purest diatomites and cherts.

surface texture of lepispheres in broken rocks (Figure 2.7). This characterization is limited to the surface of the lepisphere, necessitating the internal structural investigation undertaken by this study.

The diagenetic transition of porcelanite from opal-CT to quartz affects the physical and chemical properties of petroleum reservoir rocks, especially porosity and permeability. These alterations are influenced by many factors, but especially sediment composition, pore-water chemistry and water-rock ratio. During both of the dissolution-precipitation steps, the collapse of the porous framework decreases porosity and results in an abrupt increase of bulk density. Overall, there is a release of structural water from recrystallization of both silica (Eichhubl and Behl, 1998) and smectite clay (Burst, 1969)

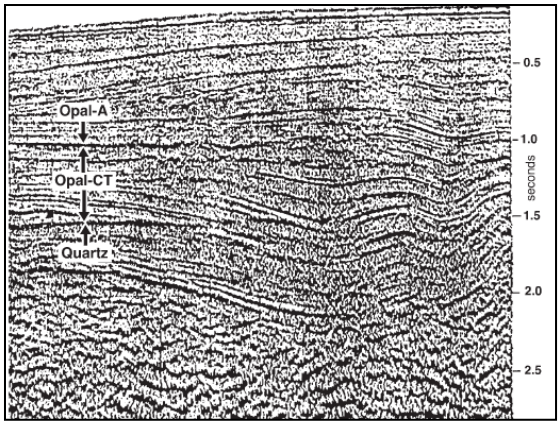

FIGURE 2.6. Seismic-reflection profile showing the near-horizontal opal-A to opal-CT to quartz phase transition that crosses stratigraphy (After Crouch, Bachman, and associates, 1991).

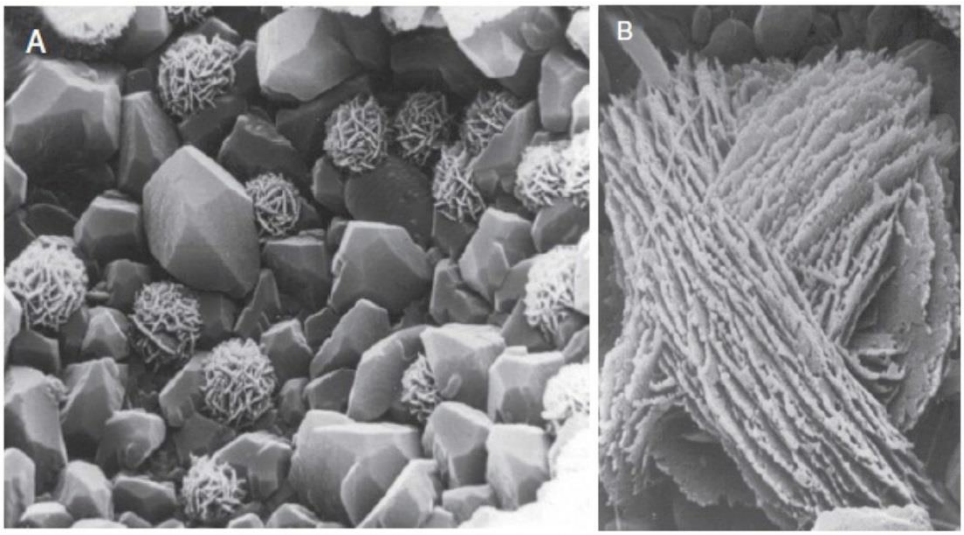

FIGURE 2.7. Images of opal-CT porcelanite lepispheres, modified from Florke et al., (1976). (A) Small opal-CT lepispheres (2-3 μm in diameter) growing on euhedral calcite in cavity of foraminifera in partially silicified chalk. (B) Opal-CT blades (~ 1 μm in length) of juvenile lepisphere displaying twinning angle of 70^0 C.

during burial. Furthermore, there is a release of water, CO_2, liquid hydrocarbons and natural gases during diagenesis and catagenesis of organic matter. Although, there is a

decrease of porosity during the transformation of opal-CT phase porcelanite to quartz phase, there is an increase of permeability (Figure 2.8.) (Schwalbach et al., 2009).

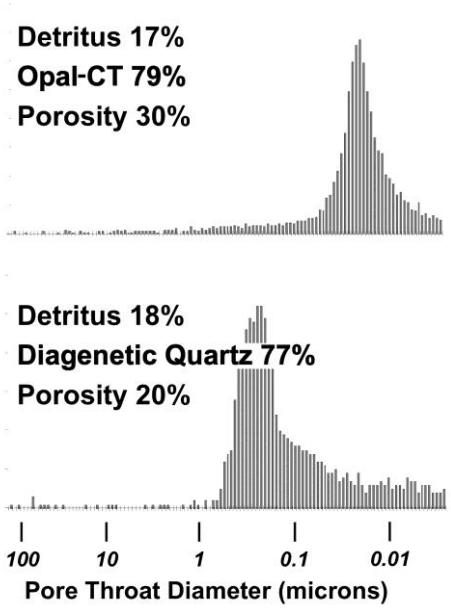

FiGURE 2.8. Pore-size distribution data derived from capillary pressure mercury injection tests of similar low-detritus composition porcelanite (Schwalbach et al., 2009).

The highly siliceous rocks of Monterey Formation are important reservoir rocks to the petroleum industry in some parts of California, in particular. These rocks display noticeable differences in petroleum productivity with diagenetic alteration of porosity and pore structure in these rocks. Although the Monterey Formation rocks are porous, the low-permeability matrix is a bottleneck to production, driving commercial extraction in the coastal region to be primarily from fractured rocks. However, some matrix production from porcelanite rocks, especially in the San Joaquin basin, prompts industry interest in research in this subject. Previous published studies of porosity reduction in

siliceous sedimentary rocks were done by Isaacs (1981), Chaika and Dvorkin (2000), Chaika and Williams (2001) and Schwalbach et al. (2009).

Isaacs (1981) studied the porosity reduction in diatomaceous rocks of the Monterey Formation along the Santa Barbara coastal area using the method of computing the value of total dry porosity from bulk density and grain density values after removing the adsorbed water. The study focused mainly on porosities of diatomaceous, carbonate-free rocks and their diagenetic equivalent rocks. According to Isaacs, porosity in carbonate-free rocks decreases from 55-70% in diatomaceous rocks to 25-40% in opal-CT to 10-20% for quartz-phase rocks. This occurs by two abrupt porosity decreases due to the two step burial diagenetic transformation of silica at different depths (Figure 2.9.). She found that the reduction occurs mainly by compaction associated with silica dissolution and reprecipitation process during transition of diatomaceous rocks to opal-CT and quartz phase. The same pattern is followed for siliceous rocks with 5-30 % calcite composition and 5-10 % loss of porosity during each transition between silica phases.

A number of special properties or observed relationships indicate that porosity reduction in originally diatomaceous sediments occur in discrete diagenetic steps, quite different from gradual compaction of granular sediments: 1. Textural features, field with 60 % porosity is not consistent with gradual compaction related to a slow increase in burial load: 3. The abrupt change in physical properties indicated by sharp acoustic reflectors of offshore diatomaceous rocks formed during the formation of opal-CT (Hein and et al., 1978; and Isaacs, 1981) and the sharp reduction of porosity and gain of bulk density from 1.4 g/cm^3 in diatomaceous strata and 1.9 g/cm^3 in the underlying diagenetic

opal-CT related to such acoustic reflectors indicate an abrupt change (Figure 2. 10.) (Creager et al., 1973; Hein et al., 1978) indicate diagenetic transition mechanism for the formation:

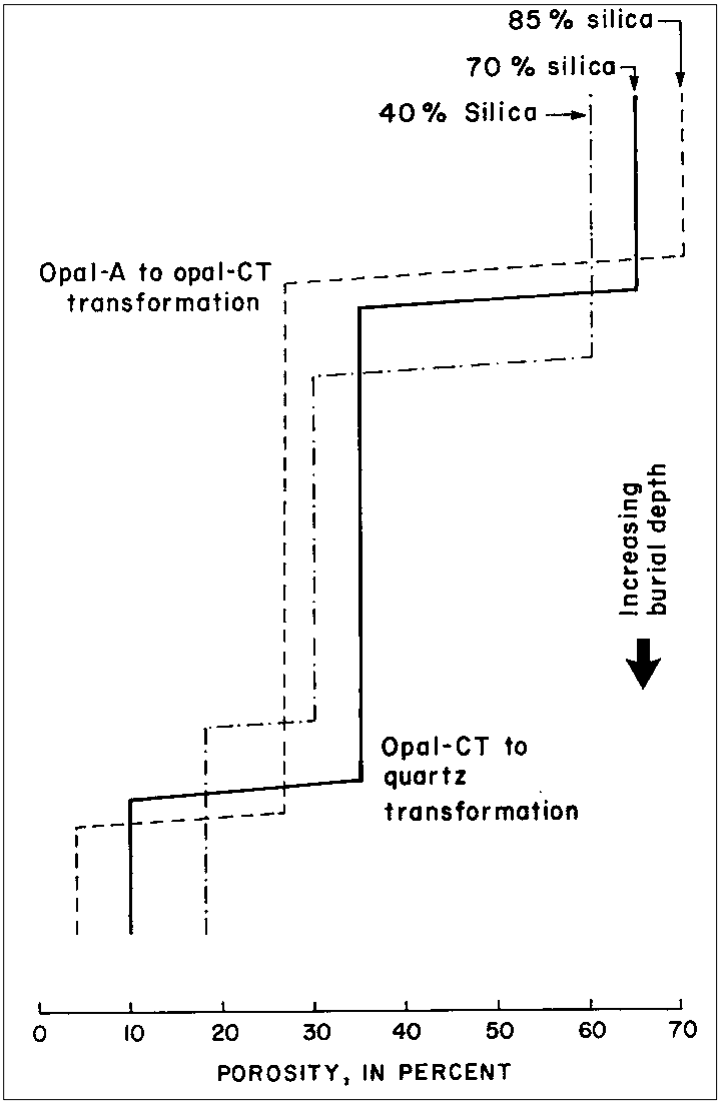

FIGURE 2.9. Schematic porosity-depth pattern for diatomaceous rocks and diagenetic equivalents at moderate burial depths (about 200-200m). In individual layers, an abrupt reduction in porosity is associated with each of the two silica phase transformations, but slightly different temperatures for the transformations in rocks of different composition can result in a comparatively broad zone of porosity reduction.

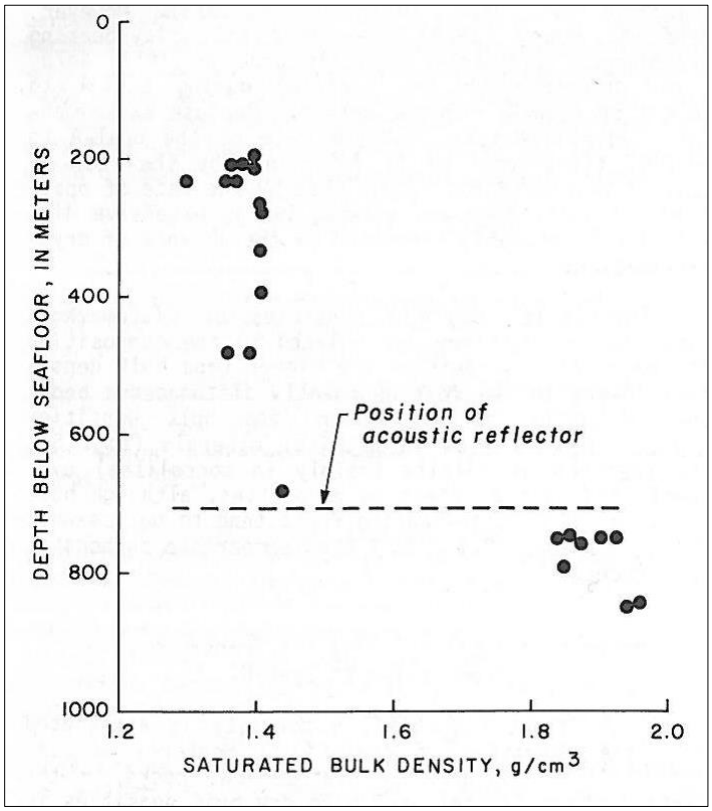

FIGURE 2.10. Abrupt gain in bulk density associated with boundary between diatomaceous (opal-A-bearing) rocks and opal-CT-bearing rocks in cores from the southern Bearing Sea. Data are from hole 192 on DSDP leg (Greager and others, 1973, p. 463-80; Lee,1973).

4. The diatomaceous rocks with abundant diatom frustules and skeletal remains and their nearly complete absence in laterally positioned, stratigraphically equivalent opal-CT-bearing rocks provides support for the involvement of a dissolution and reprecipitation mechanism: 5. Lamination in diatomaceous rocks at Elwood Beach and laterally occurring opal-CT rocks at Naples and Gaviota beaches yield identical thicknesses after correction by porosity reduction.

Similarly, at a larger scale, the different stratigraphic thicknesses of the same interval where measured at two different diagenetic stages represent the same porosity-

adjusted solid thickness, suggesting that porosity loss occurred with conversion of opal-A to opal-CT rather than pore-filling silica addition. Therefore, Isaacs (1981) concluded that the reduction of porosity is largely due to the in situ dissolution of opal-A silica and reprecipitation as opal-CT, resulting in destruction of the highly porous framework that then yields to burial load compaction. Although most of the investigations were on the opal-A to opal-CT transition, also Isaacs provides evidence and arguments that pore reduction from opal-CT is a similar in situ dissolution-reprecipitation process.

Nonetheless, within any single silica-phase state, original compositional difference is the main factor controlling porosity variations (Isaacs, 1981); with low-detritus siliceous rocks generally having higher porosities and lower bulk densities than detrital-rich siliceous rocks.

Chaika and Dvorkin (2001) studied dry bulk density, grain density, porosity mineralogy and silica phase of siliceous rocks in cores from five fields in the San Joaquin valley and outcrop samples from Point Pedernales and the Santa Barbara area. They identified two patterns of porosity reduction of diatomaceous rocks that relates to the detrital content of the siliceous rocks, and in part, to their locHaration in the inner (San Joaquin) versus outer (Point Pedernales and Santa Barbara) basins.

Group 1 (detrital-rich) displays: gradual and continuous porosity alteration during transition from opal-A to opal-CT; coexistence of both silica phases together in the same samples; similar porosities for two adjacent samples of different phases; specimens with greater abundances of clay minerals have lower porosity.

Group 2 exhibits: sharp decrease of porosities with silica phase; samples can be either nearly entirely opal-A or opal-CT with a distinct gap in the porosity distribution

with > 55% for opal-A and < 43% for opal-CT; increase abundance of opal-CT or quartz as well as decrease of clay minerals with reduction of porosity. Chaika and Dvorkin (2001) concluded that this pattern difference resulted from localized addition of pore-filling silica from solution. The difference between the two groups is shown in (Figure 2.11).

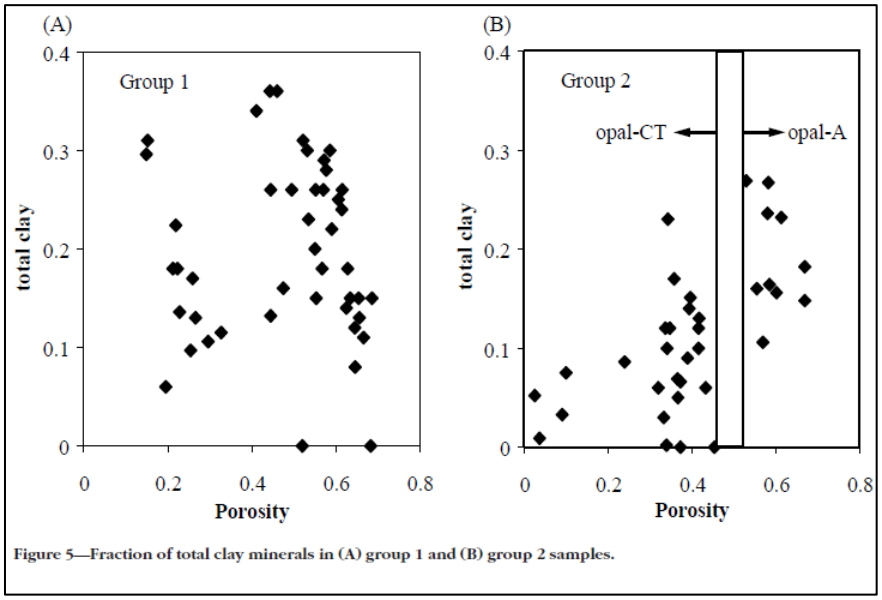

FIGURE 2.11. Fraction of total clay minerals in (A) group 1, and (B) group 2 samples.

Mercury injection capillary pressure tests indicate higher permeability in quartz porcelanites despite the decrease in matrix porosity during the phase change from opal-CT to quartz (Schwalbach et al., 2009). Capillary pressure for opal–CT lithologies is greater than 250 psia, whereas for opal-CT/siltstone rock types are around 80 psia. Schwalbach and others suggested that the permeability increase is due to an increase in pore-throat diameter in quartz-phase rocks.

CHAPTER 3

MATERIAL AND METHODS

The focus of this study was to characterize the pore-structure of porcelanites of varied composition and silica phase, and to develop optimum petrographic methods for high-resolution and high-quality imaging of porosity suitable for quantitative analysis. To accomplish these ends, chemical, mineralogical and physical properties of porcelanite were determined using various methods performed at California State University Long Beach (CSULB), University of Southern California (USC), University of California, Irvine (UCI). Sample preparation was done at CSULB [sawing and mechanical polishing], by Tulsa Sections, Inc., [epoxy impregnation and thin section impregnation], at USC and UCI [Focused Ion Beam micro-milling], and by the Boeing Company [argon ion milling/cross-section polishing]. The study included sample collection, sample preparation by varied means, X-ray diffraction (XRD), X-ray fluorescence spectroscopy (XRF) and energy dispersive X-ray spectroscopy (EDS), cross section polisher-argon ion milling (CP), scanning electron microscopy (SEM), multi-beam focused ion beam micro-milling scanning electron microscopy (FIB-SEM), and image analysis with Photoshop and ImageJ software programs.

The data generated by this study includes chemical composition, silica phase, high-magnification images of pores, and quantification of the size, shape and distribution of pore structures in porcelanites.

3.1. Sample Collection

Samples were collected from the Miocene Monterey Formation in Casmalia Hills on Vandenberg Air Force Base (Figure 3.1) in August 2012. This is one of a few locations known to contain both opal-CT and quartz-phase porcelanites (Pisciotto, 1981; Ijeoma, 2014). Fifteen porcelanite samples were collected from outcrops and road cuts according to their silica phases (opal-CT and quartz phase) over a range of compositions that would be classified as detrital-rich, detrital-poor, cherty as well as calcareous porcelanite. One very pure opal-CT porcelanite was specifically collected due to its extremely high apparent porosity.

3.2. Sample Preparation

One objective of this study was to determine the best analytical technique for high-resolution imaging and quantification of pore shapes. Consequently, several different approaches for sample preparation were attempted and evaluated for electron imaging. Additionally, different sample preparation methods were also required for compositional analyses. Fifteen porcelanite samples of different silica phases and compositions were powdered for XRD and these powders were also shaped into solid disks by hydraulic press for geochemical analysis by combined EDS/XRF. The same samples were also cut into ~ 26 mm x 46 mm x 3.2 mm blocks and mechanically polished progressively finer laps down to 3-µm grit size at CSULB. These specimens were shipped to Tulsa Sections, Inc for epoxy impregnation and thin section preparation. Tulsa Sections uses a vacuum/pressure chamber to apply a push/pull method of impregnation in which samples are placed under vacuum, immersed in liquid epoxy, then nitrogen is introduced until the chamber reaches 1200 PSI. The sample is left overnight

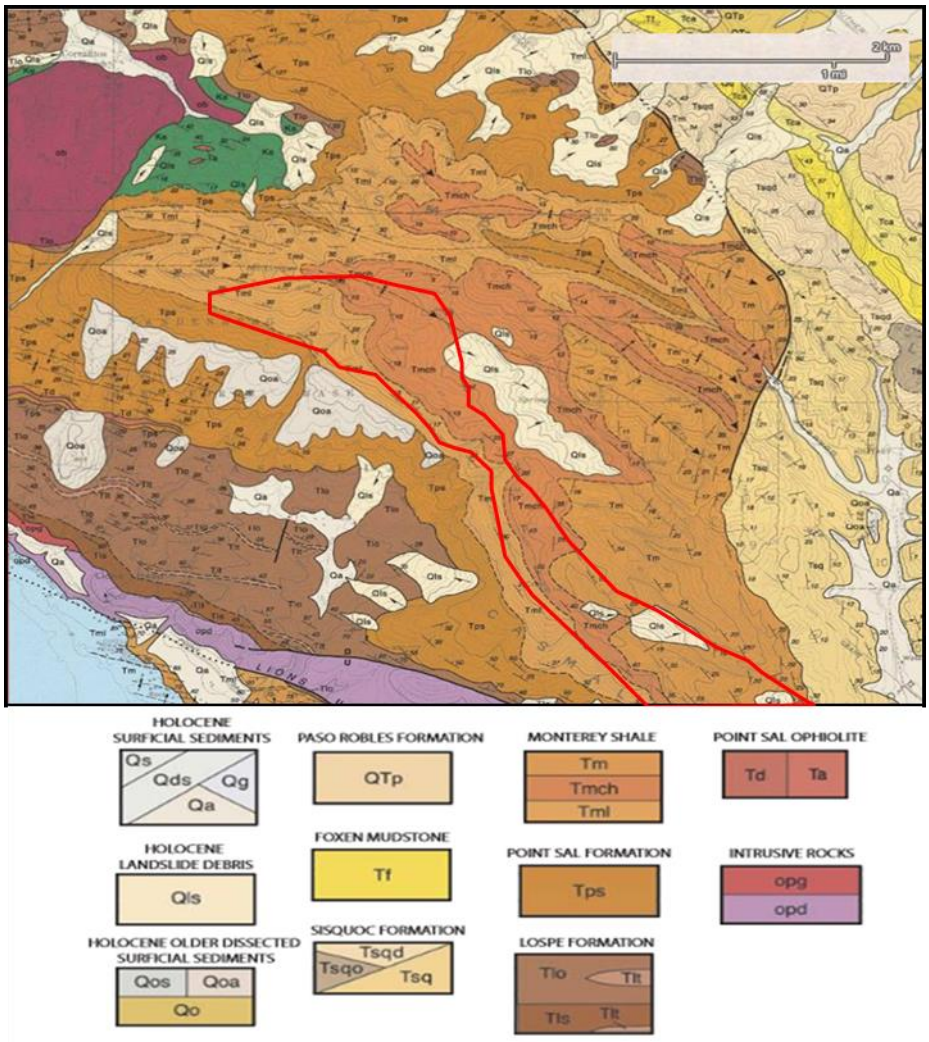

FIGURE 3.1. Geological map of Casmalia Hills, which is outlined by red. Sisquoc (Tsq), Upper Monterey (Tm), Middle Monterey cherts (Tmch), Lower Monterey (Tml) after Dibblee and Ehrenspeck (1989).

under 1200 PSI to impregnate and cure. After petrographic examination, the highly polished, uncovered epoxy impregnated thin sections were sputter-coated with conductive films of carbon or gold for SEM analysis.

A subset of the opal-CT phase samples were also cut into rectangular specimens of ~ 2-4 mm thickness with sharp perpendicular edges that were polished to 3 µm at CSULB. As much as possible, the polished edges were oriented perpendicular to laminations. These samples were sputter-coated with silver (for mounting and conductivity), then micro-milled with focused ion beam (FIB) at USC to provide a milled surface of ~25 by 15 µm. Finally, the specimens were sputter-coated with 5 nm thickness of gold for SEM imaging.

Ten of the original fifteen samples were also prepared somewhat differently. They were first cut and polished to 3 µm finish at CSULB. They were further polished with polishing films down to 0.1 µm to achieve fine finishes in the Laboratory for Electron and X-Ray Instrumentation (LEXI) at UCI. A finer mechanical polish helps to minimize curtain effect during micro-milling with the focused ion beam. Deposition of platinum across the penetrated face further planarized the surface and decreased irregularities in the milled surface. A 3 nm-thick conductive sputter coating of iridium was applied for FIB, followed by a 1.5 nm-thick coating for SEM to eliminate any charging effect during imaging. `

In our final, and most successful, preparation technique, a much larger, mm-scale area of six of these samples were highly polished by argon beam milling at Boeing Company in El Segundo. They were then coated with 1.5 nm iridium for SEM imaging in LEXI, UCI.

3.3 X-Ray Diffraction

The silica phase and mineral composition of all the samples were analyzed with a Rigaku MiniFlex X-ray diffractometer (XRD) operated at 30 kV and 15 mA with X-rays generated from a copper anode target. Samples were scanned from 5 to 40 degrees 2θ using step width 0.2° 2-theta for 1.0 sec. Opal-CT and quartz phases were distinguished

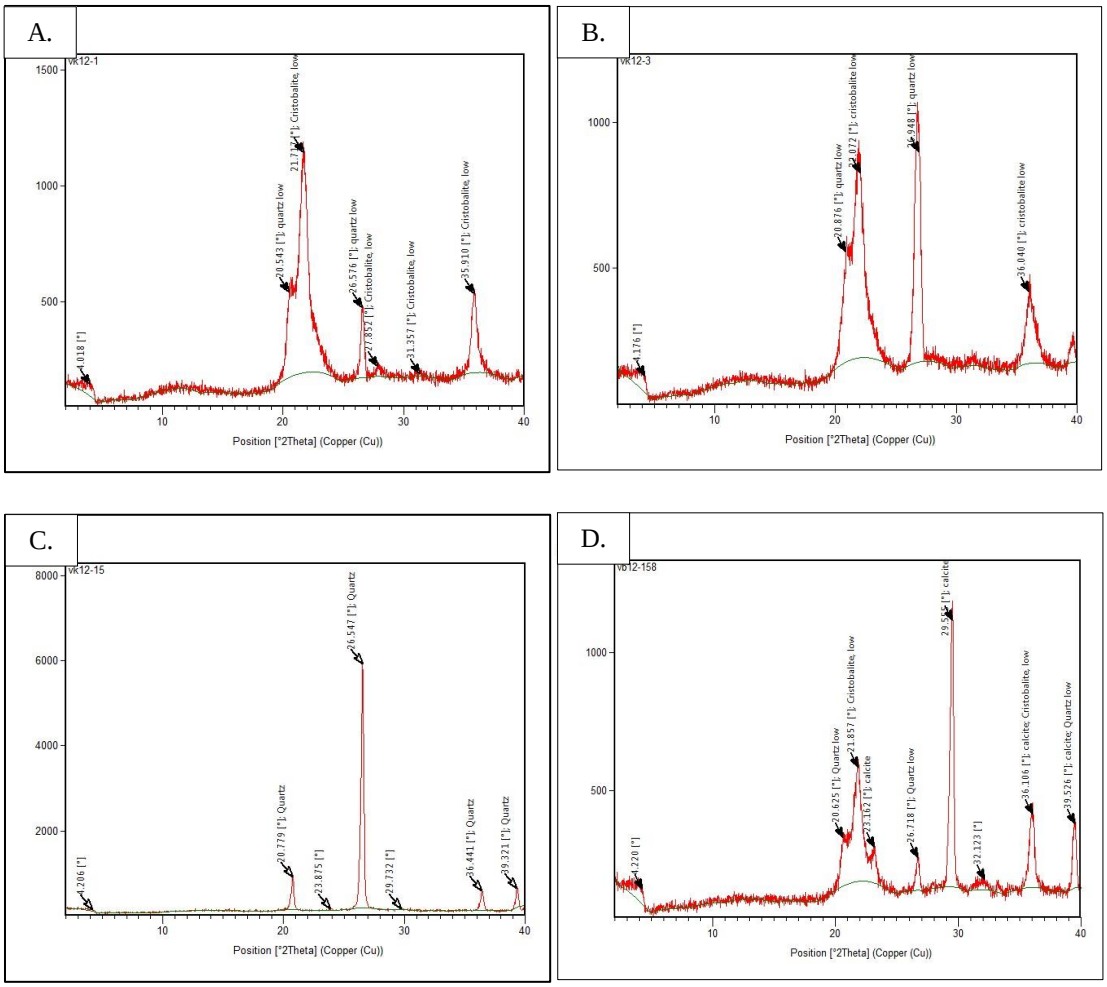

FIGURE 3.2. XRD results showing silica phase and mineralogic composition of porcelanite: A. opal-CT porcelanite; B. mixed opal-CT and quartz phase porcelanite; C. quartz phase porcelanite; and D. calcareous opal-CT porcelanite.

mineralogic composition was based on peak position and intensity (Figure 3.2D) using PANalytical X'Pert High Plus software and the International Center for Diffraction Data Powder Diffraction File Minerals database.

3.4 Energy-Dispersive X-Ray Spectroscopy and X-Ray Fluorescence Spectroscopy

Combined EDS and XRF were used for bulk chemical analysis of the samples. These analyses were run on a iXRF Systems Iridium Ultra microanalytical system mounted on a FEI Quanta 200 ESEM (Environmental Scanning Electron Microscope), operated as described in Ijeoma (2014). Isaac's (1980) empirical formulas were used to convert major element oxide percentages to the abundance of detritus and silica (biogenic and diagenetic) components. The detritus and silica abundances were computed as follows:

$$\text{Detritus} = 5.6 \times Al_2O_3$$

$$\text{Silica (biogenic and diagenetic)} = SiO_2 - (3.6 \times Al_2O_3)$$

These values were then normalized to 100% on a carbonate-, phosphate- and organic matter-free basis.

3.5 Ion Beam Milling (FIB-SEM) and Cross Section Polisher-Argon Ion Milling (CP)

Opal-CT porcelanite samples have ultramicroscopic size pores and pore-throat diameters that inhibited complete impregnation of thin sections with epoxy. Due to this undesired result, the prepared thin sections were unfit for the purpose of imaging porosity using backscattered electrons to map areas of pores versus solid matrix. Therefore, a JEOL JIB-4500 Multi-Beam Focused Ion Beam - Scanning Electron Microscope (FIB-SEM) was used for micro-milling and monitoring the milling process. Multi-step milling used a progression from coarser to smaller beam size as well as faster to slower milling

rate to produce finer polishing. This produced a much improved surface, but one that still had problems. Although samples were mechanically polished to 3 µm grit size to rectangles with sharp edges, the surfaces of the specimens were still too irregular (see Figure 3.3) due to the high porosity nature of porcelanite to allow even beam- penetration during ion milling. Consequently, a curtain effect was pervasive (see Figure 3.4). "Curtain effect" is the formation of striations on an ion-milled surface, due to heterogeneous structures, density or chemical composition of specimens (Tseng, 2008)). This unwanted effect is one of the chief problems of FIB milling.

Another FIB instrument – a FEI Quanta 3D FEG Dual Beam FIB/SEM – was used for milling as well as monitoring the process and selection of suitable sites on the porcelanite samples at LEXI, UCI. The stage was tilted at 10^0 to the horizontal and a multi-step milling process was conducted on the specimens. A voltage of 30 kV and probe current of 50-30 nA were used in the process with a depth of 8 µm. This cut was rough and finer cuts were made deeper into the sample using a "stair-step" geometry. Finally, a voltage 30 kV and probe current of 30 nA with a depth of 10 µm was applied for achieving a fine finish.

After the milling process, a 1 µm thick layer platinum was applied with beam induced-deposition, then cleaned to mitigate the curtain effect. For the cleaning process, the stage was tilted at 10^0 to the horizontal surface, and platinum was cleaned by a multi-pass approach at 30 kV with current progressively decreasing from 30 nA to 0.3 nA. The completely prepared milled surface has a cross section of ~25 x 25 microns. This process After the milling process, a 1 µm thick layer platinum was applied with beam

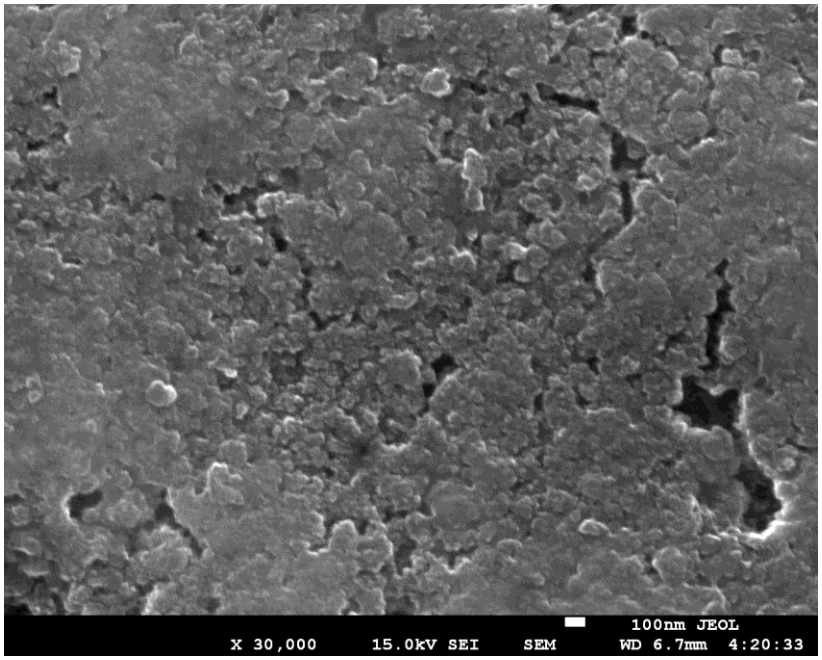

FIGURE 3.3. Secondary electron images of opal-CT porcelanite magnified at the same scale showing uneven surface topography: a mechanically polished rough surface.

induced -deposition, then cleaned to mitigate the curtain effect. For the cleaning process, the stage was tilted at 10^0 to the horizontal surface, and platinum was cleaned by a multi-pass approach at 30 kV with current progressively decreasing from 30 nA to 0.3 nA. The completely prepared milled surface has a cross section of ~25 x 25 microns. This process resulted in much less curtain effect than achieved with the JIB-4500 Multi-Beam FIB-SEM (Figure 3.4 B). Minor striations only became somewhat pronounced lower in the cut surface (Figure 3.4A and B). The SEM in the same instrument was used to follow the FIB milling progress and select suitable milling sites. Although this SEM is useful for monitoring during milling (Figure 3.4C), it was not used for imaging since higher resolution and high-quality imaging are required for this study (Figure 3.4D).

FIGURE 3.4. Secondary electron images A. Cross section of the FIB-milled surface; B. Slightly magnified image showing the curtain effect at depth (lower part of image); C. and D. Images provided by FIB-SEM (low resolution) and FEI Magellan 400 XHR SEM (high resolution) instruments respectively.

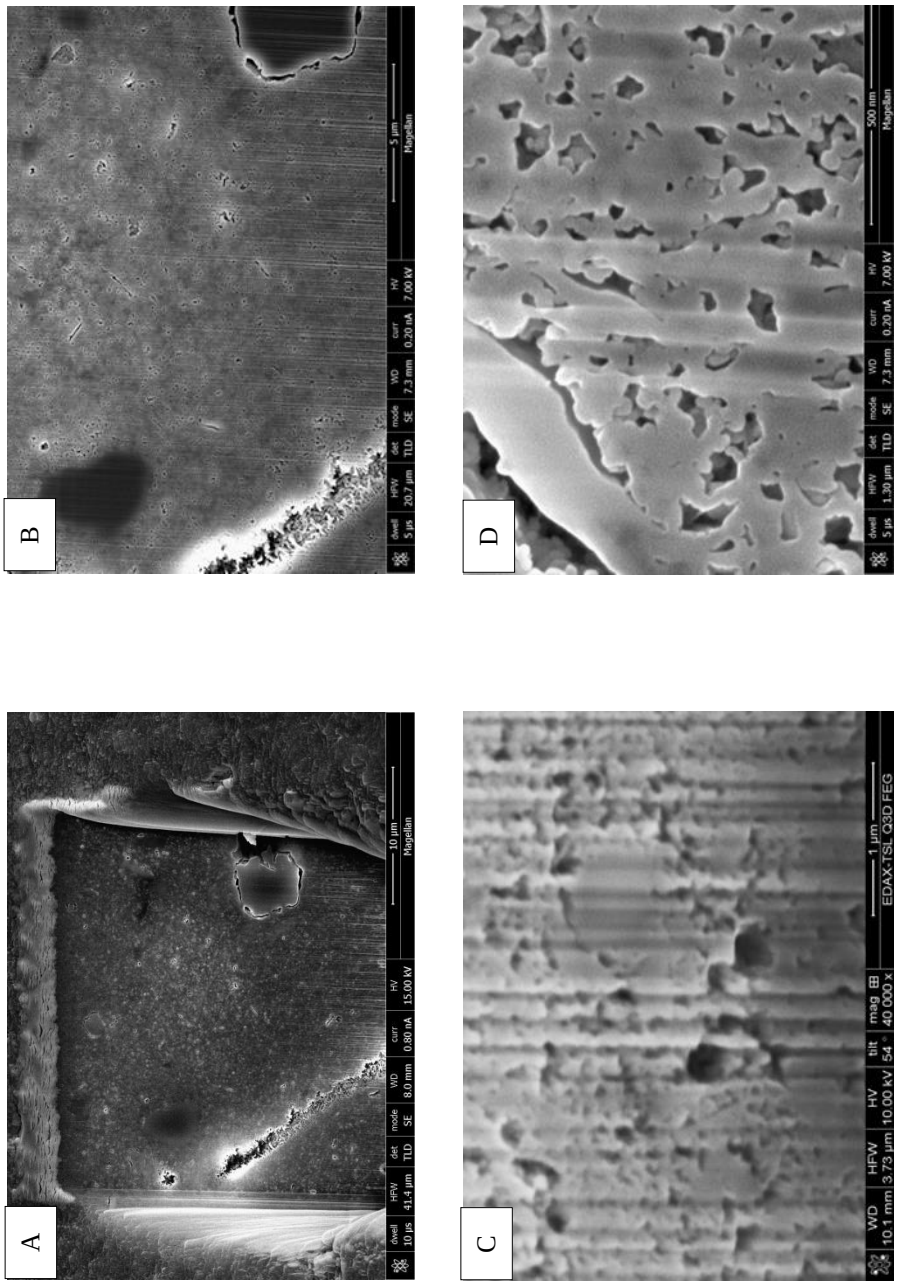
A
B
C
D
Magellan
EDAX-TSL Q3D FEG

A stand-alone argon ion mill – a JEOL Cross-Section Polisher (CP) – was used at Boeing Company to overcome limitations of the previously employed techniques of sample surface preparation. This method allows for a larger area to be polished as well as elimination of artifacts and distortion. Typically, a polished surface cross section of 1.5 mm x 0.5 mm width and several microns depth was obtained (Figure 3.5A). This yields a polished surface area ~500 times larger than that produced by FIB-SEM, permitting better characterization of spatial variation on a sedimentary lamination scale. Furthermore, the swinging of the stage to $\pm 30^0$ during milling produces uniform etching of specimens reducing development of beam striations. As a result, highly polished surfaces were obtained in this process that almost totally eliminated curtain effect (Figure 3.5B). This method is effective in producing planar surfaces on porcelanites that are suitable for the very high resolution images required for this study.

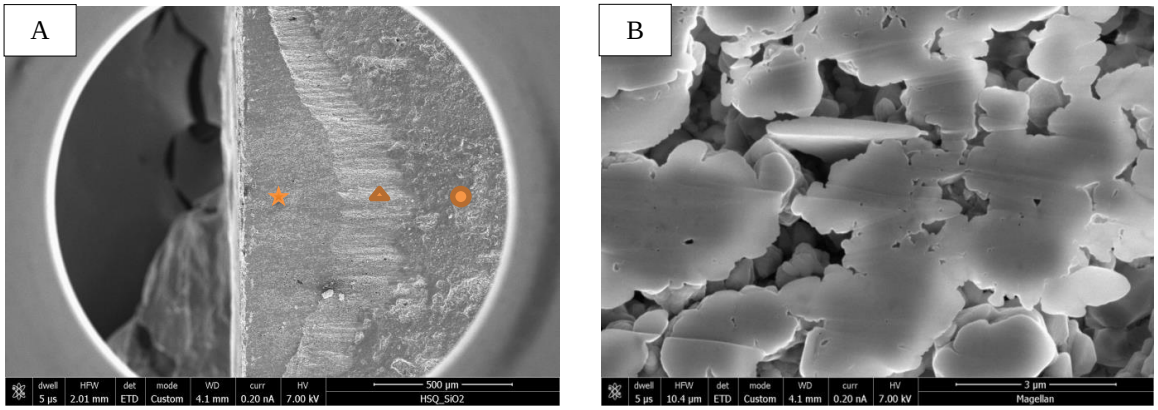

FIGURE 3.5. Argon-ion beam milled porcelanite. A. a large cross section of the milled area 1.mechanically polished surface (★), 2. transition zone (●), and 3. Argon ion-milled surface (▲). B. Highly polished quartz-phase porcelanite with minimum curtain effect.

3.6 Scanning Electron Microscopy (SEM)

Scanning electron microscopes were used for imaging, using secondary electrons or backscattered electrons. Three different types of SEM were used for imaging pores depending on resolution, charging problem, and clarity of images provided. A FEI Quanta 200 ESEM (Environmental Scanning Electron Microscope) at CSULB was used for imaging the epoxy-impregnated thin sections. A JSM 7001 SEM at USC was used for imaging the epoxy-impregnated thin sections, and FIB-milled specimens at CEMMA, USC. The highest resolution images were taken with a FEI Magellan 400 XHR SEM at LEXI, UCI. The specimens used for high-resolution imaging were mainly the FIB-milled and Argon-Ion milled samples prepared at LEXI and Boeing Company, respectively.

3.6.1 Imaging Methods

3.6.1.1 Backscatter electron imaging (BSEI). The Quanta 200 ESEM at CSULB was used for backscattered electron imaging of epoxy impregnated thin sections. Electrons are differentially backscattered based on compositional and density contrasts between the solid rock matrix and the pore-filling epoxy. An acceleration voltage of 25kV and a spot size of 4-5 under high and low vacuum conditions were used to image both opal-CT and quartz phase porcelanites. It was possible to image the quartz-phase porcelanite at a high accelerating voltage (Figures 3.6A and B); however, there were some charging and resolution problems. Because electrons are backscattered chiefly from a teardrop-shaped volume below the surface of the specimen that often contains different materials, BSEI does not generate images showing sharp edges at the pore/grain contact. Instead these contacts are usually diffuse unless the contact is oriented straight down into the slide. In contrast to the results with the quartz-phase samples, the thin

sections of opal-CT-phase porcelanite have much lower permeability and were only partially impregnated by epoxy. This is due to the size and shape of their ultramicroscopic pores as seen on the carbon-coated image acquired by the JEOL JSM 7001 SEM (Figure 3.6C). Although the BSEI image quality was good enough to quantify for quartz-phase samples, it still was not optimal due to the fuzziness. And, furthermore, BSEI was not useful on either instrument for opal-CT phase rocks.

Some images of quartz phase porcelanite were also acquired with JEOL JSM 7001 SEM. The clarity of the images were less than optimal and charging problems were also conspicuous (Figures 3.6 D and E) when trying to use this instrument to achieve high resolution images. Particularly with high voltages (20-25 V), the charging problem interfered with acquisition of high-quality images. Generally, the contrast and clarity of the images are better under high vacuum than low vacuum conditions, but high-vacuum images also tended to have more charging effects (Figures 3.6 D&E).

3.6.1.2 Secondary electron imaging. For the most part, secondary electron images show topography, and were used to directly image the distribution of pores and solid rock matrix. The FEI Quanta 200 at CSULB was not capable of acquiring SEI images of sufficient magnification and quality for this study. The JEOL JSM 7001 SEM was used for examining the samples prepared by FIB-SEM milling at USC. Although, high resolution images were acquired at 15 kV, the curtain effect form the FIB preparation was inescapable (Figure 3.3D). This phenomenon makes pore analysis challenging due to the difficulty of consistent image processing and spatial quantification of an irregular and unevenly illuminated surface.

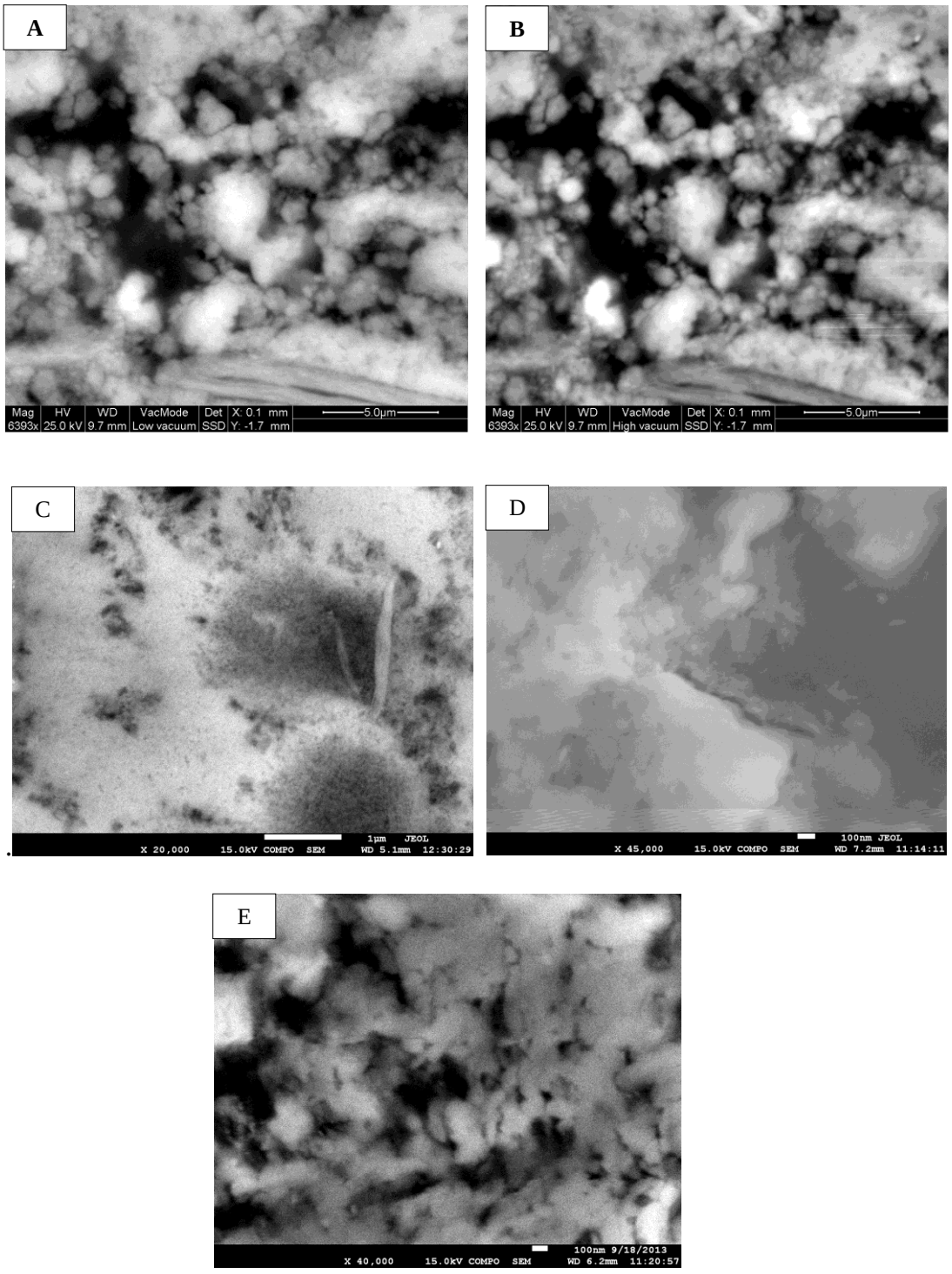

FIGURE 3.6. SEM images: A & B. Low and high vacuum images of quartz phase porcelanite; C. Images of carbon coated opal-CT phase porcelanite and D & E Image of quartz phase porcelanite at low and high vacuum respectively.

All of the previous methods have problems and limitations with defects or/and resolutions. Consequently, most acquisition of the SEI images was carried out with FEI Magellan 400 XHR SEM, at UCI. An accelerating voltage of 7 kV, current of 0.20 nA and WD of 5-7.5 mm were typically used to collect data. Low kV and short working distance helped to minimize charging and maximize resolution of surface details. Images of cut surfaces of specimens milled by FIB and Argon-ion beam were acquired with an extreme high resolution (Figure 3.7).

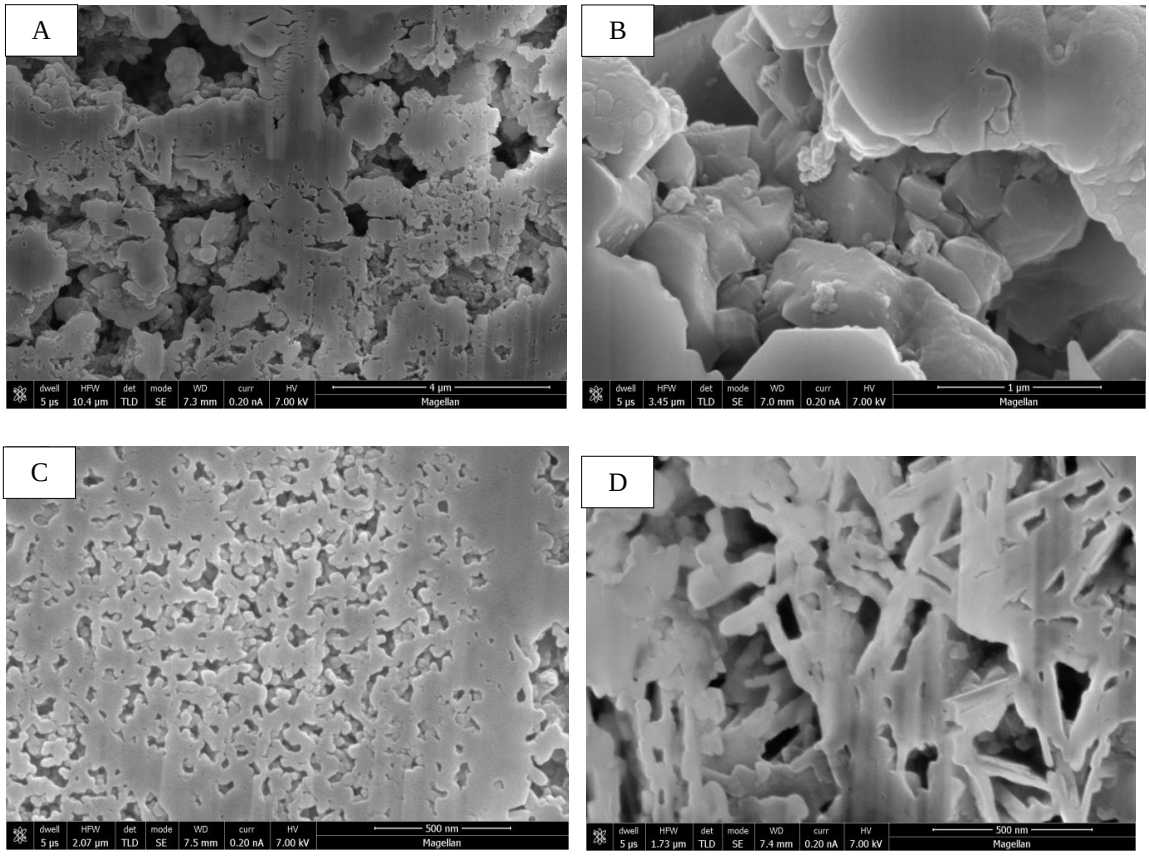

FIGURE 3.7. High-resolution argon-ion beam (A, B &C) and FIB (D) milled surfaces images.

3.7 Photoshop and ImageJ

The cross section polisher-argon ion milling (CP) and focused ion beam (FIB) polishers provide polished surface of porcelanite with minimum artifacts. However, the acquired scanning electron microscope images in this study are still not of optimal quality and have problems during segmentation (definition of pore boundaries). The following is a list of image characteristics that necessitate special, interactive image processing:

Some have noise (Figure 3.8A).

Striations (curtain effect) formed during FIB polishing cause uneven brightness and focus (Figure 3.8B).

Suboptimal brightness and contrast (Figure 3.8C)

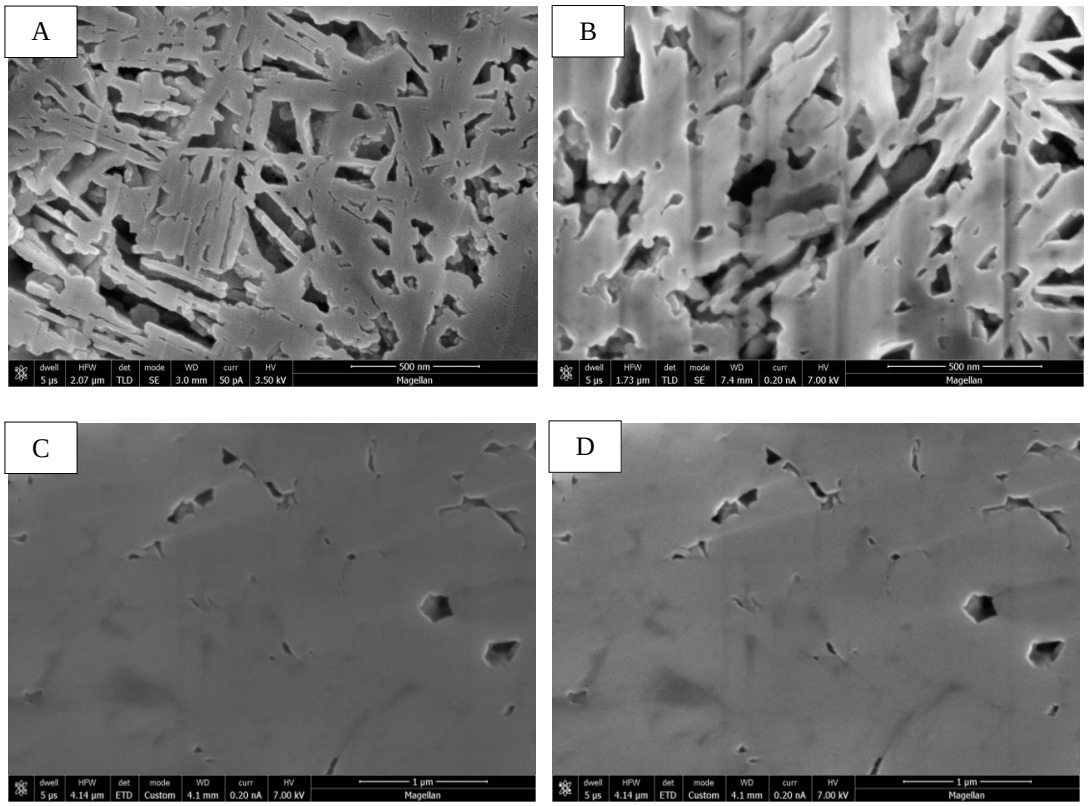

FIGURE 3.8. A, C, & D. Noisy, flat and enhanced images, respectively; B. Image with curtain effect.

Excess electron emission at sharp edges result in brightness discontinuities causing problems during segmentation. Symbol ▲ in (Figure 3. 9).

Low-gradient surfaces at the outer edges of pores results in a tonal gradation that does not provide a sharp boundary for quantification. Symbol ★ in (Figure 3.9)

Some pores have complex morphologies with different depths and surfaces (e.g. crystal faces), displaying different tones for the same pore. This makes segmentation difficult. Symbol ● in (Figure 3.9)

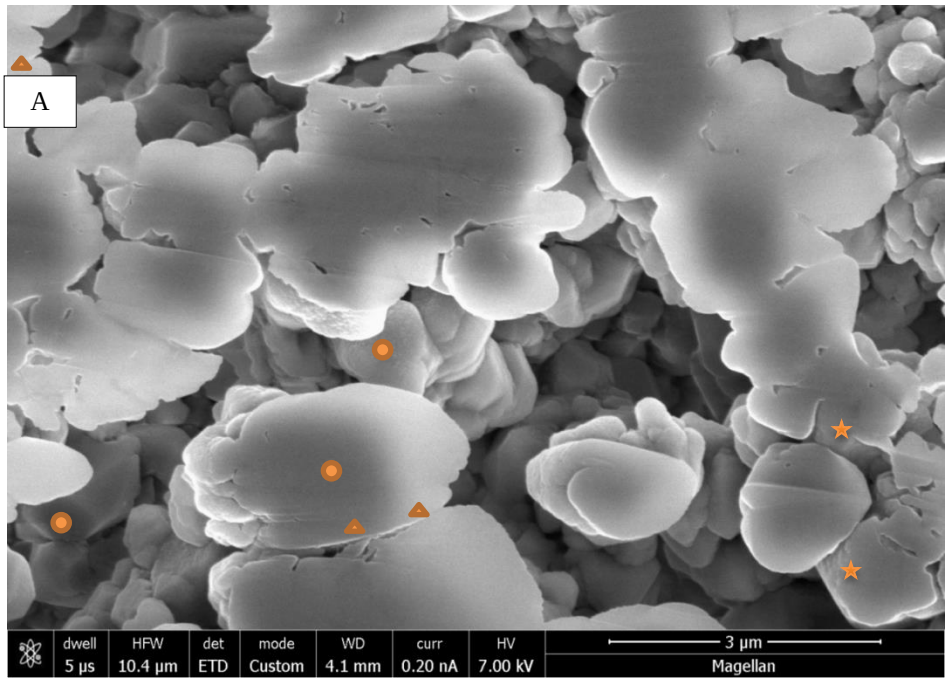

FIGURE 3.9. Images with discontinuities and layers of pores having the same tone as the milled surface of the matrix.

Because of these issues, images had to be optimized prior to digital quantification by an interactive and iterative procedure. Adobe Photoshop CC (2014) and ImageJ

programs were used to process and analyze the data in this study. The following processing techniques were used to overcome the problems described above.

Levels in Photoshop and Contrast stretching in ImageJ:

Used to adjust the brightness, contrast and tonal range level (Figure 3.10).

Accomplished by stretching out a portion of the acquired intensity values to span a desired range.

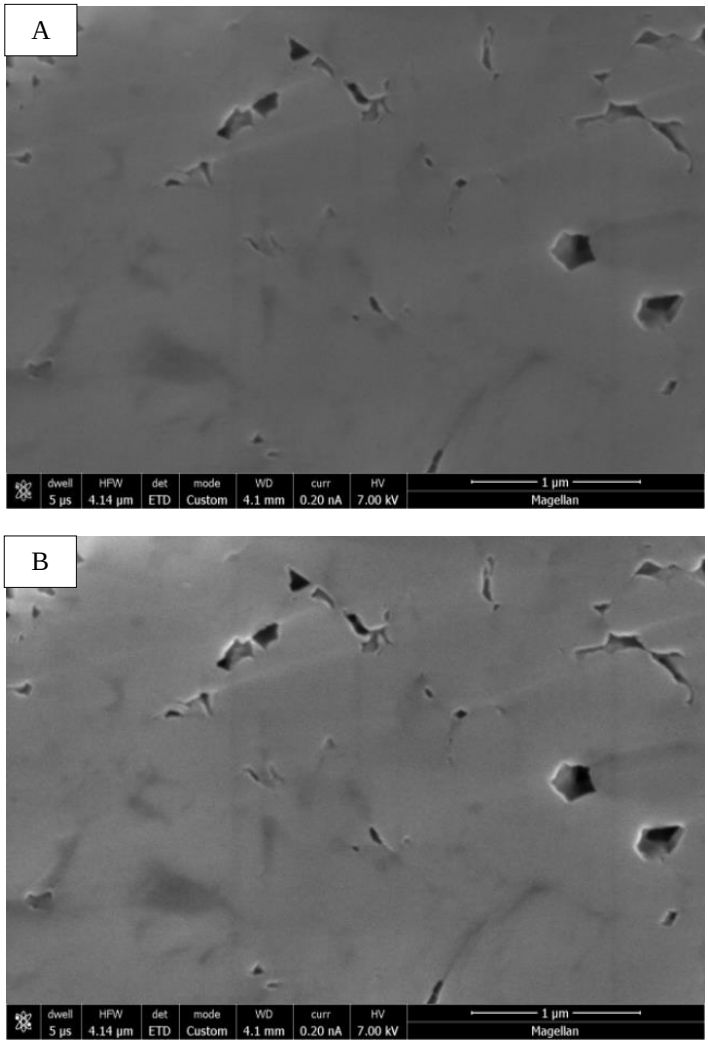

FIGURE 3.10. Image of low brightness & contrast and B. Enhanced image clipped to 35 (lower) and 205 (higher) intensity values and then stretched to 0-255 intensity levels.

Curves in Photoshop: The same purpose as levels but manipulated by shaping a sigmoidal correlation curve between the input and output so that more or less contrast is acquired over different ranges.

Despeckle and median filter: Used to reduce Noise and outlier values.

Image segmentation

Image segmentation is a process of dividing an image into meaningful structures-pores in this study. The following techniques were used in image segmentation:

Posterizing and LUT:

Posterizing is a conversion of continuous gradation of tone to several regions of fewer tones which shows details with the purpose to pinpoint edges.

Look Up Table (LUT) are false color or pseudo-color displays with assigning color values to each brightness value applied to identify edges of pores or pores.

Grow and similar: used to delineate edges as the pores have different tone.

Grow is used to broaden the area to reach the edges of pores.

Similar is used to select all regions with the same intensity value in the whole image.

Thresholding: is an image segmentation method partitioning greyscale images into feature of interest (pores in this study) and background.

Quantitative image analysis was carried out using ImageJ software. Area, %area, perimeter well as shape descriptor, such as circularity, roundness, aspect ratio and roundness were computed using mathematical routines and algorithms described at http://imagej.nih.gov/ij/.

CHAPTER 4

RESULTS

Porcelanite samples composed of both opal-CT and quartz phase silica were analyzed for composition, pore morphology and fabric. Results of this study show that pore shape and size vary with silica phase as well as composition and also spatially, consequently several porosity microstructures are categorized (Figure 4.1, 4.2 & 4.3, and Table 4.1). The opal-CT and quartz phase porcelanites have three distinct microfabrics each that vary with composition or diagenetic environment. For opal-CT porcelanite, two types of detrital-poor and one detrital-rich porcelanite were studied. Similarly, for quartz-phase porcelanites, two types of detrital-poor porcelanite (laminated and massive) and one detrital-rich porcelanite were analyzed.

Numerous systems of pore classification have been proposed in the geologic literature. Chalmers et al. (2009), Rouquerol et al. (1994), and Choquette and Pray (1970) recommended different classification schemes for mudstones and for carbonates. Many of these classification systems do not adequately distinguish pores in the size range encountered in this study. For example, Rouquerol et al.'s (1994) pore size terminology doesn't adequately separate the microporosity of mudrocks into different categories across a range from several nanometer to micrometer size. Similarly, Choquette and Pray (1970) categorize all pores less than 62.5 μm in a single group which is insufficient for the range of very small pores found in mudrocks. In this study, pores sizes range from nanometers to micrometers and the above-mentioned classification systems are not

sufficient to describe the pore size distribution. Therefore, we adopt the classification system of Loucks et al. (2012) as appropriate to represent the pore size range found in this study and consequently recognized two ranges of pore size: nanopores from ≥1 nm to < 1 µm and micropores from ≥ 1 µm to < 62.5 µm. Aspect ratio, roundness, circularity, solidity and perimeter-over-area shape descriptors are calculated from the raw shape measurements. The following tables and figures are characterizations of the separate classes of microstructure that relate to different lithology and composition.

TABLE 4.1. Silica Phase and Composition of Samples Analyzed

Phase	Opal-CT			Quartz		
Sample #	VK12-6	VK12-11	VK12-178	VK12-15	VK12-16	VB12-43
Detrital content	Detrital-poor	Detrital-rich	Detrital-poor	Detrital-poor	Detrital-poor	Detrital-rich

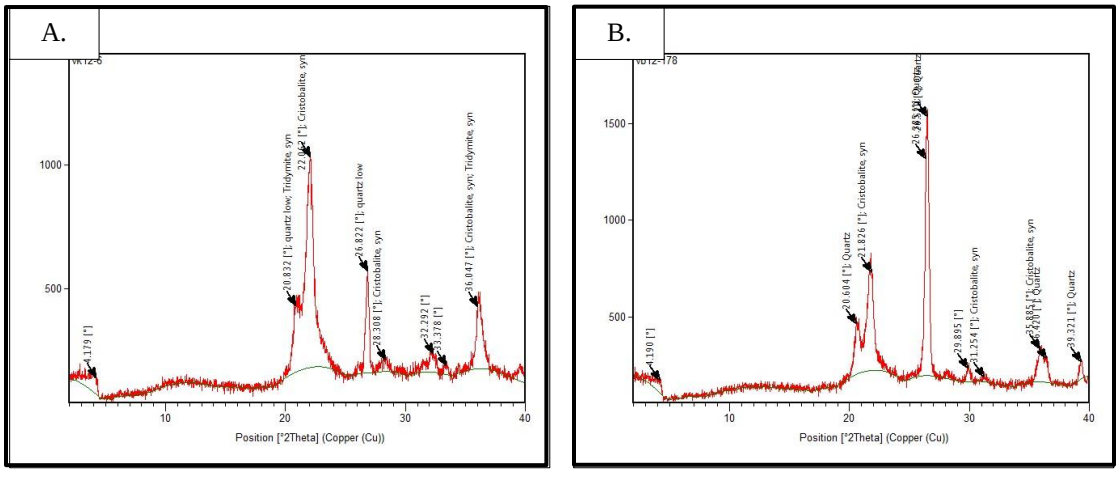

FIGURE 4.1. X-ray diffractograms displaying the minerals and silica phases of the samples analyzed in this study. The step shown at approximately 4.1° 2-theta is an artifact of the system.

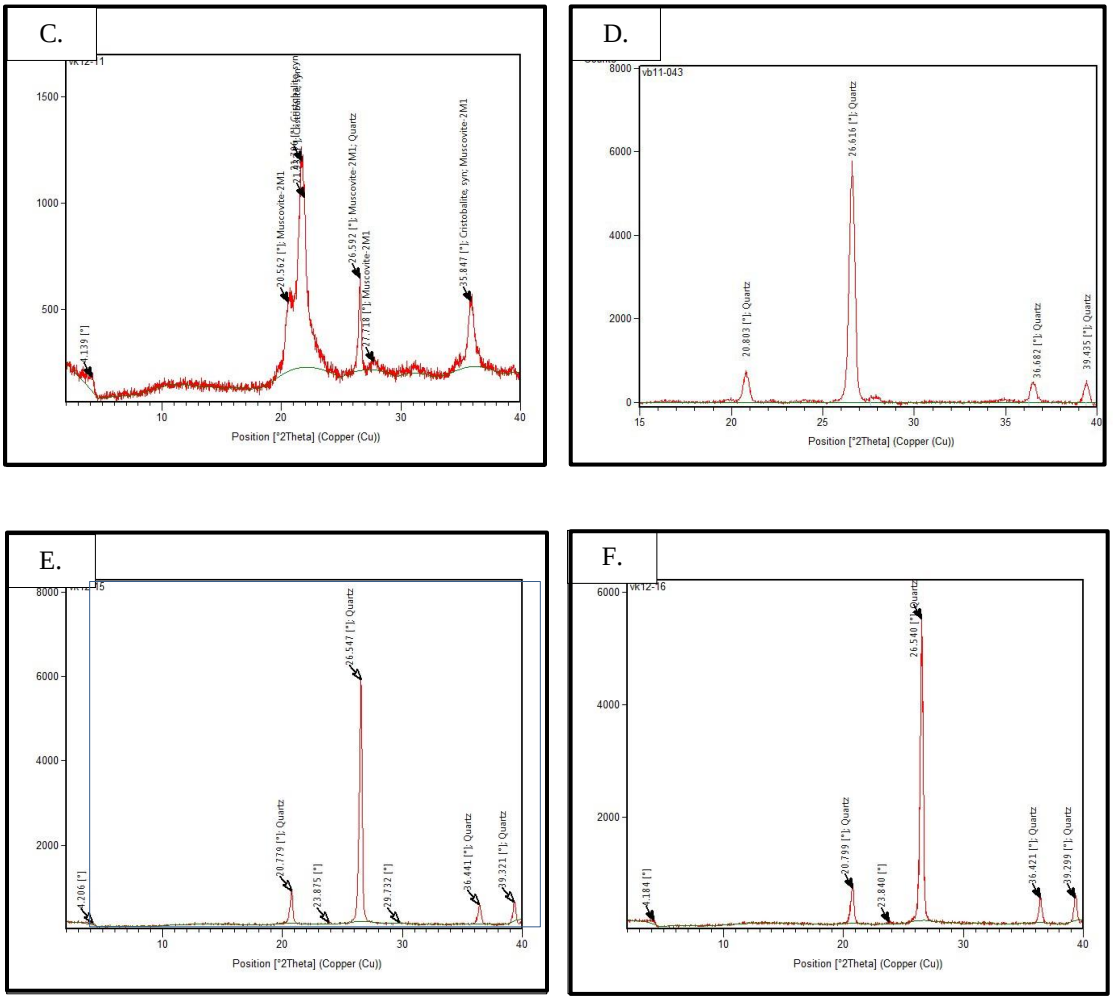

FIGURE 4.2. Continuation of FIGURE 4.1

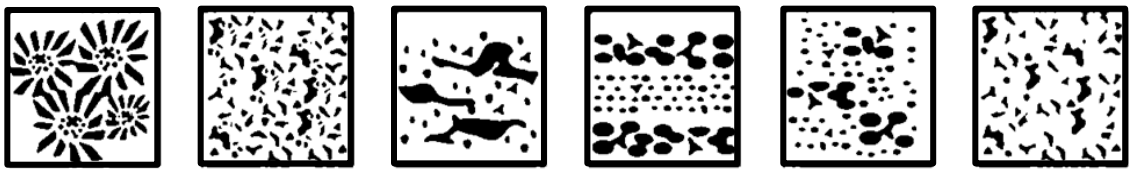

Opal-CT Detrital-poor | Opal-CT Detrital-rich | Opal-CT Detrital-poor Transition-zone | Quartz Detrital-poor | Quartz Detrital-poor | Quartz Detrital-rich

FIGURE 4.3. Pore microstructure according silica phase and silica:detritus range.

4.1. Opal-CT Phase Porcelanites

4.1.1 Detrital-Poor Porcelanite: Lepispheric Porosity

The detrital-poor porcelanite has a lepispheric microstructure (Figure 4.4) that consists of three distinct layers – interlepisphere, mantle and the core of most lepispheres. The core is composed of granular, anhedral crystallites of opal-CT; it is highly porous with well-connected nanopores (Figure 4.5). The mantle is composed of a massive groundmass of opal-CT that is virtually impermeable, isolating the core and rendering its porosity largely ineffective. The interlepisphere pores are locally larger nanopores that are not as well connected as in the core. They form between larger, bladed crystals that generally radiate outward from the mantle region (Figure 4.6). Most larger interlepisphere pores are elongated and angular, reflecting the bladed crystals, but in some locations, well-shaped pores do not develop and instead form a more irregular habit (Figure 4.7).

Sample VK 12-6 was polished using an argon-ion mill Cross-Section Polisher (CP) and imaged using secondary electron microscopy (FIGURE 4.4). It is opal-CT phase and detrital-poor. Figures 4.8, 9,10 & 11, and Table 4.2 & 4.3 show the results of digital image analysis.

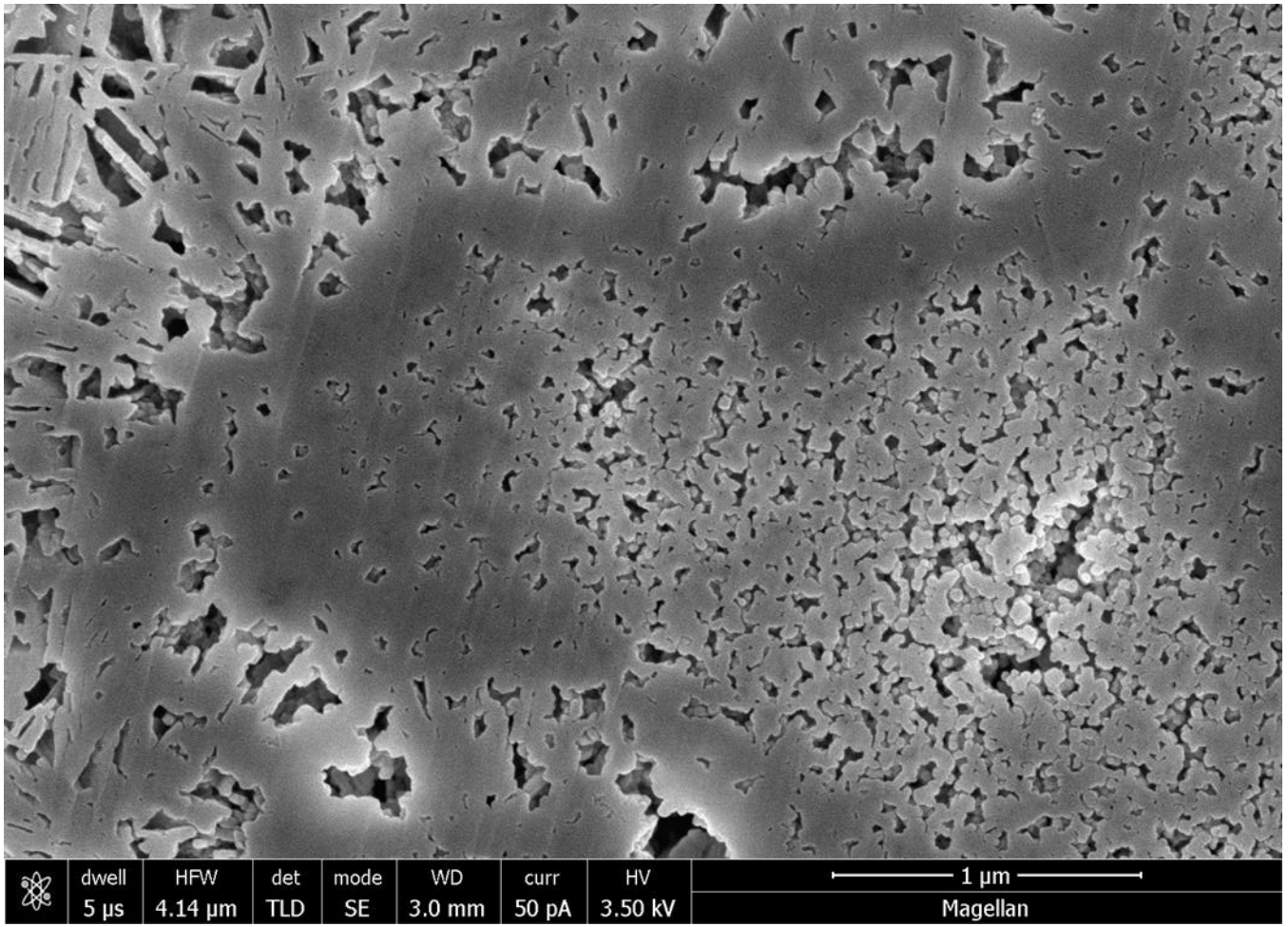

FIGURE 4.4. Lepispheric fabric with three distinct zones of porosity (VK12-6).

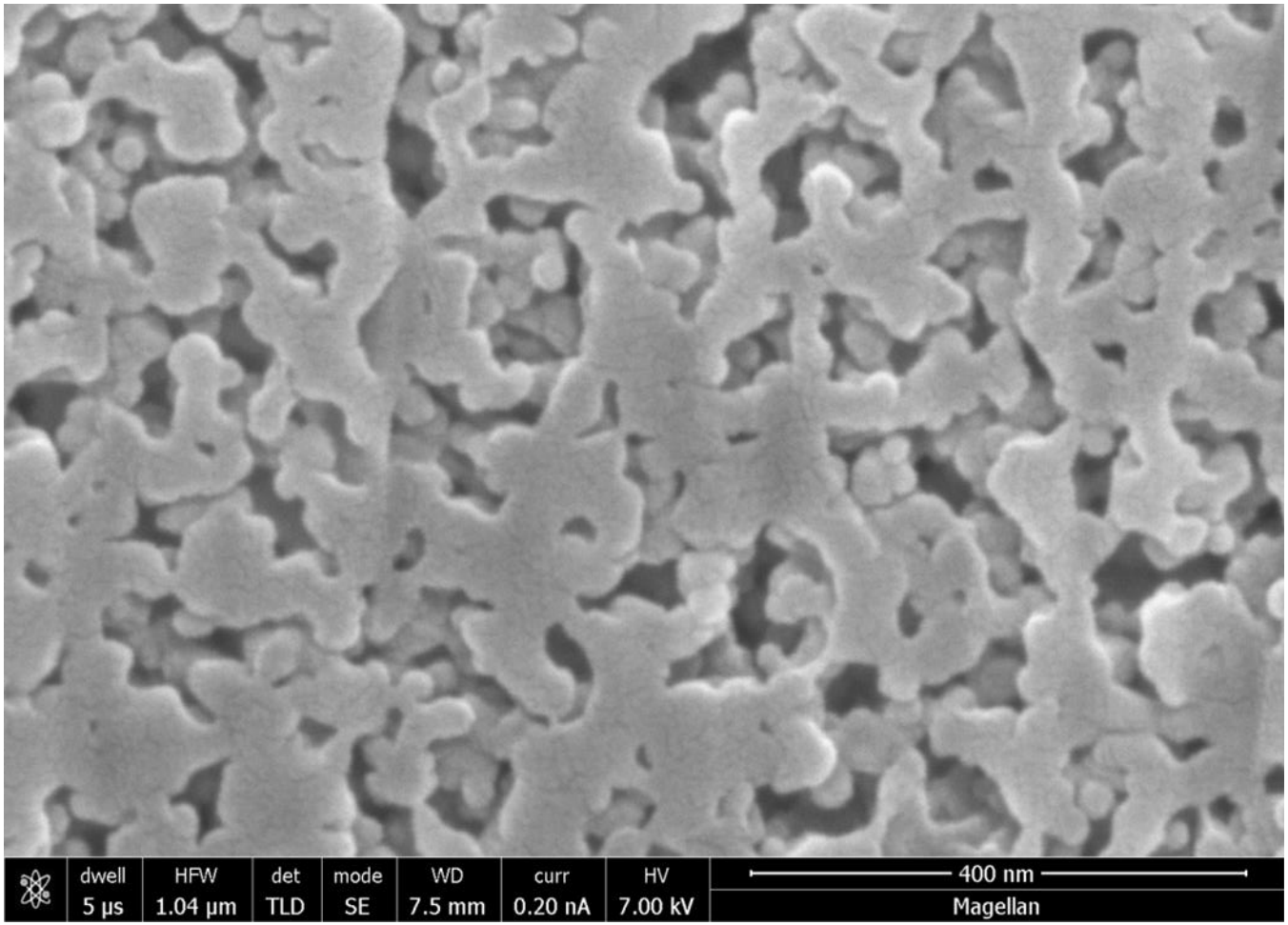

FIGURE 4.5. The core composed of anhedral, granular crystallites and irregular, interconnected pores (VK12-3).

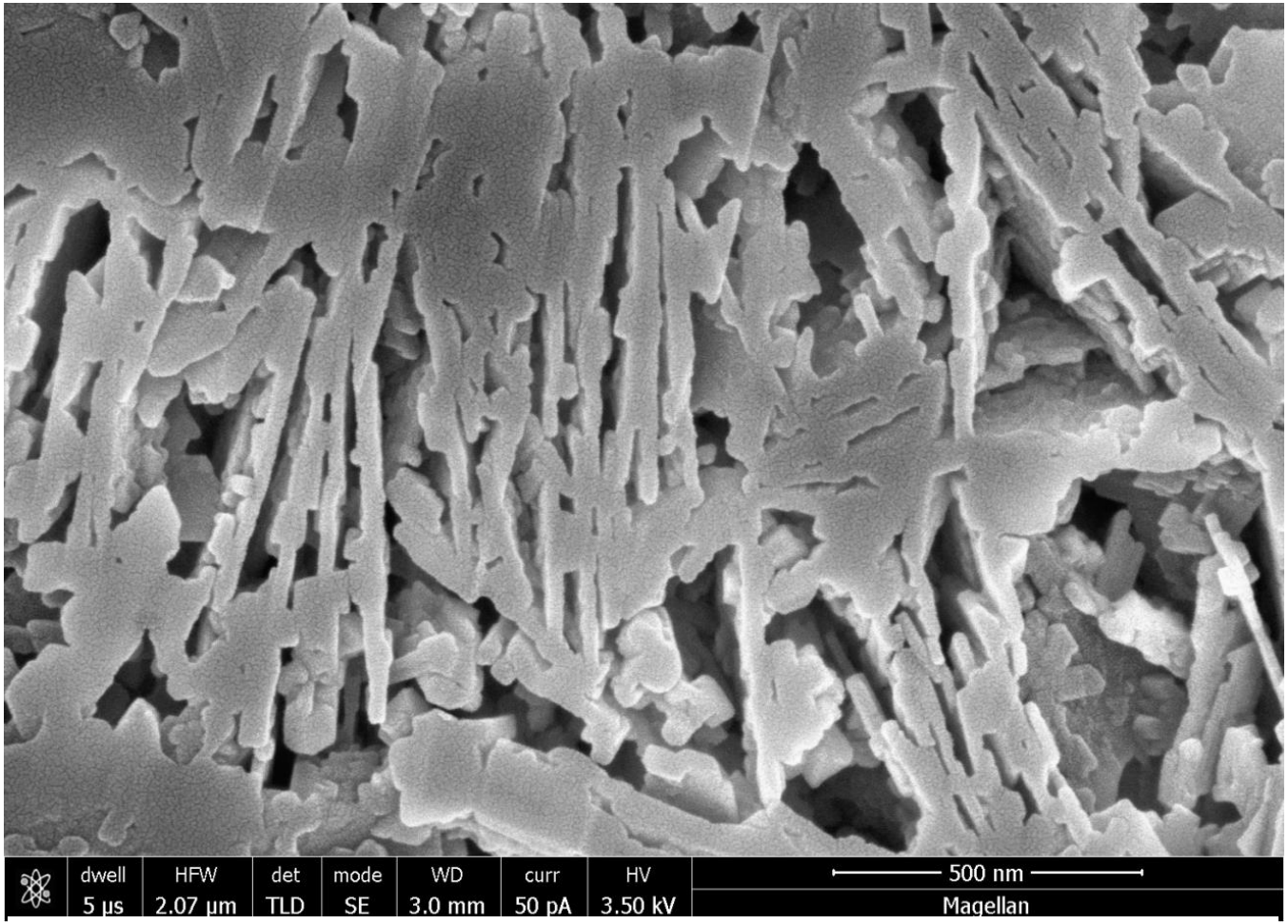

FIGURE 4.6. Elongated, bladed crytals of pal-CT and pores in the outer interlepisphere zone (VK12-5)

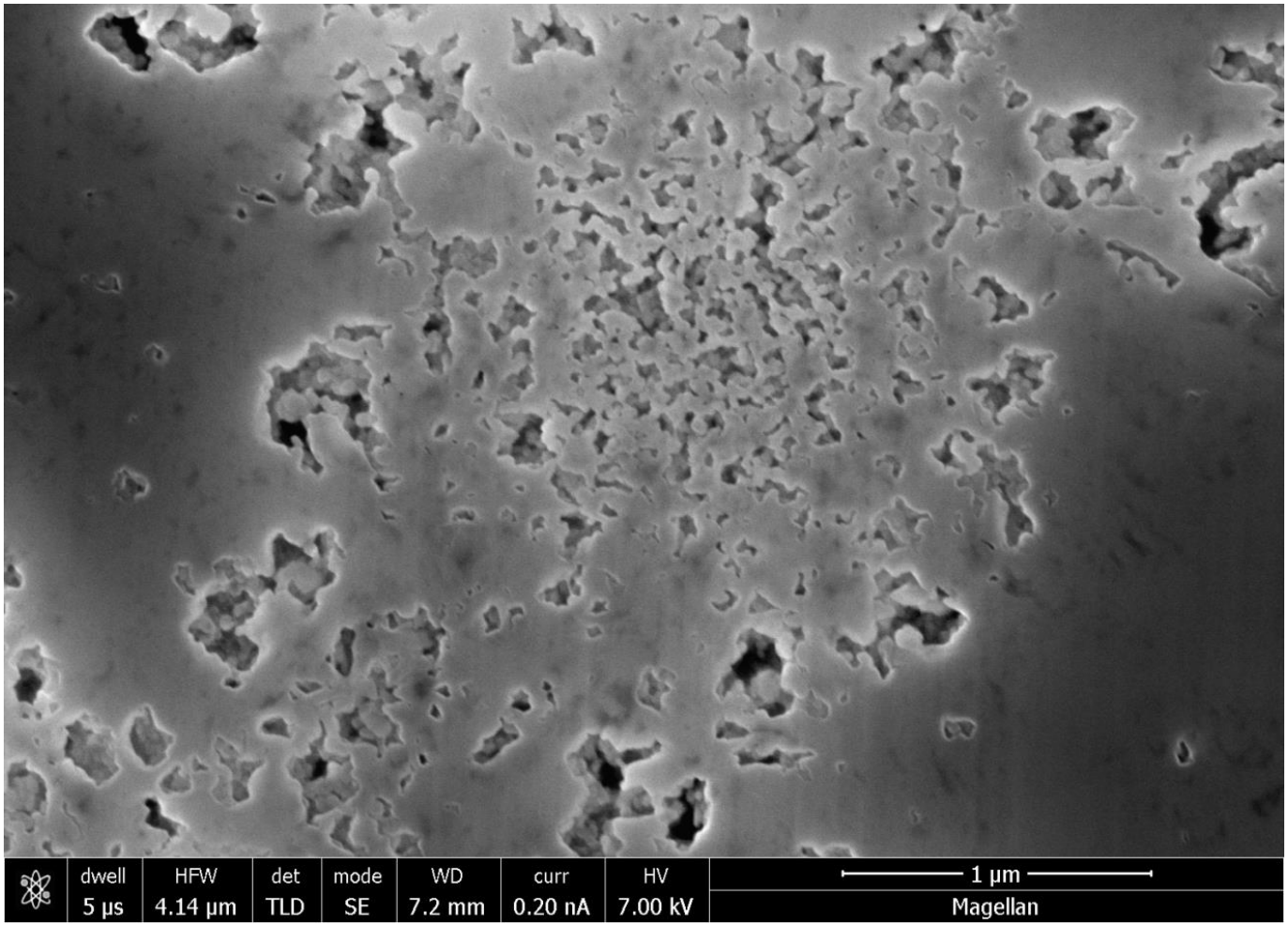

FIGURE 4.7. Lepisphere with irregular pores instead of bladed in the outer "interlepisphere". Note that in this location, the lepisphere is surrounded by mostly solid groundmass (VK12-3)

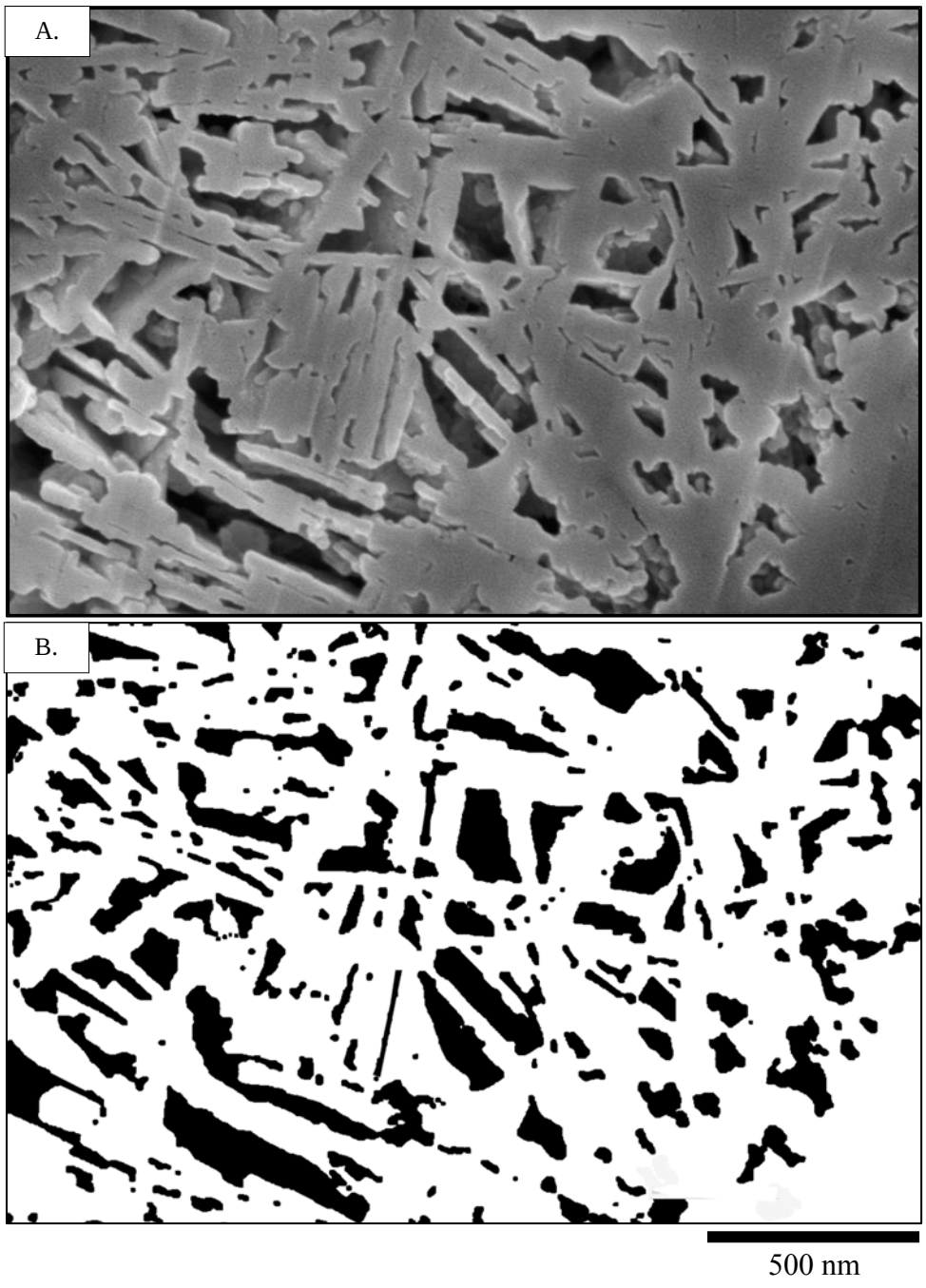

FIGURE 4.8. Images of interlepisphere pores in A. SEM and B. thresholded with ImageJ (VK12-6).

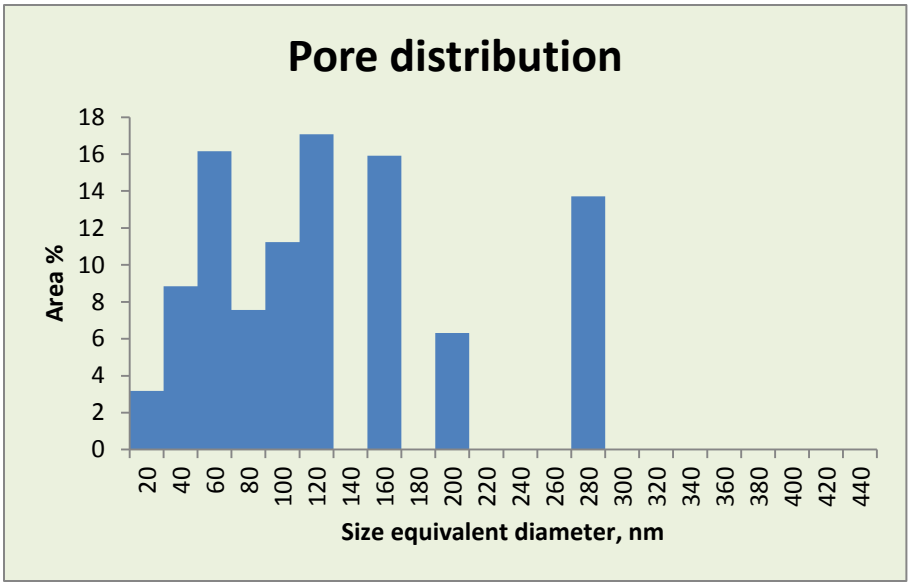

FIGURE 4.9. Pore distribution of interlepispheric pores (VK12-6).

TABLE. 4.2 Porosity, Pore Diameter and Shape Descriptors of the Interlepispheric Zone (VK12-6).

Pores: % Area	Circular equivalent diameter (nm)	Aspect Ratio	Roundness	Circularity	Solidity	Perimeter over area μm^{-1}
25.19	10-440	2.28	0.44	0.684	0.867	41.71

The interlepisphere zones are very porous, consist of larger nanopores that are elongated between bladed crystals. The rims of the mantle at the transition to interlepisphere zone have similar irregular, stubby pore shapes as in the cores. However, as they radiate outward, they become more bladed and elongated. The circular equivalent diameter of the pores range from 10-440 nm (Figures 4.7 & 8, and Table 4. 2).

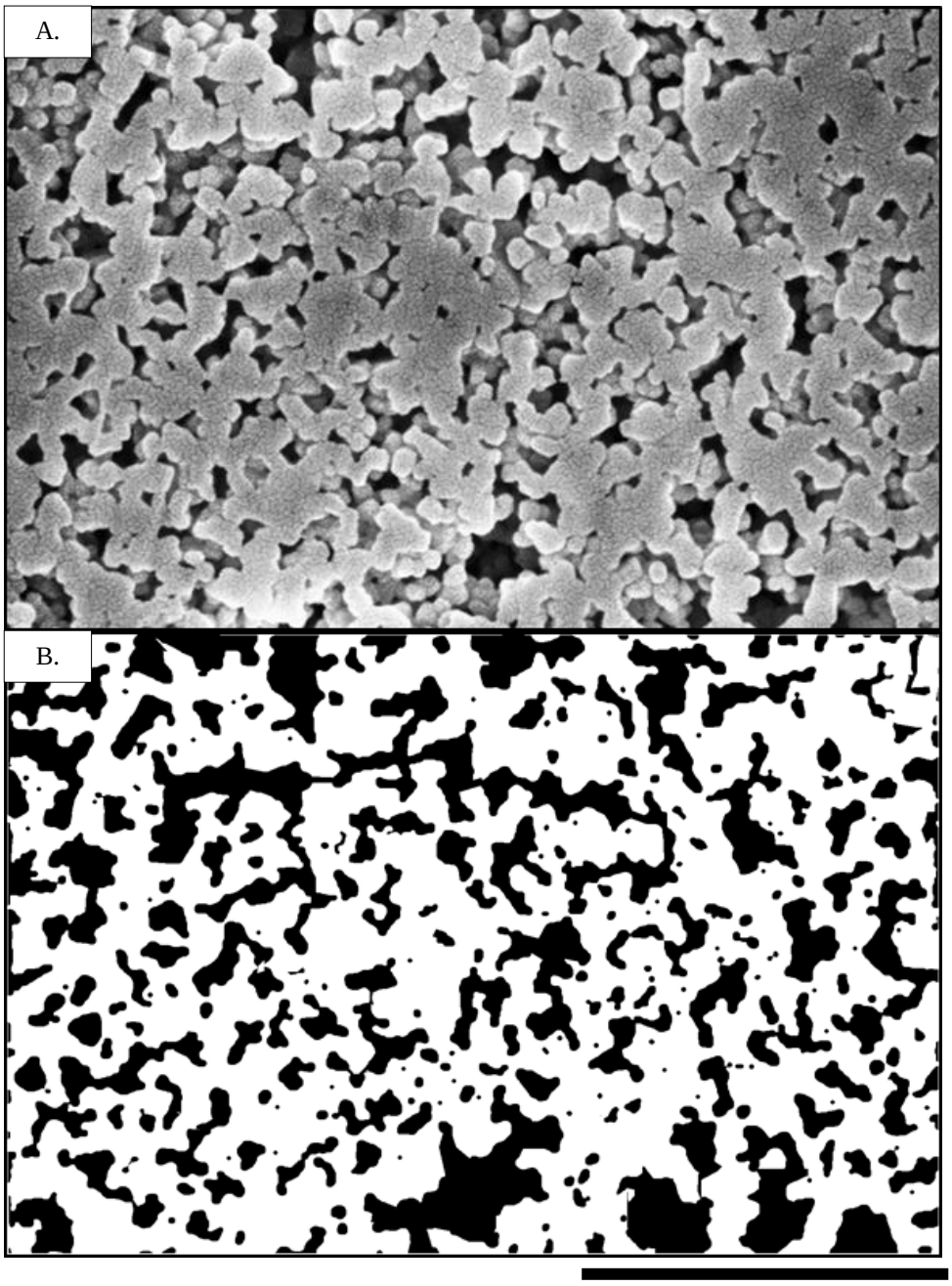

FIGURE 4.10. Images of lepispheric core pores in A. SEM and B. thresholded pores with ImageJ. Note granular and connected nature of pores in this zone (VK12-6).

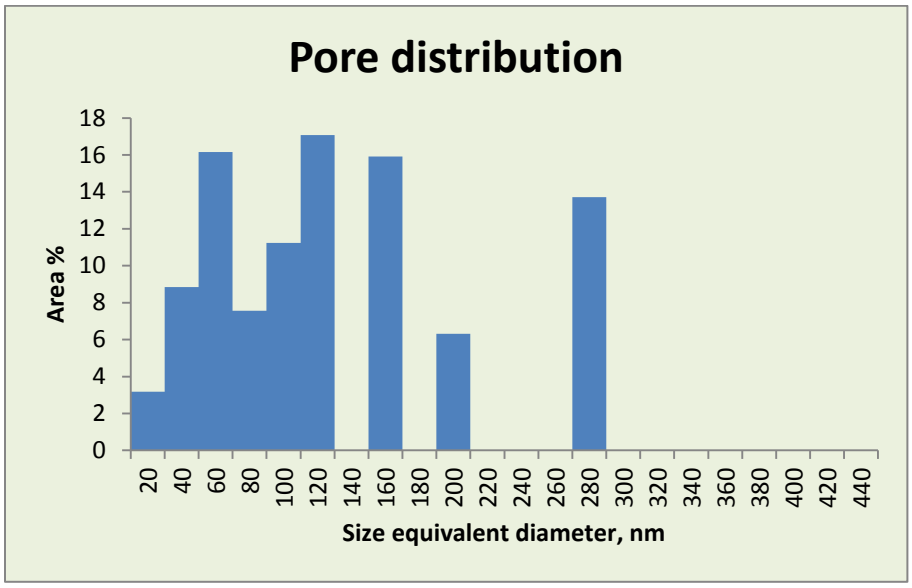

FIGURE 4.11. Pore distribution of lepispheric core pores (VK12-6).

TABLE. 4.3. Porosity, Pore Diameter and Shape Descriptors of the Core Zone (VK12-6).

Pores: % Area	Circular equivalent diameter (nm)	Aspect Ratio	Roundness	Circularity	Solidity	Perimeter over area μm^{-1}
34.38	3-280	1.90	0.53	0.702	0.844	107.30

The core is highly porous and connected. They are nanopores with intergranular shapes and the pore size ranges from 3-280 nm (Figures 4.9 &10, and Table 4.3). The virtually impermeable mantle makes the core ineffective porosity. They have elongated shape as some of the more equant primary pores are connected into single volumes.

4.1.2. Detrital-Rich Opal-CT Porcelanite

The detrital-rich opal-CT porcelanite specimen (VK12-12) is rather

homogeneous, with relatively low porosity, consisting of small pores with poor apparent connectivity (Figure 4.12).It contains nanopores ranging from 3-180 nm circular equivalent diameter (Figures 4. 12 & 13, and Table 4.4) with irregular shapes. The poor interconnection of the pores suggests that they form rather ineffective and isolated porosity.

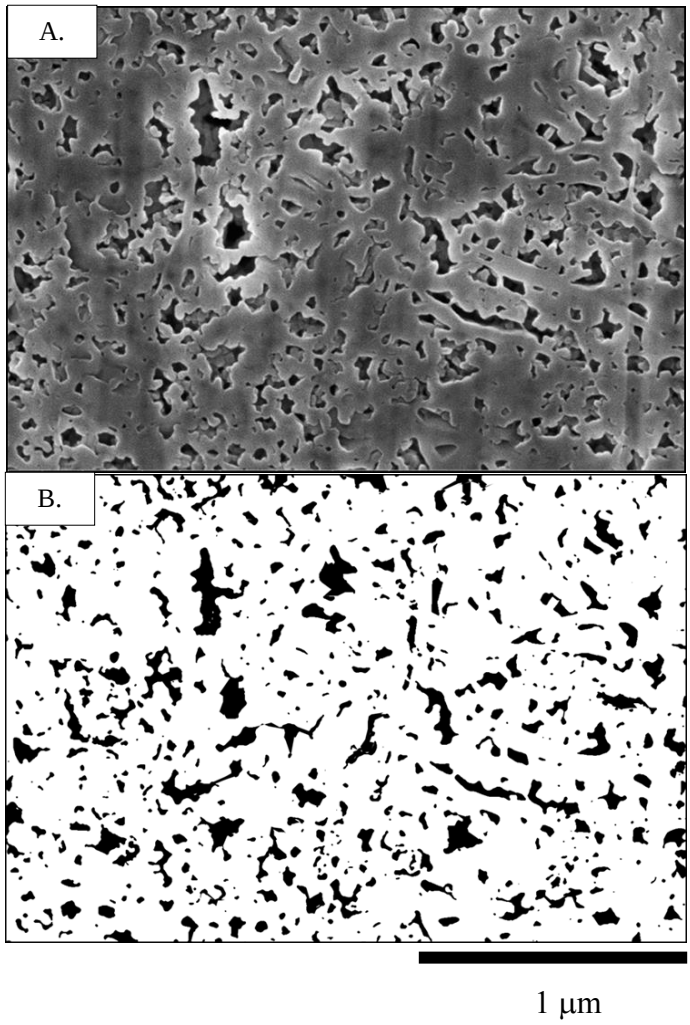

FIGURE 4.12. Images of irregular and poorly connected nanopores (VK12-11) in A. SEM and B. thresholded pores with ImageJ.

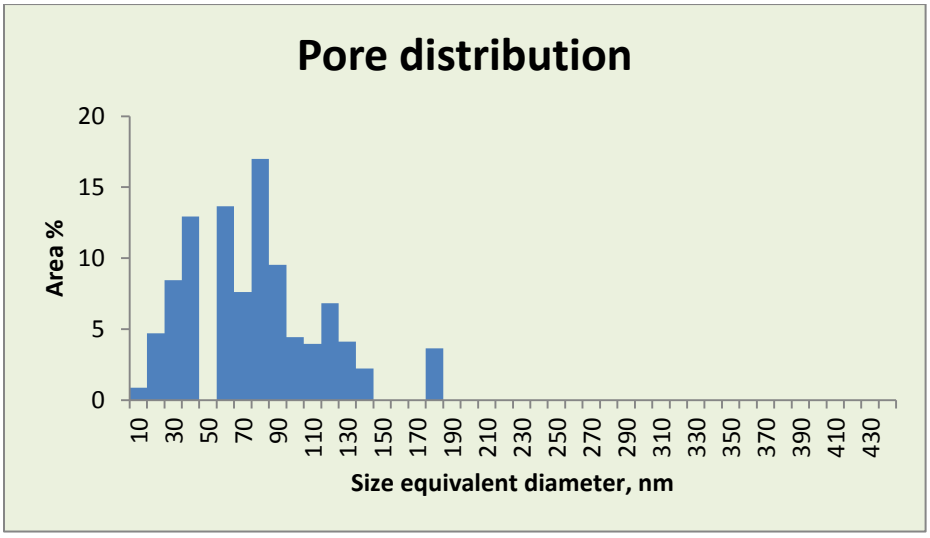

FIGURE 4.13. Pore distribution of detrital-rich porcelanite sample VK12-11.

TABLE 4.4. Porosity, Pore Diameter and Shape Descriptors for Detrital-Rich Opal-CT porcelanite (VK12-11)

Pores: % Area	Circular equivalent diameter (nm)	Aspect Ratio	Roundness	Circularity	Solidity	Perimeter over Area μm^{-1}
18.82	3-180	1.96	0.51	0.729	0.828	124.58

4.1.3. Detrital-poor opal-CT porcelanite (Transition-zone).

"Transition-zone" opal-CT porcelanites have exceeding high porosity for opal-CT phase rocks – as high as common in pure diatomites. They have large interconnected vuggy pores (Figure 4.14). The pore surfaces are not bounded by euhedral or subhedral crystal faces. These kinds of rocks are closely spatially associated on the bed- and

lamination-scale with the presence of “late quartz cherts” that are silicified at the cessation of burial or during tectonic uplift (Behl and Garrison, 1994; Behl et al., 2012).

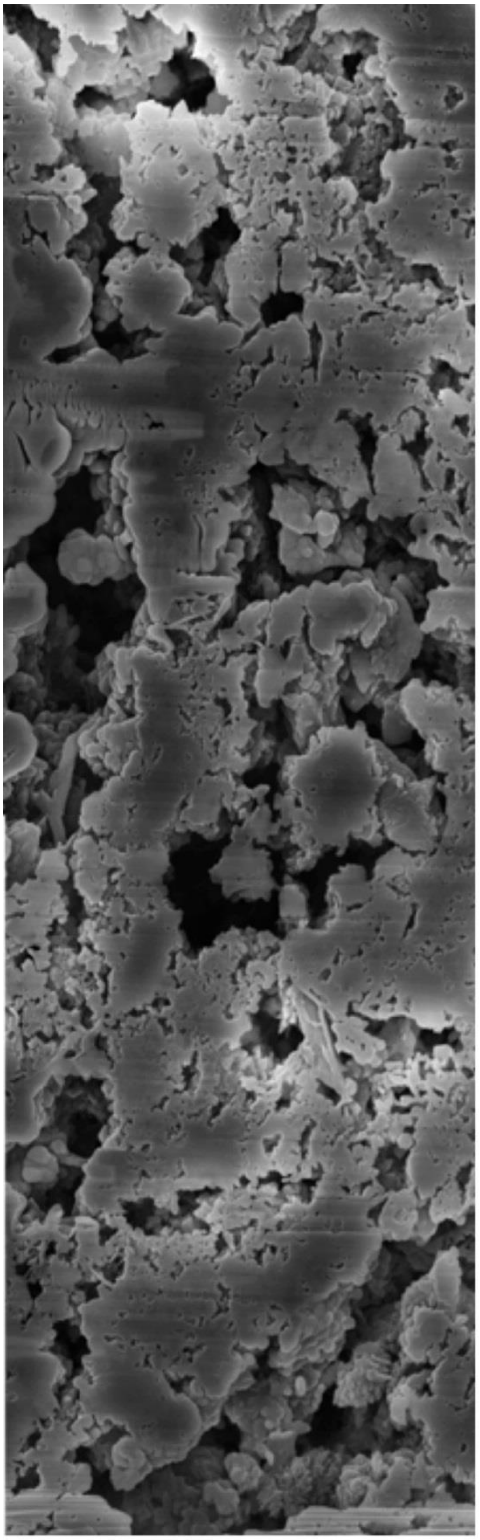

FIGURE 4.14. Transition –zone opal-CT porcelanites with large, interconnected, vuggy pores(sample VK12-178

4.2. Quartz-Phase Porcelanites

Three types of quartz-phase porcelanites were analyzed and display distinct pore system microfabrics and properties. They are: 1. detrital-poor laminated quartz porcelanite; 2. detrital-poor massive quartz porcelanite; 3. Detrital-rich quartz porcelanite.

4.2.1 Detrital-Poor Quartz laminated Porcelanite

A detrital-poor quartz porcelanite specimen (VK-12-16) was taken from a macroscopically laminated bed with ~100 μm-thick layering (Figures 4.15.A and B). Microscopically, the rock is heterogeneous with the principal variation being that laminations are defined by marked difference in porosity and pore connectivity. At this scale of investigation, lamination thickness and boundaries are quite irregular.

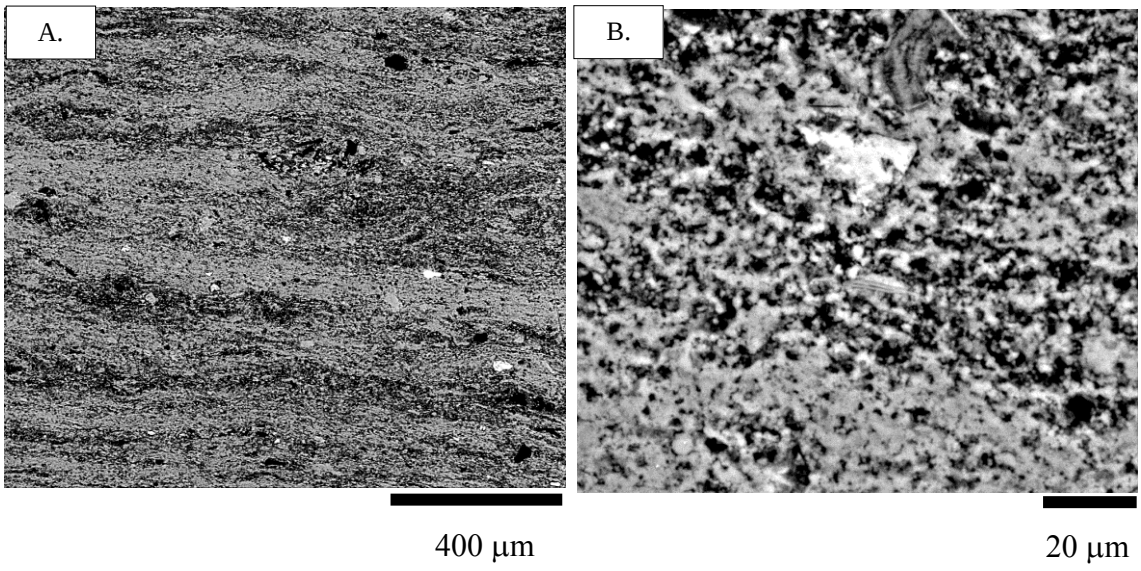

FIGURE 4.15. Epoxy-impregnated back-scattered image of laminated quartz porcelanite (Sample VK12-16). Epoxy-filled pores are black, whereas opal-CT crystals and other mineral grains are light gray to white. A. low maginification to show laminations. B. higer magnification to show pores.

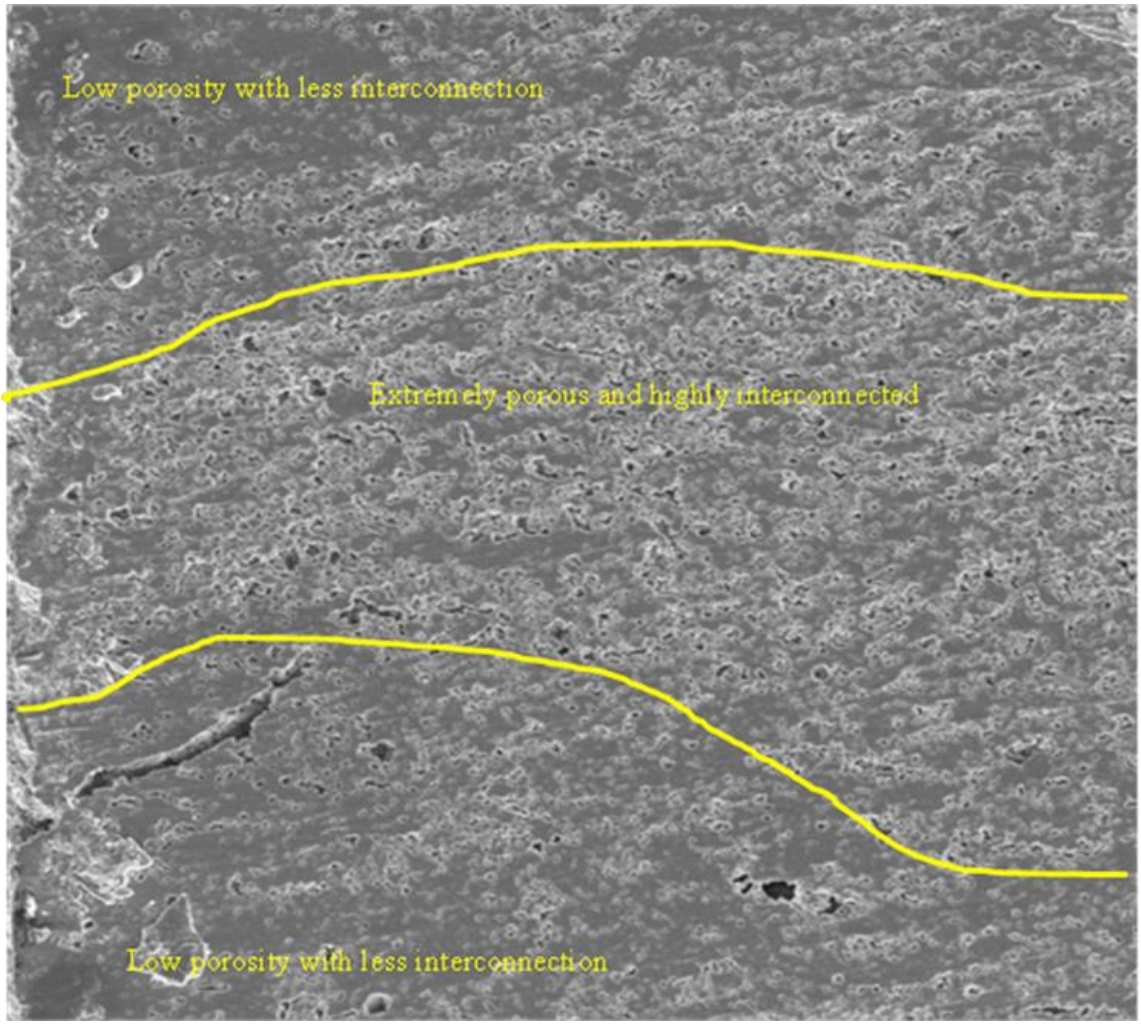

FIGURE 4.16. Secondary electron image of detrital-poor, laminated quartz porcelanite displaying layered hetrogenity of porosity.

4.2.1.1. Detrital-poor laminated quartz porcelanite (high-porosity lamination zones) with extremely large pores of highly interconnection. Note zone shown in the center of Figure 4.16. This highly porous zone (irregular lamination) has very highly connected large (> 1 micron) pores with irregular shape. Pore-throat diameters are almost

micrometer-scale (Figure 4.17 and 17). Some pore walls show subhedral to euhedral crystal form, but others are irregular or anhedral (Figure 4.18 and 17).

For the highly porous lamination, the pore size ranges from 0.4-3.0 micrometer (Figure 4.19 & 20, and Table 4.5). One extremely large (6.8 microns) size measurement is due to the connection of the pores. Pores have irregular overall shapes and the aspect ratio is high due to high connection of mostly separated pores.

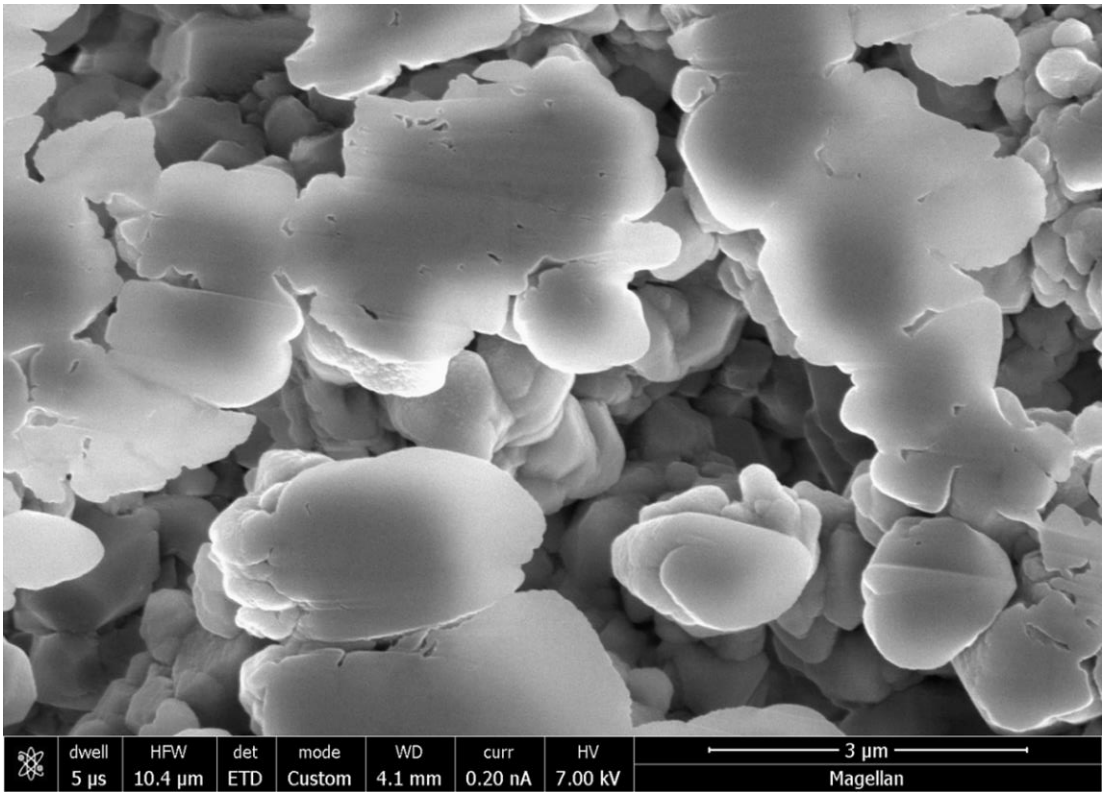

FIGURE 4.17. Secondary electron image showing subhedral to euhedral quartz crystal form of pore walls with large pore-throat diameter.

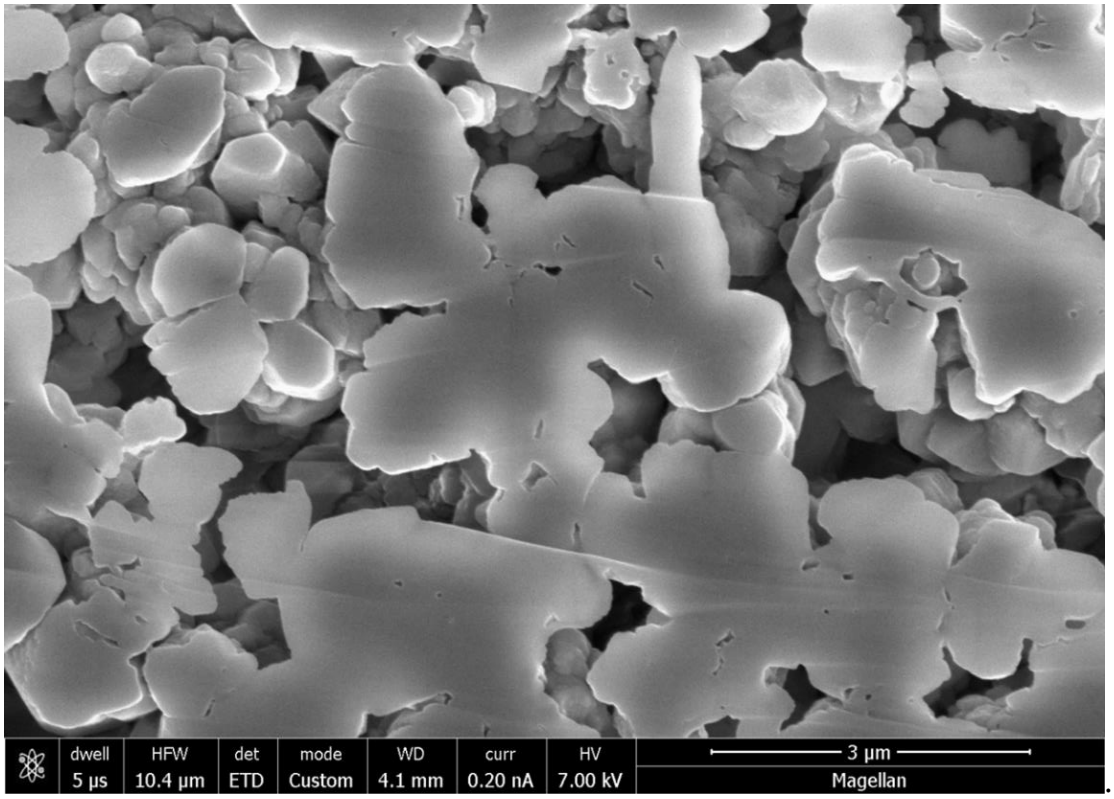

FIGURE 4.18. Secondary electron image showing subhedral to euhedral quartz crystal form and resulting pore structure.

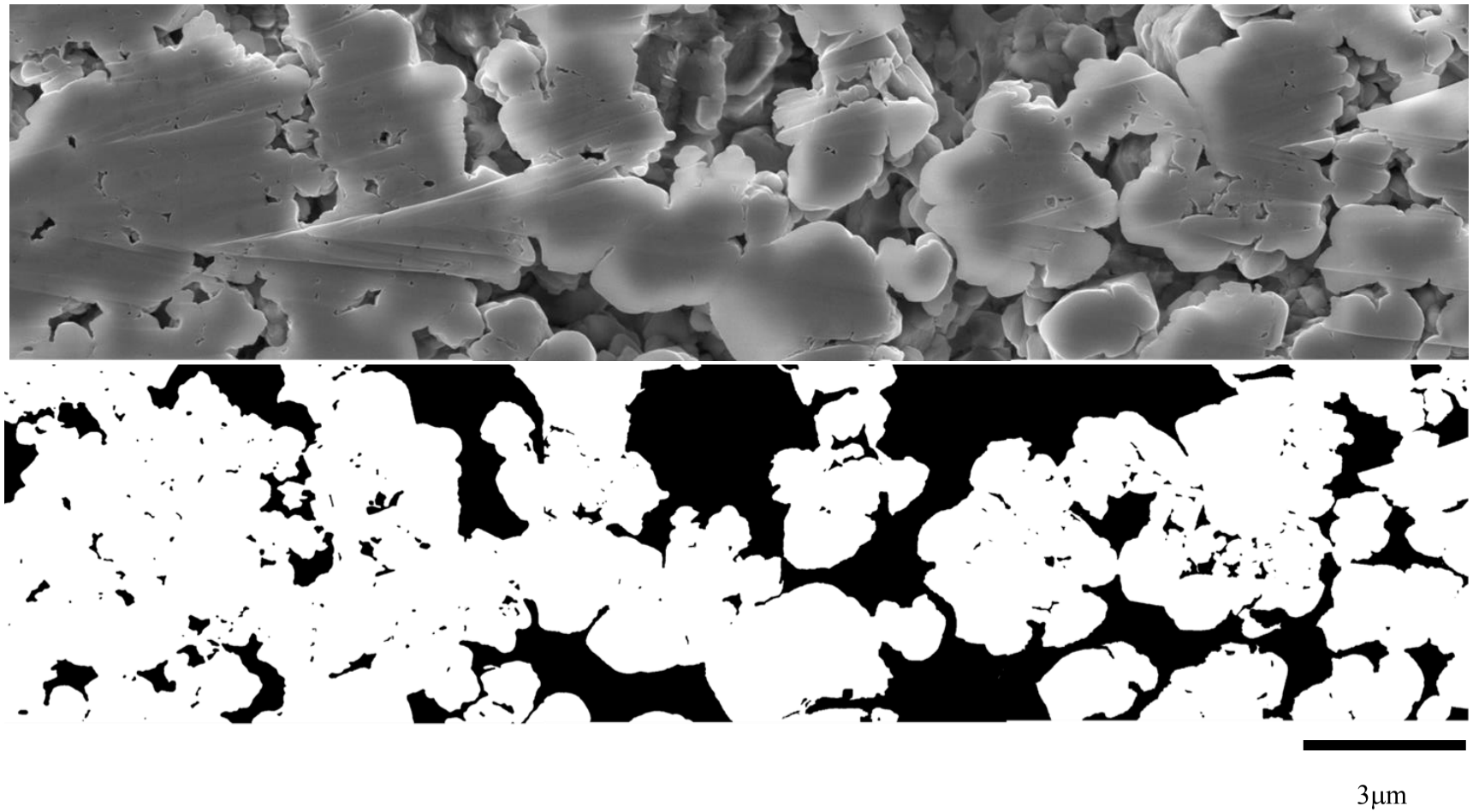

FIGURE 4.19. Secondary electron image and its thresholded pore image.

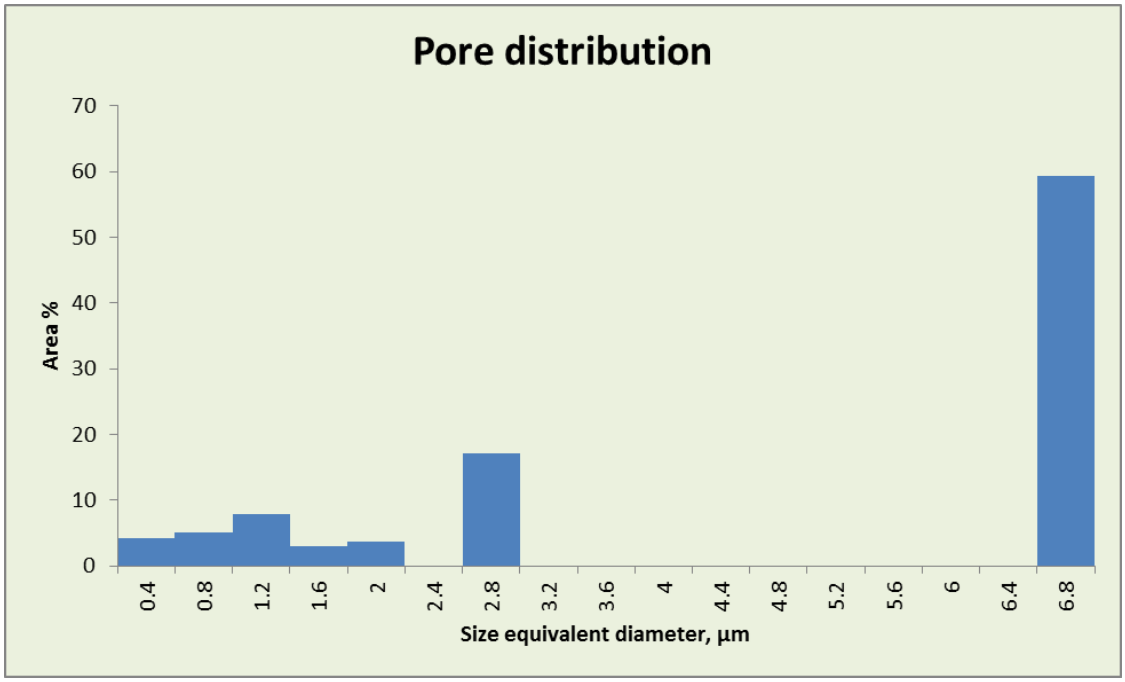

FIGURE 4.20. Pore distribution of the extremely porous zone in laminated quartz-phase porcelanite (Sample VK12-16).

TABLE 4.5. Porosity, Pore Diameter and Shape Descriptors of Detrital-Poor Quartz Porcelanite of the Extremely Porous Zone (Laminated) (VK12-16).

Pores: % Area	Circular equivalent diameter (nm)	Aspect Ratio	Roundness	Circularity	Solidity	Perimeter over Area μm^{-1}
28.50	400-3000	2.03	0.49	0.672	0.793	6.13

The analyzed part of the low-porosity laminated zones have low porosity with spatially heterogeneous pore-size (Figures 4.21 A and B). The pores are nano to

micrometer size and segregated into sub-zones with larger and smaller pores. Overall, they have poor apparent connectivity resulting in isolation of many pores.

The areas with relatively smaller pores vary from 3-600 nm in effective diameter (Figure 4.22.A, B & 23, and Table 4.6), are of irregular shapes and almost completely isolated from each other by solid microcrystalline quartz matrix.

The portions with larger pores have circular pore diameter that range from 17 nm to 2.254 micrometers (Figure 4.24, 25 & 26, and Table 4.7).The areas with large pores are mostly surrounded by nearly solid matrix with only dispersed and isolated smaller pores (Figure 4. 24). The pore sizes are quite heterogeneous and the pores have poor connectivity (Figure 4.24). Pore walls are formed of subhedral to anhedral quartz crystals (Figure 4.24), but in general pore-shapes are irregular.

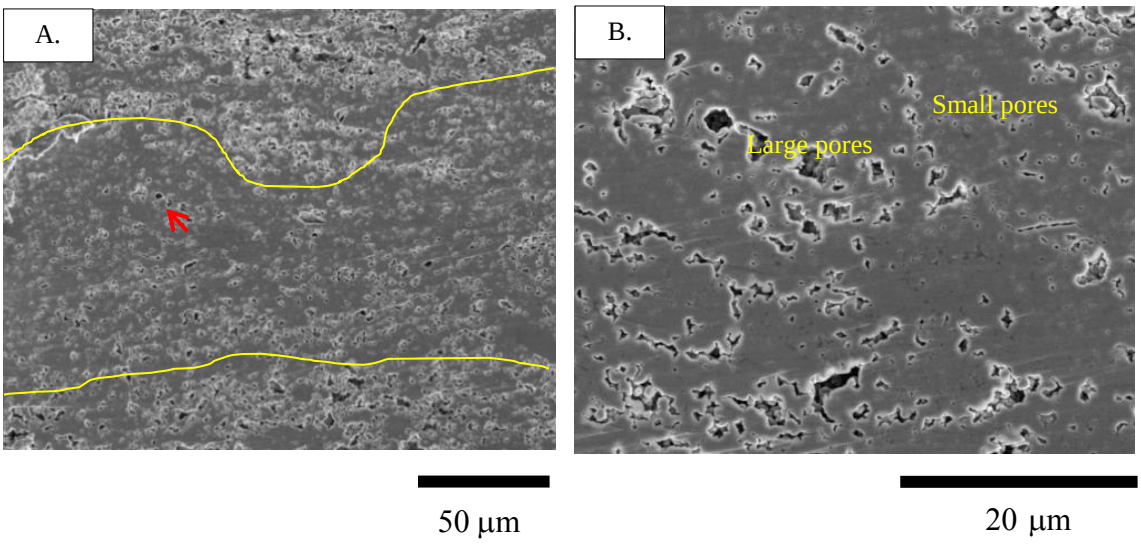

FIGURE 4.21.A & B. The low-porosity layers in laminated quartz porcelanite showing heterogeneous porosity and poorly connected pores.

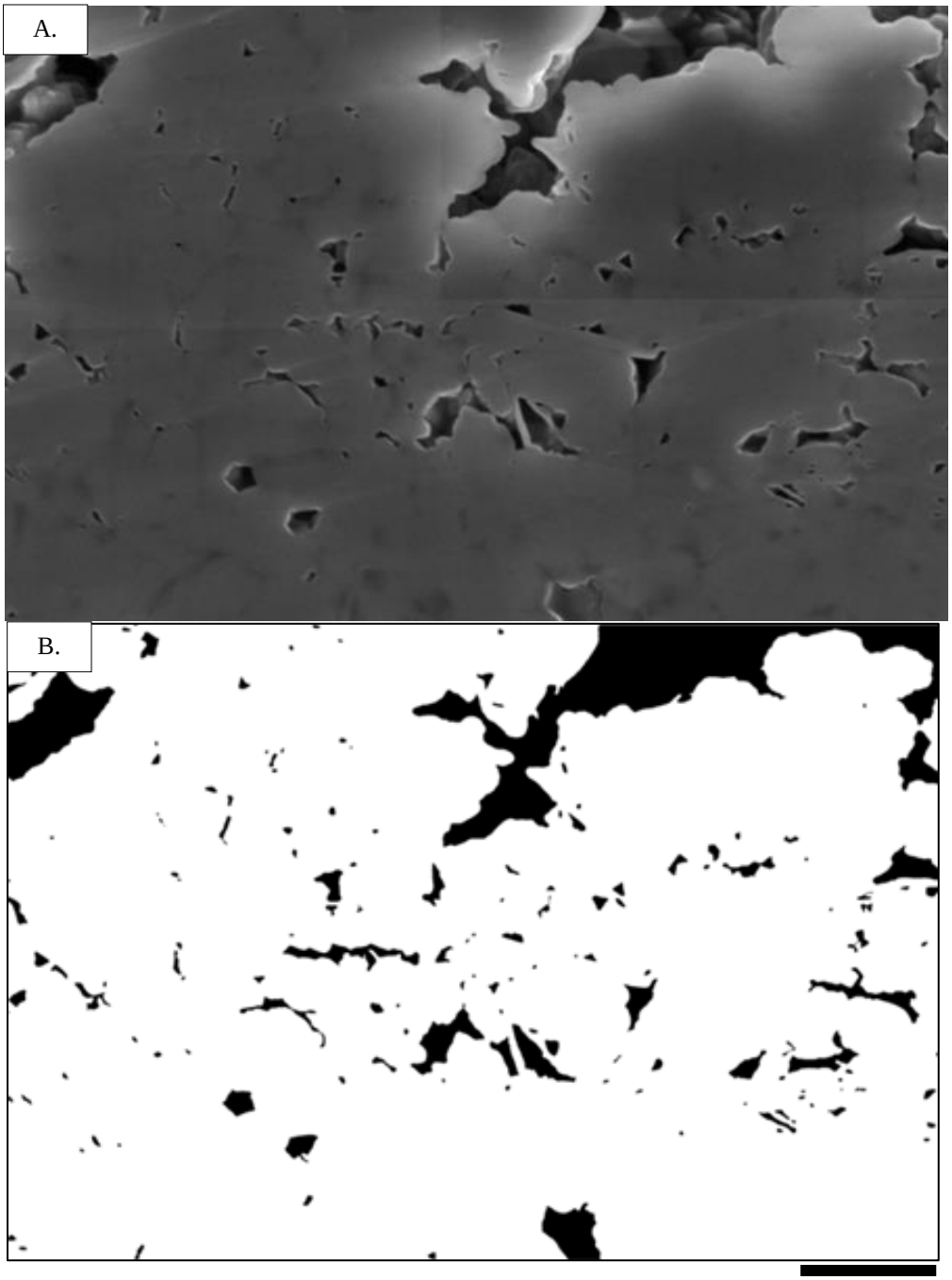

FIGURE 4.22.A and B. Areas of low-porosity lamination zones with primarily small pores that are poorly connected in quartz porcelanite and thresholded nanopores to micrpores.

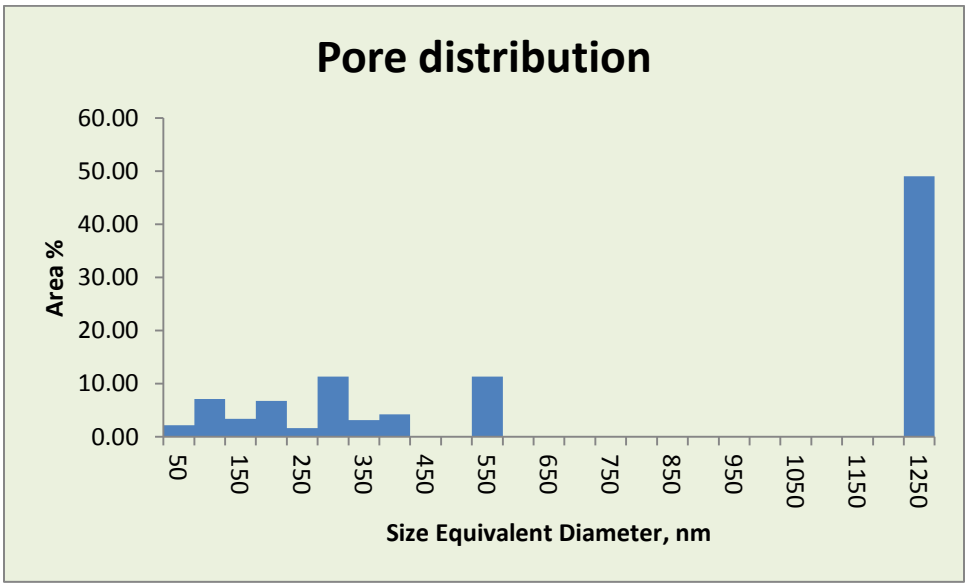

FIGURE 4.23. Pore distribution in the small-pore zone of low-porosity laminations of quartz porcelanite (VK12-16).

TABLE 4.6. Porosity, Pore Diameter and Shape Descriptors of Laminated Detrital-Poor Quartz Porcelanite of the Small Pores Zone of the Low Porosity Lamination (VK12-16).

Pores: % Area	Circular equivalent diameter	Aspect Ratio	Roundness	Circularity	Solidity	Perimeter over area μm^{-1}
8.89	3-1250	2.31	0.43	0.647	0.818	26.89

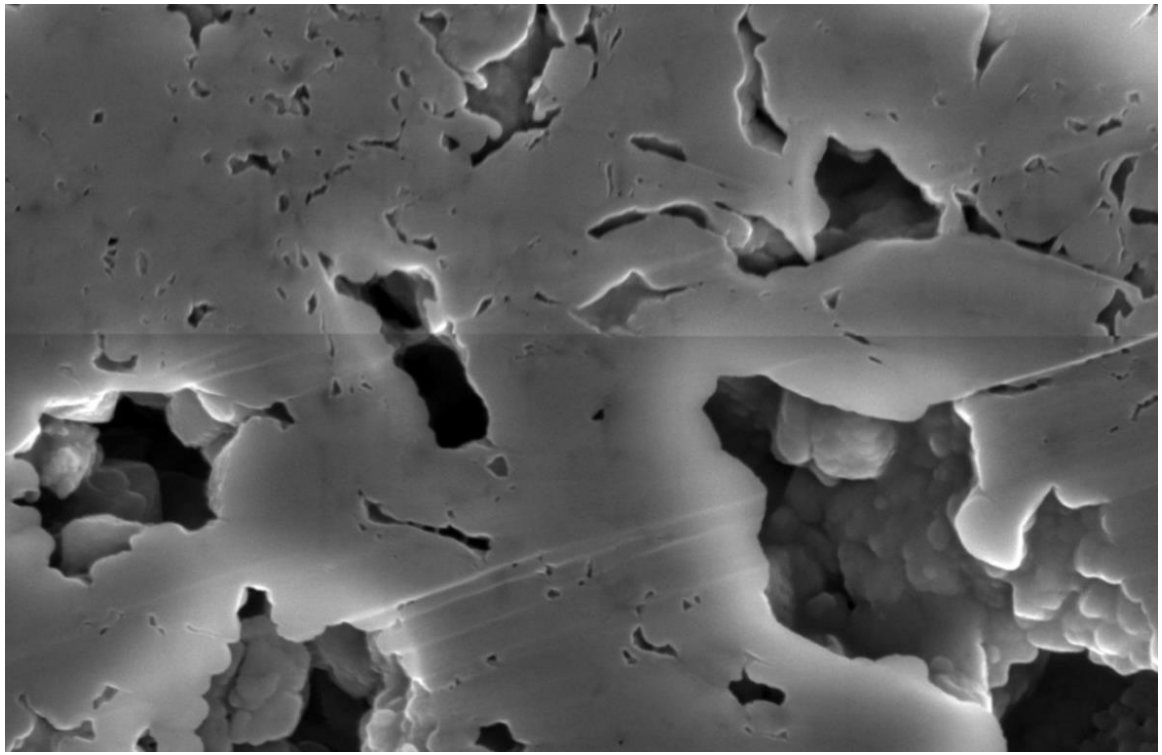

FIGURE 4.24. Areas of low-porosity lamiinations with larger pores in quartz porcelanite.

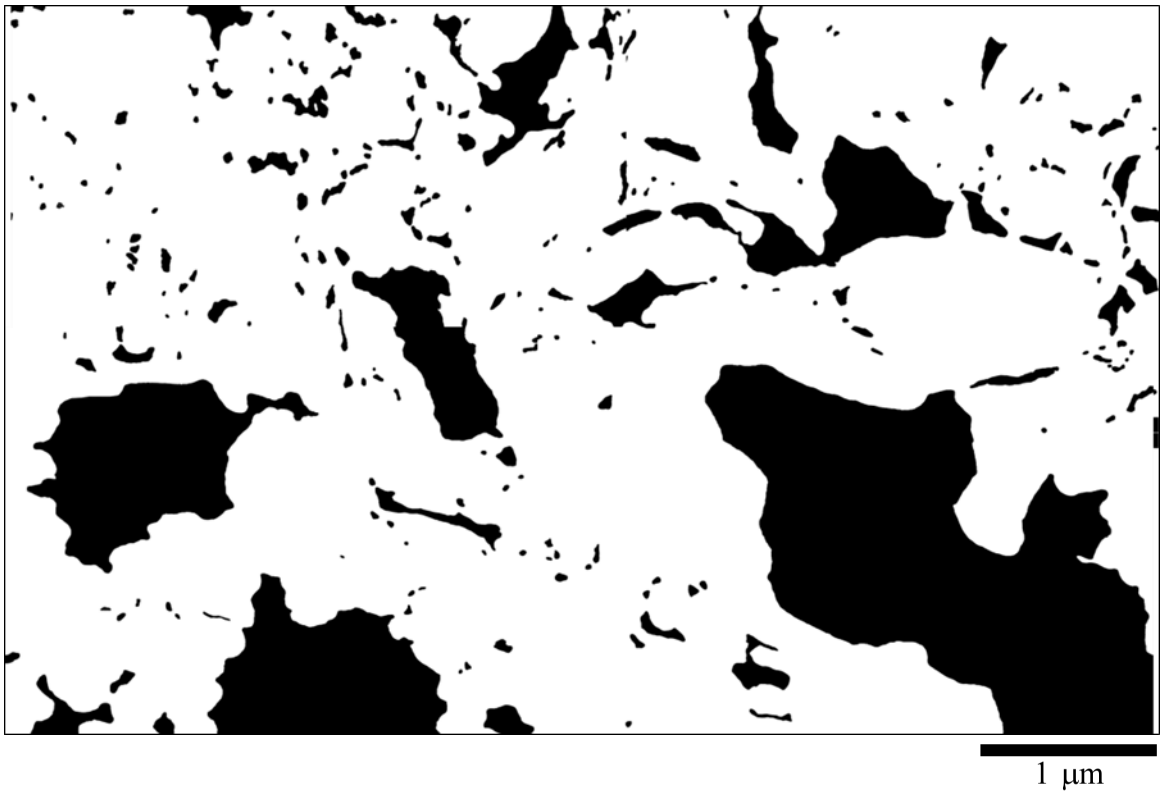

FIGURE 4.25. Thresholded nanopores to micrpores in the areas of low-porosity lamination with larger pores in quartz porcelanite with large pores (VK12-16). Note the poor connectivity of pores.

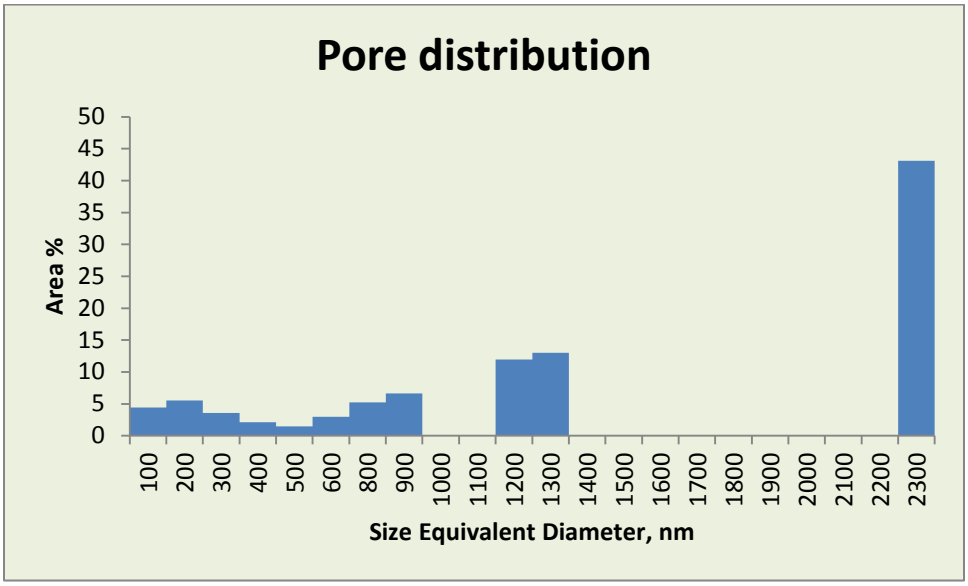

FIGURE 4.26. Pore distribution of low porosity areas of laminated quartz porcelanite with relatively large pores (VK12-16).

TABLE 4.7. Porosity, Pore Diameter and Shape Descriptors of Laminated Detrital-Poor Quartz Porcelanite of the Low Porous Zones with Relatively Larger Pores (VK12-16)

Pores: % Area	Circular equivalent diameter (nm)	Aspect Ratio	Roundness	Circularity	Solidity	Perimeter over area
24.82	17 - 2.254	2.17	0.46	0.696	0.858	12.18

4.2.1 Detrital-Poor Massive Quartz Porcelanite

Macroscopically massive porcelanite beds with low-detritus composition frequently have patchy to indistinct laminations of detritus when examined by SEM (Figures 4.27 and 4.28). The patchy to indistinct laminations of detritus contain primary and authigenic clays and creates a heterogeneous and discontinuous composition, microstructure and porosity (Figures 4.29 and 4.30). This mineralogic heterogeneity contributes to the generation of minor artifacts (striations) during polishing that need to be minimized during image analysis and quantification (Figure 4.30). In general, the rock fabric can be divided into a relatively homogeneous matrix and separate lenses or patches. Figure 4.30 shows the zone of the lenticular patches with some primary and authigenic clays. The pores are of irregular shapes and heterogeneous pore size ranging from 50 to 800 nanometer (Figures 4. 31, 32 &33, and Table 4.8). They have anhedral crystal shapes on the pore walls.

Figures 4.34 and 4.35 show the secondary electron images of the massive quartz-phase porcelanite with patchy to indistinct laminations of detritus, and the part that is analyzed for massive matrix (indicated by arrow) at different magnifications. The pores in the massive detrital-poor intervals tend to have sharp edges following the euhderal crystal shapes (Figure 4. 36). The massive matrix has isolated nano- to micropores with some authigenic clays within the angular, intercrystalline pores (Figure 4.37). The nanopore to micropore in size pores are only partially connected and are surrounded by a non-porous impermeable quartz (Figure 4.37). The pores are of irregular shapes with heterogeneous pore size ranging from 3 to 1715 nanometer (Figure 4.37, 38 & 39 and

Table 4.9). The detrital-rich areas have pores of more irregular shapes. Both areas have isolated pores with poor interconnectivity.

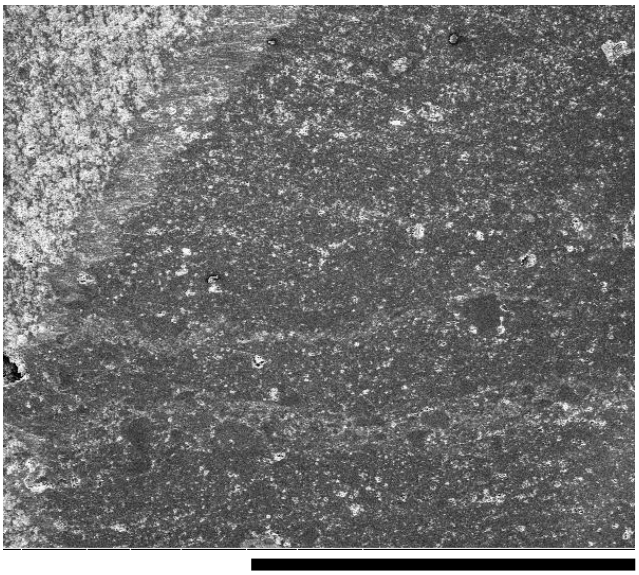

FIGURE 4.27. Secondary electron images of the massive quartz-phase porcelanite

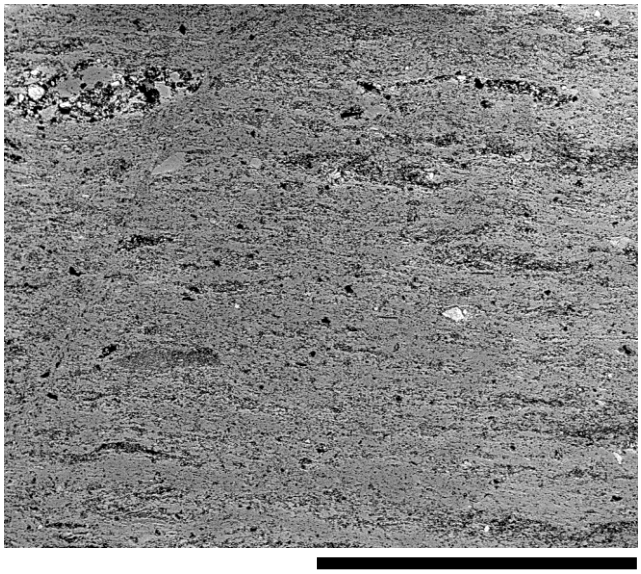

FIGURE 4.28. Backscattered images of the massive quartz-phase porcelanite. Note lenticular patches of higher porosity.

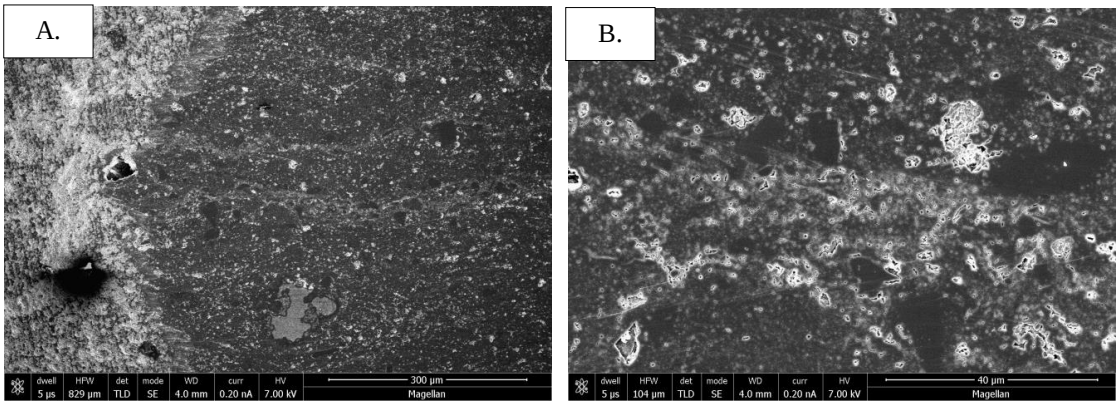

FIGURE 4.29. A. Secondary electron images of the massive quartz-phase porcelanite. A. With patchy to indistinct laminations of detritus, and B. the middle part that has the analyzed lenticular patch in high magnification.

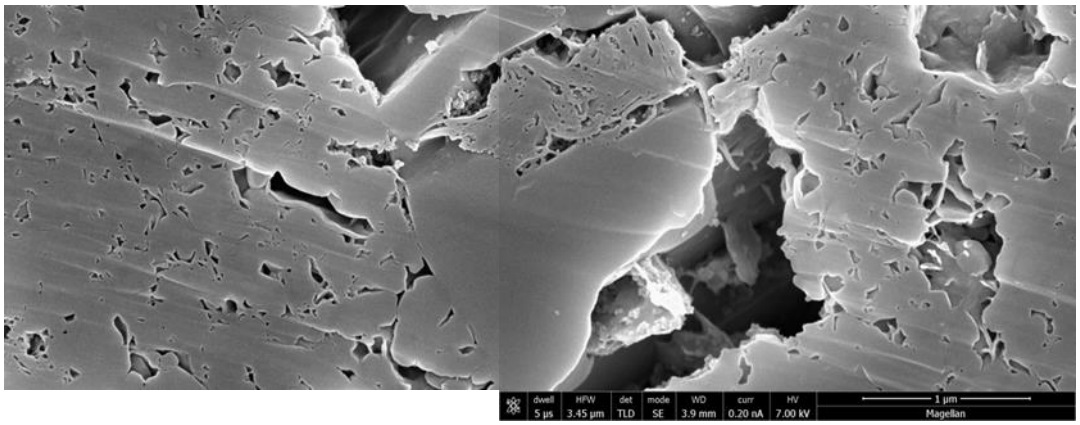

FIGURE 4.30. Part of the analyzed lenticular patch displaying clays in high magnification.

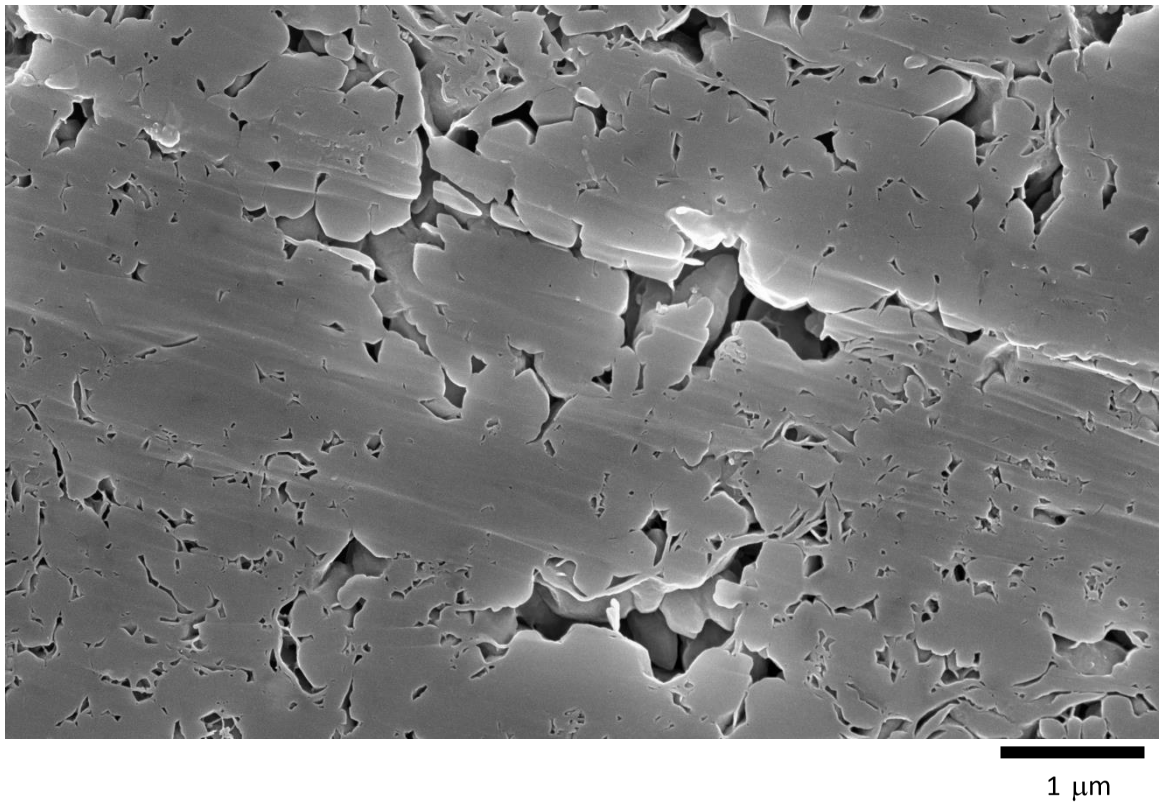

FIGURE 4.31. Patchy to indistinct laminations of detritus.

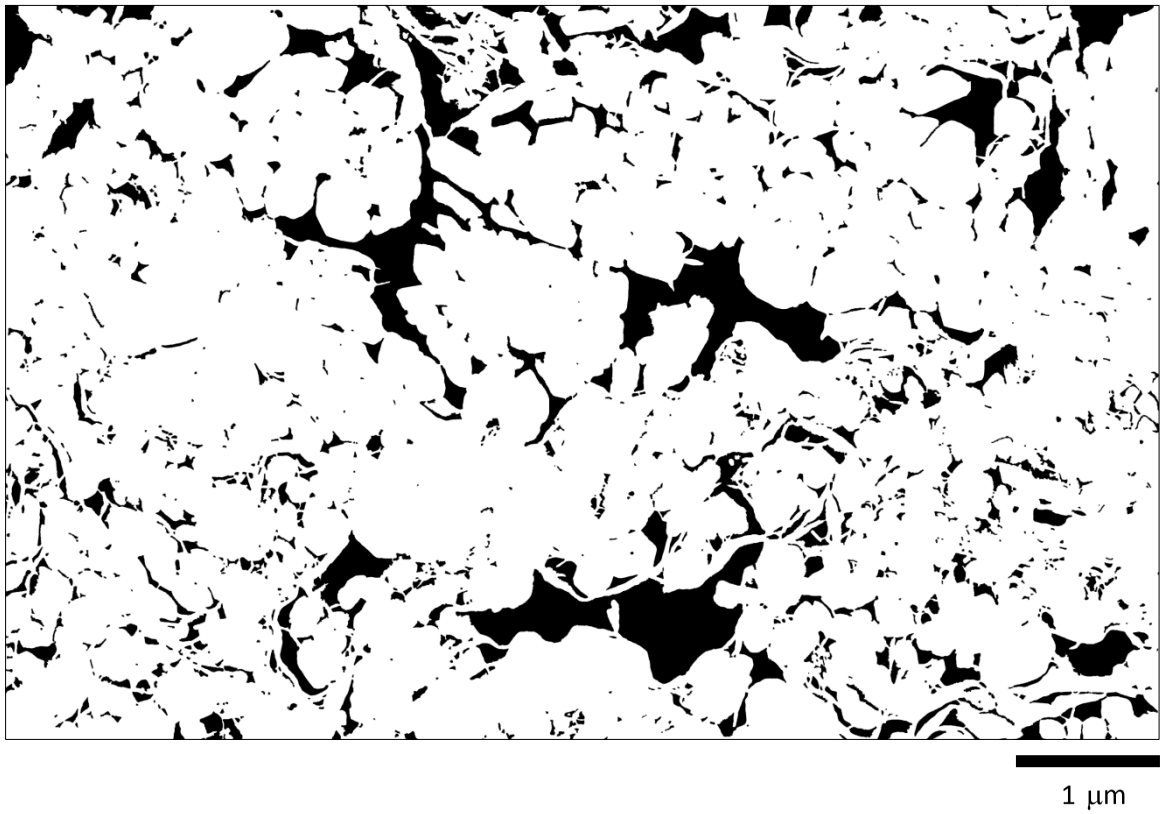

FIGURE 4.32. Thresholded image of sample VK-12-15.

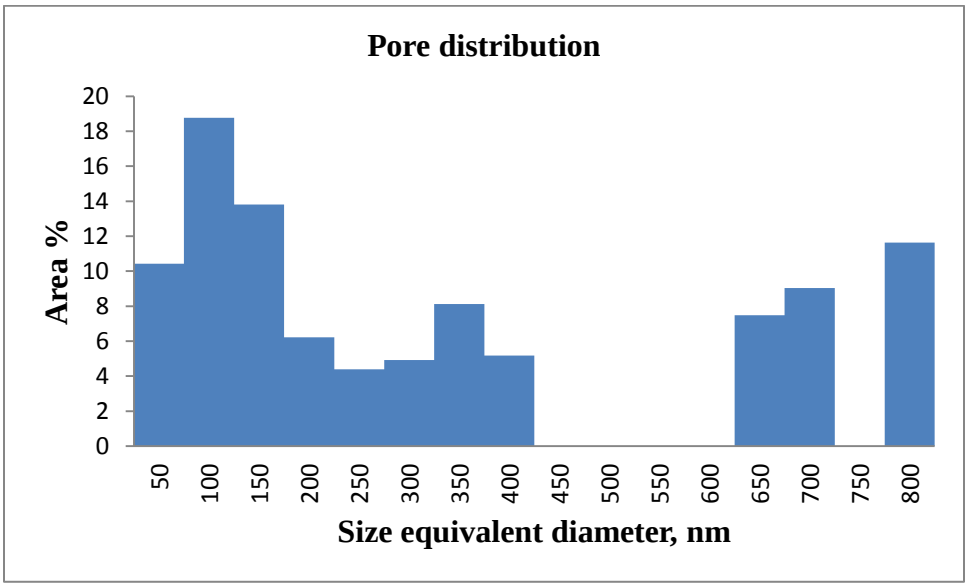

FIGURE 4. 33. Pore distribution of sample VK12-15 of the patches.

TABLE 4.8. Porosity, Pore Diameter and Shape Descriptors of Massive Detrital-Poor Quartz Porcelanite within the Patches (VK12-15)

Pores: % Area	Circular equivalent diameter (nm)	Aspect Ratio	Roundness	Circularity	Solidity	Perimeter over area μm^{-1}
14.45	5-758	1.96	0.51	0.603	0.775	66.68

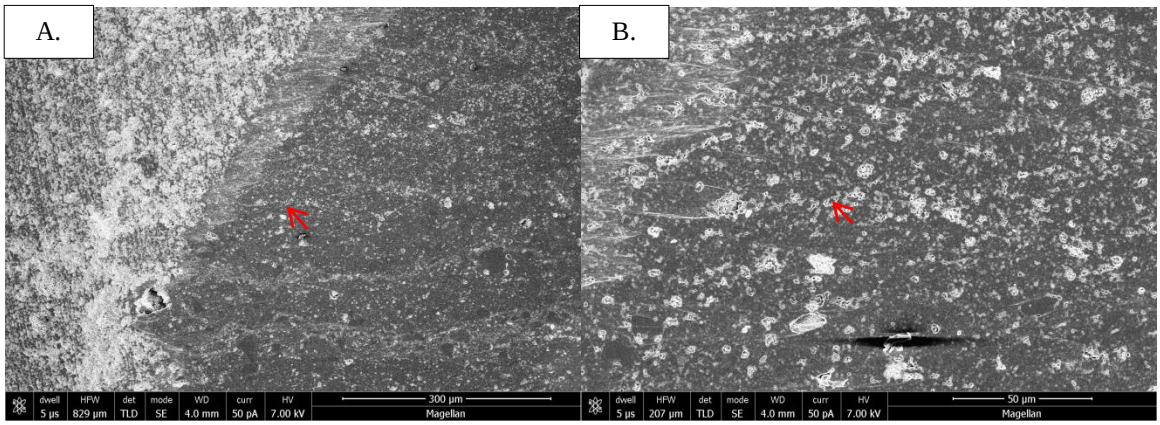

FIGURE 4.34. A. Secondary electron images of the massive quartz-phase porcelanite. A. Darker section in right 2/3's is polished surface that displays patchy to indistinct laminations of detritus. B. The analyzed portion of massive porcelanite (indicated by arrow) in higher magnification.

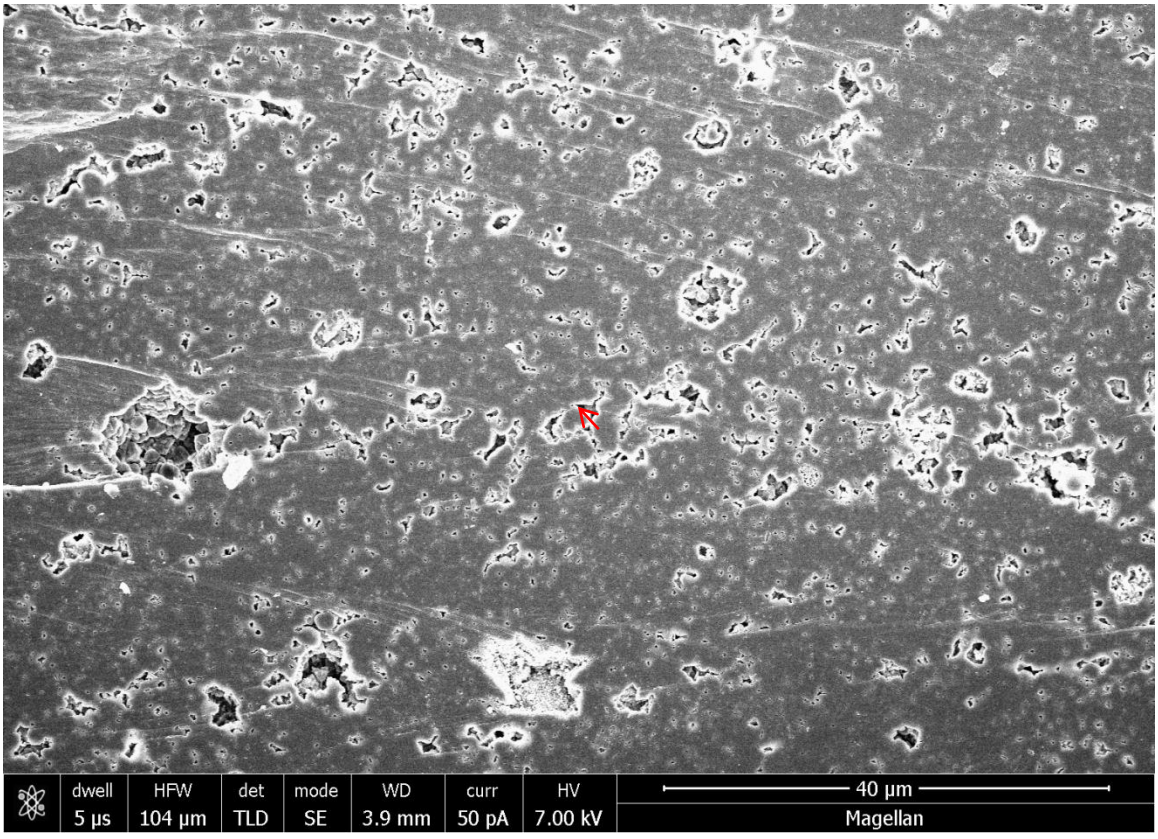

FIGURE 4.35. A. Secondary electron images of the massive quartz-phase porcelanite displaying the analyzed part of massive matrix (indicated by arrow) in high relatively magnification.

The pore walls within the areas of massive matrix is formed by quartz crystals with euhedral to anhedral shapes (Figure 4.35, 4.36 and 4.37). The pores have sharp edges following the crystal shapes (Figure 4.36 and 4.37). They have dispersed authegenic clays attached to the quartz crystals (Figure 4.36 and 4.37). The pores are of irregular shapes and nanopore to micropore in size (Figures 4. 37, 38 & 39, and Table 4.8).

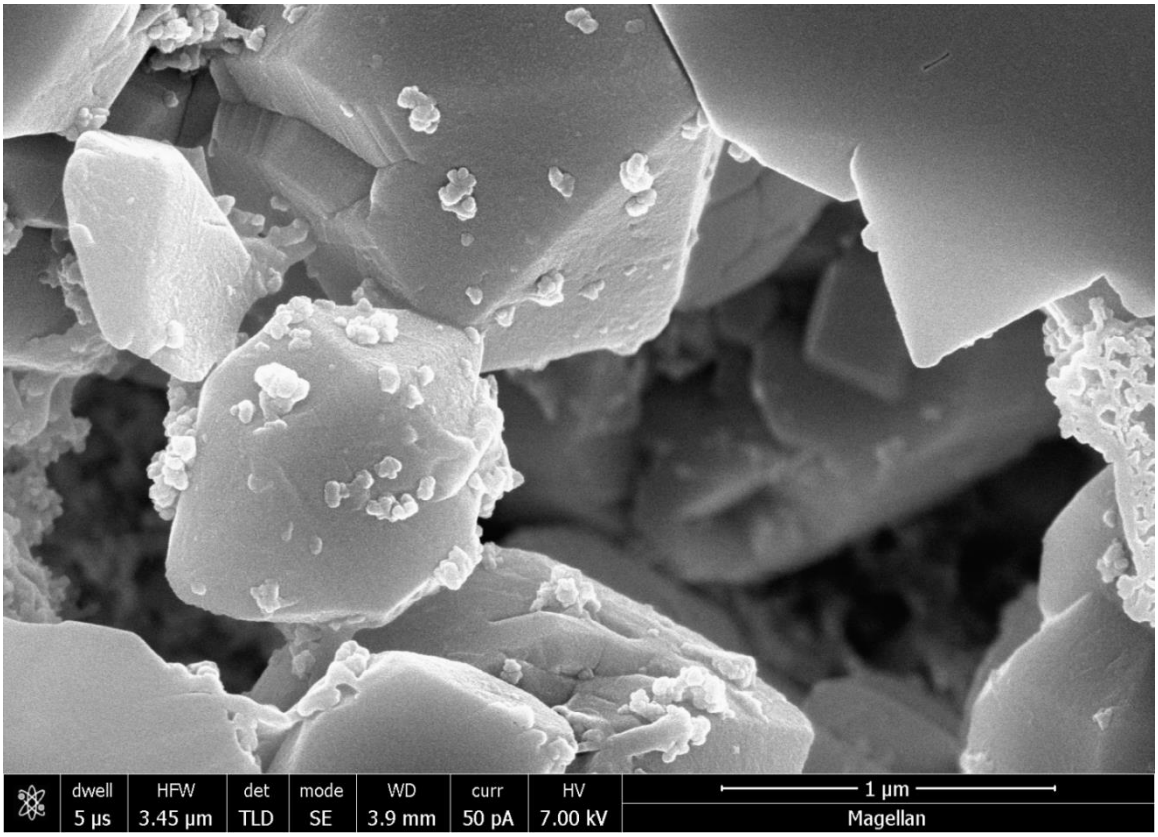

FIGURE 4.36. Secondary electron image of the massive quartz-phase with some authigenic clays.

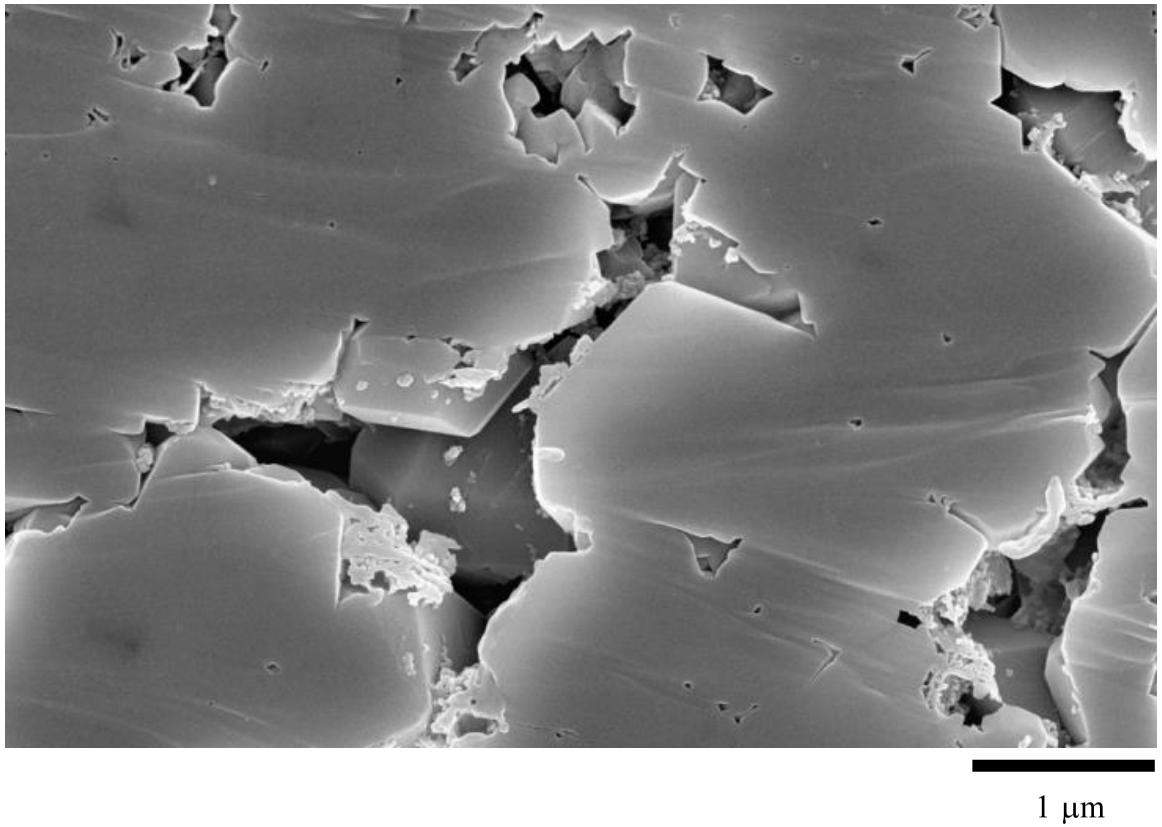

FIGURE 4.37. Secondary electron image of massive matrix of the detrital-poor quartz-phase porcelanite

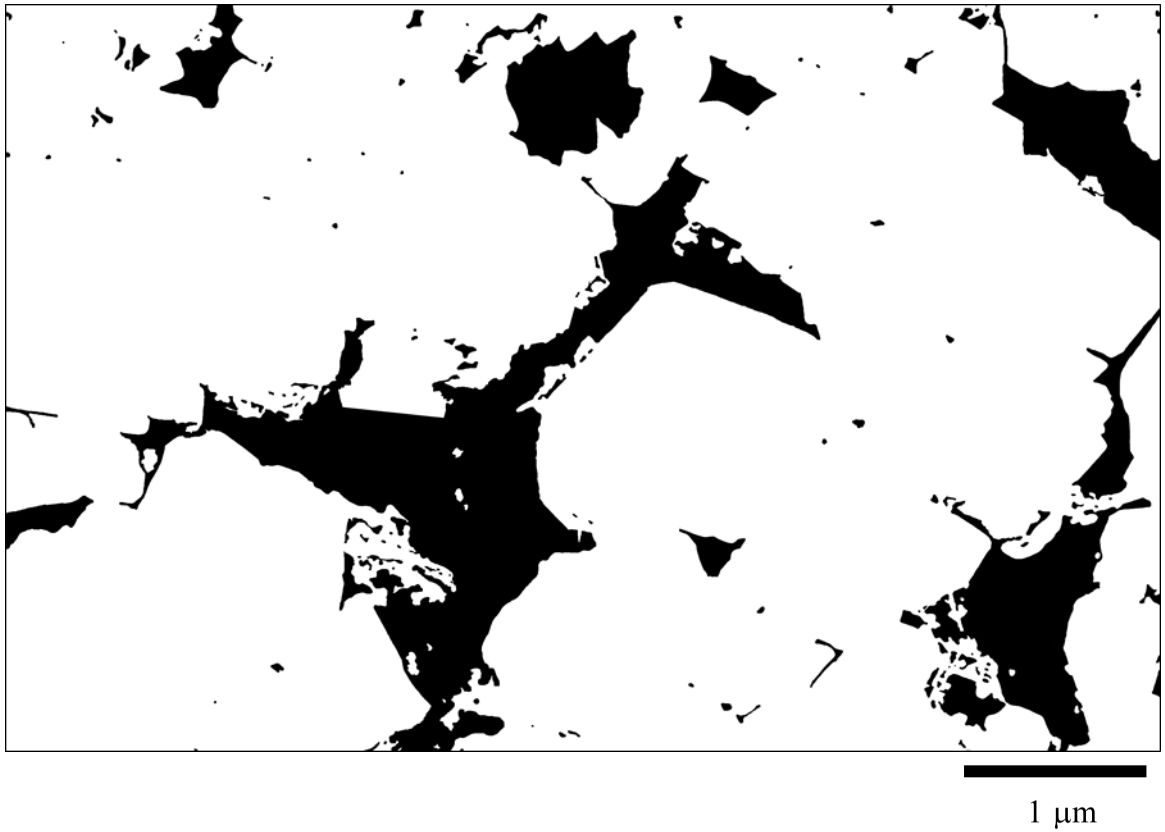

FIGURE 4.38. Thresholded massive matrix of quartz-phase porcelanite

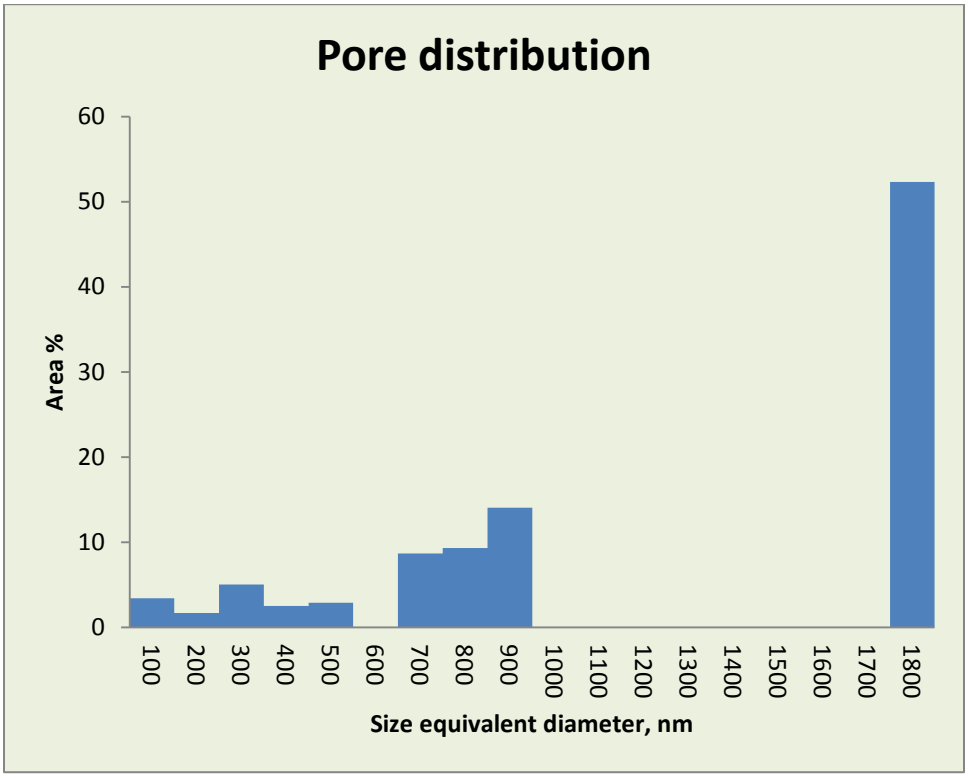

FIGURE 4.39. Pore distribution of the massive matrix of quartz-phase porcelanite (VK12-15).

TABLE 4.9. Porosity, Pore Diameter and Shape Descriptors of Detrital-Poor Quartz Porcelanite of the Massive Matrix (Massive) (VK12-15)

Pores: % Area	Circular equivalent diameter (nm)	Aspect Ratio	Roundness	Circularity	Solidity	Perimeter over area μm^{-1}
16.62	3-1715	2.35	0.43	0.667	0.809	17.01

4.2.3 Detrital-Rich Quartz-Phase Porcelanite

The detrital-rich quartz porcelanite has a heterogeneous microporosity (Figure 4.40). The pores have irregular shapes with anhedral crystals forming the pore walls. The pores are nanopore to micropore in size. Some large pores are connected but are largely surrounded and isolated by impermeable quartz matrix. The rectangle-bounded area (Figure 4.40) is analysed (Figures 4.41 & 42) resulting in moderate porosity and poor connectivity.

The microporosity of the detrital-rich quartz porcelanite varies (Figures 4.41 & 42). The pores have irregular shapes with anhedral crystals in some of the very large pores. The pores are 50 nanometers to 2.25 micrometers in effective circular diameter (Figures 4.41, 42 & 43 and Table 4.10).

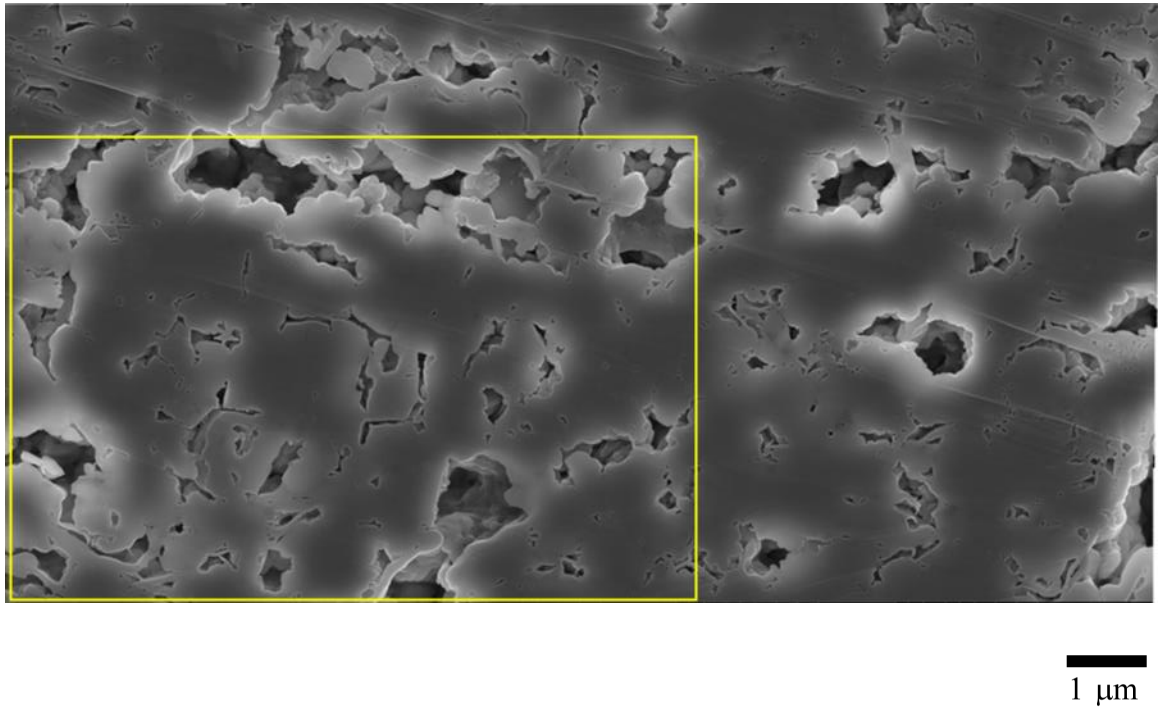

FIGURE 4.40. Secondary electron image of the detrital-rich quartz-phase porcelanite.

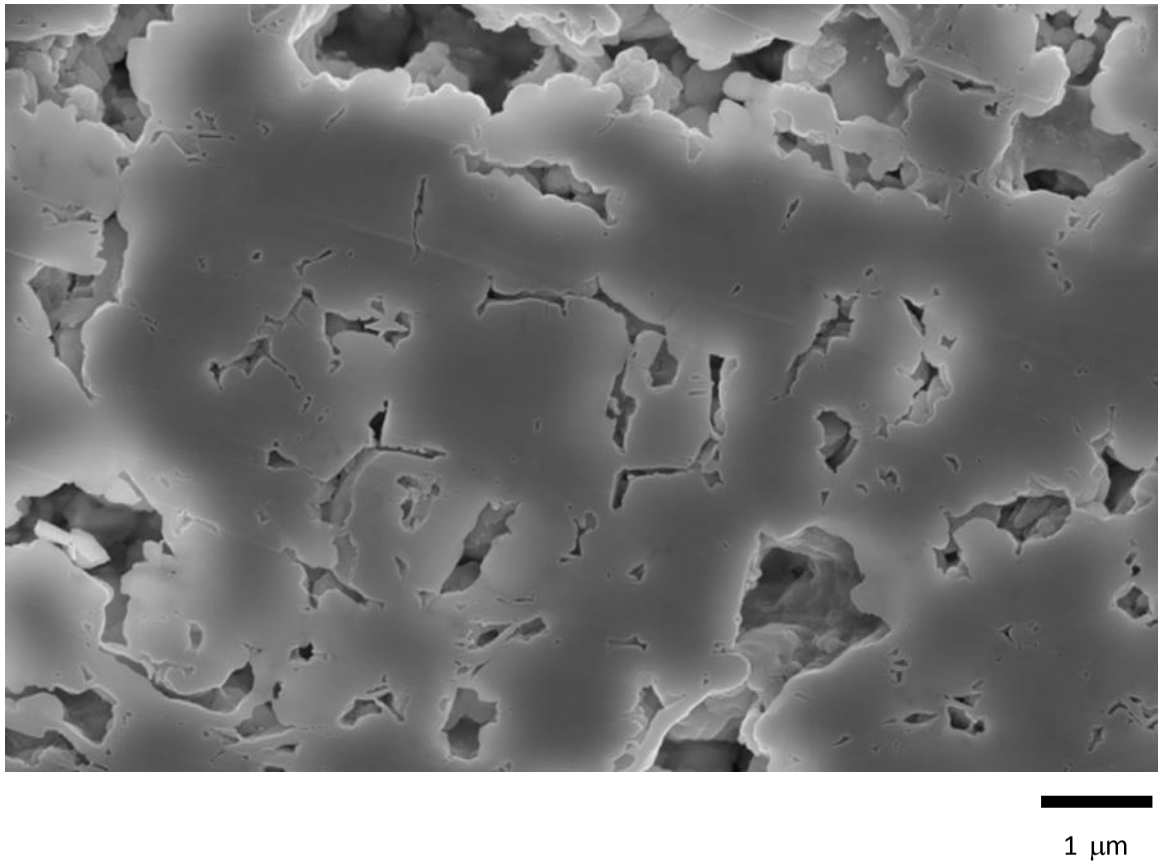

FIGURE 4.41. Secondary electron image of the analyzed detrital-rich quartz-phase porcelanite

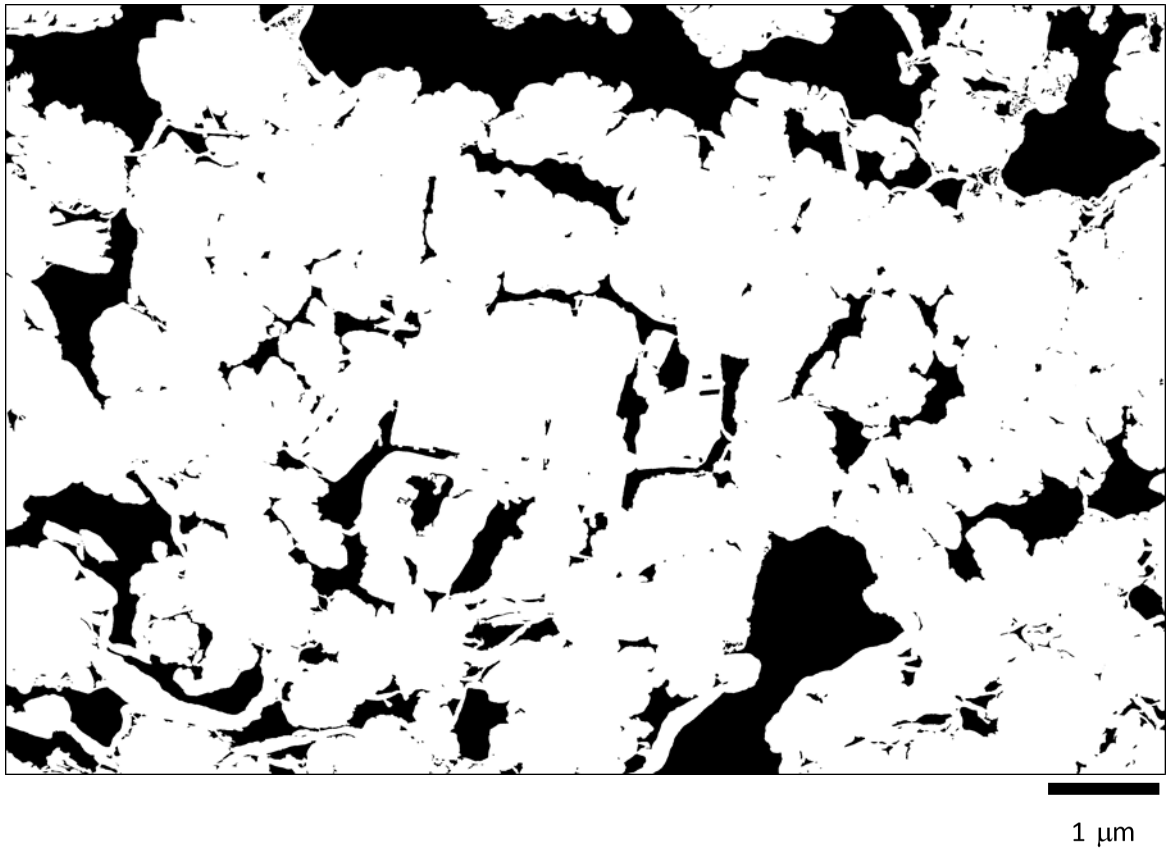

F FIGURE 4.42. Thresholded detrital-rich quartz-phase porcelanite porcelanite

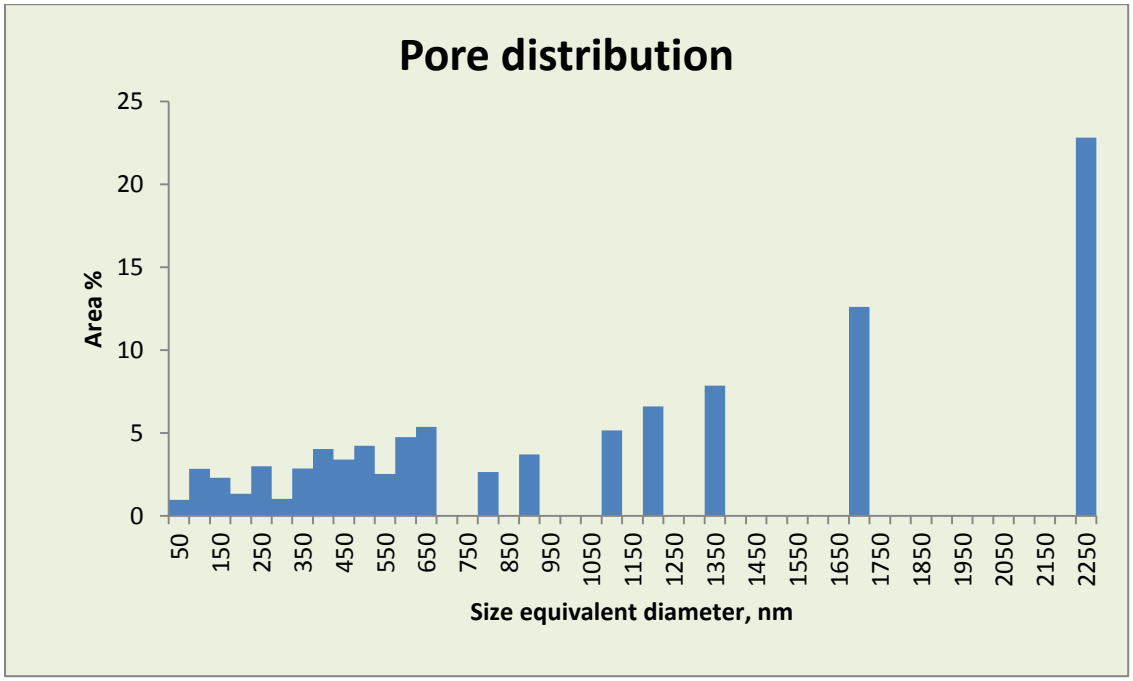

FIGURE 4.43 . Pore distribution of the detrital-rich of quartz-phase porcelanite of sample VB11-43.

TABLE 4.10. Porosity, pore diameter and shape descriptors of detrital-rich quartz porcelanite (VB11-43)

Sample No.	Pores: % Area	Circular equivalent diameter (nm)	Aspect Ratio	Roundness	Circularity	Solidity	Size equivalent diameter (nm)
	21.88	50-2250	2.37	0.42	0.566	0.756	16.64

CHAPTER 5

DISCUSSION

Although numerous previous studies have determined the spatial and burial-depth patterns of bulk-rock porosity and permeability in common siliceous sedimentary rocks (e.g., Isaacs; 1981), Chaika and Dvorkin, 2000; Chaika and Williams; 2001; Schwalbach et al.; 2009 – see Background chapter for more), this thesis presents the first quantitative petrographic analysis of the 2-dimensional pore shape, pore size and porosity microfabric of porcelanites. The quantitative pore shape and size data presented herein provides critical information to test and interpret the previous results that were obtained by bulk analytical methods. High-resolution scanning electron microscopy of argon ion milled surfaces permitted acquisition of undistorted images of submicron-scale (nanoscale) pore features suitable for quantitative shape analysis. We used these techniques to quantify nano- and micropore systems in porcelanites of different composition and silica phase, as well as having different burial-diagenetic histories.

In the following section, quantitative descriptors of pore shape for each analyzed rock type are calculated from the raw shape data to assess the role of pore shape, as well as size, on the bulk properties of the different rocks. These primary and derived parameters are then compared and evaluated for their possible relation to differences in permeability and effective/ineffective porosity found in previous studies.

5.1. Pore Types

In this study of both opal-CT and quartz phase porcelanites with varied detrital composition, several distinct porosity microfabrics are recognized that have different pore shape, size and spatial distributions (Figure 5.1.). The analyzed opal-CT porcelanites are of three types: "normal" detrital-poor and detrital-rich porcelanites and one unusual detrital-poor specimen from the opal-CT to quartz transition zone. Similarly, the quartz-phase porcelanite specimens include two types of detrital-poor porcelanite (laminated and massive) as well as one detrital-rich porcelanite.

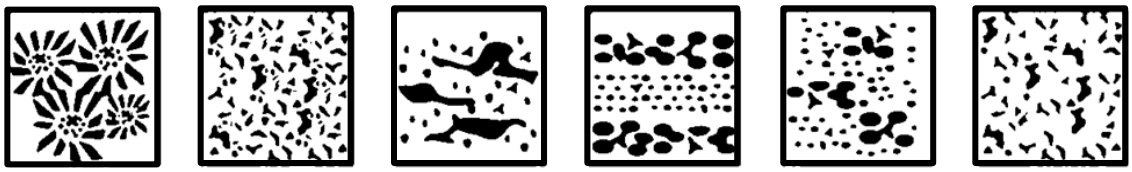

Opal-CT Detrital-poor | Opal-CT Detrital-rich | Opal-CT Detrital-poor Transition-zone | Quartz Detrital-poor | Quartz Detrital-poor | Quartz Detrital-rich

FIGURE 5.1. Sketch of the microfabrics according to silica phase and silica:detritus (detrital and detrital poor).

Quantitative image analysis was carried out using ImageJ softwares. Area, %area, perimeter, as well as shape descriptors such as circularity, roundness, aspect ratio and roundness were computed using mathematical routines and algorithms described:

1. Circularity: $4\pi*[\text{area}/\text{perimeter}^2]$

Value range is from 0 to 1 is a measurement of both the particle form and roughness.

As the shape becomes more round and smooth, the value approaches 1, indicating a circle; the value decreases for more irregular shapes.

2. Aspect ratio: Major axis /minor axis

Derived from a fitted ellipse.

Gives an indication for the elongation of the pore shapes.

3. Roundness: 4 x [area/ π x major axis^2] or related to the inverse of aspect ratio.

4. Solidity: Area/convex hull area (Figure 5.2)

Solidity, S, is the measurement of the overall concavity of a particle derived from fitted ellipse.

Decreases its value as a shape becomes rougher or less solid.

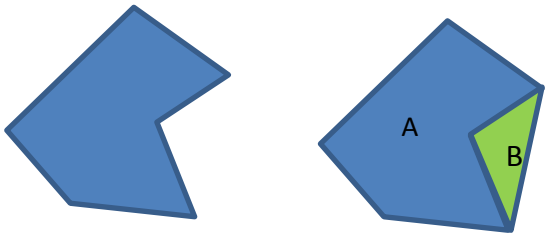

FIGURE 5.2 Definition of the convex hull area A+B for the projection area A of a particle.

5.2. Opal-CT Phase Porcelanite

5.2.1. Detrital-poor Lepispheric Porcelanite

As noted by many by previous workers (see review in Hesse and Schalcht, 2011), opal-CT in detrital-poor siliceous rocks can form lepispheres (i.e., spheres of twinned and

cross-cutting bladed crystals). Previous characterizations were based on SEM images of the outer bladed surface texture of lepispheres in broken rocks. However, this study using cross-cutting ion-milled surfaces shows that the lepispheres do not entirely consist of bladed crystals, but instead display a concentric microstructure consisting of three distinct layers – interlepisphere, mantle and the core of the lepisphere (Figures 4.4-7.). Pores in these highly siliceous rocks are almost entirely intercrystalline with equant to bladed shapes reflecting the angular intersection of opal-CT crystal faces. The interlepisphere region consists of larger, bladed crystals that radiate outward from the mantle region. The interlepisphere pores are 10-440 nm nanopores that have good connectivity and a zonal porosity of 25.19 %. Generally, these interlepisphere pores are elongated and rectangular, reflecting the bladed crystals shape and are larger than pores in the inner mantle and core regions (Figure 4.8. & Table 5.1.).

TABLE 5.1. Shape Descriptors of Pores in the Interlepispheric Zone, Detrital-Poor Porcelanite

Aspect Ratio	Roundness	Circularity	Solidity	Perimeter over area μm^{-1}
2.28	0.44	0.684	0.867	41.71

The highly porous core is composed of granular, anhedral crystallites of opal-CT with well connected nanopores (Figure 4.10.) ranging from 3-280 nm in diameter, with a zonal porosity of 34.3 % (Figures 4.11. & Table 5.2.). The virtually impermeable mantle of opal-CT surrounding the core is composed of a massive groundmass that isolates the core and renders its porosity largely isolated and ineffective.

TABLE 5.2. Shape Descriptors of Pores in the Lepispheric Core, Detrital-Poor Porcelanite.

Aspect Ratio	Roundness	Circularity	Solidity	Perimeter over area μm^{-1}
1.90	0.53	0.702	0.844	107.30

According to the shape descriptors, the interlepisphere pores are more elongated, smooth and concave than the core pores, with aspect ratio of 2.28 vs. 1.90, circularity of 0.702 vs. 0.684 and solidity 0.867 vs. 0.844, respectively. Futhermore, the perimeter over area of 41.71 to 107.30 μm^{-1} respectively show that the effective width of the interlepisphere pores are larger than the core pores. The cores of each lepisphere are virtually isolated by the impermeable mantle, whereas the interlepisphere are better interconnected. The isolation of the cores lessens the effective porosity of the whole rock even though the core porosity would be detected and included in total porosity by indirect means such as a neutron porosity or gamma-ray density logging tool.

5.2.2. Detrital-rich opal-CT porcelanite

The detrital-rich opal-CT specimen that was studied is a rather homogeneous porcelanite, but others may show greater textural variability. It has a relatively low porosity of 18.82% that is comprised of small pores ranging from 3-180 nm with poor apparent connectivity (Figures 4.12&13.). The shapes of the pores are irregular with some large elongated ones (Figure 4.12, and Table 5.3). The mean size of the pores is smaller than the lepispheric core of the detrital-poor opal-CT porcelanite although they have very similar aspect ratios of 1.96 vs. 1.90, respectively (Table 5.3.). The perimeter

over area of this detrital-rich opal-CT is 124.28 vs. 107.30 μm^{-1} to the core of the detrital-poor porcelanite (Table 5.2 & 5.3). According to the shape descriptors, the pores in the detrital-rich sample are less smooth than the pores of the detrital-poor lepispheric core, but have similar concavity as shown by circularity of 0.702 vs. 0.684 and solidity of 0.828 vs. 0.844. The interlepispheric pores of the detrital-poor porcelanite are longer, wider, and less ragged than the pores of the detrital-rich opal-CT porcelanite. Overall, the width, circularity, smoothness, relative good interconnection are lower in the detrital-rich porcelanite than in any part of the lepispheric opal-CT porcelanite. In conclusion, the small size (mean equivalent diameter of 100 nm) and their poor connectivity of the detrital-rich porcelanite results in poorly connected, ineffective porosity that would render poor permeability of the rock as compared to the detrital-poor rocks.

TABLE 5.3. Shape Descriptors of Pores in Detrital-Rich, Opal-CT Porcelanite

Aspect Ratio	Roundness	Circularity	Solidity	Perimeter over area μm^{-1}
1.96	0.51	0.729	0.828	124.58

5.2.3. Detrital-poor opal-CT porcelanite (Transition-zone)

Although, diagenetic changes in silica phase, lithology, and porosity are generally regarded as a result of continuous increases in temperature and overburden, the cessation of burial or tectonic reversal can result in localized loss or gain of porosity in highly siliceous sediments (Behl and Garrison, 1994; Behl et al., 2012). Many successions –

especially those exposed at the surface or warped into anticlinal structures - experience pauses in burial or are tectonically uplifted.

Opal-CT porcelanites that are spatially associated with quartz-phase cherts in a paused or uplifted transition zone may have extremely high porosity (50-65%) for opal-CT phase rocks – as high as common in pure diatomites (R. Behl, Pers. Comm., 2016). "Transition-zone" opal-CT porcelanites have large 1-10 micrometer-scale, interconnected dissolution vuggy pores (Figure 4.14.). The pore surfaces are not bounded by euhedral or subhedral crystal faces. These kinds of rocks are closely spatially associated on the bed- and lamination-scale with the presence of "late quartz chert" that are silicified at cessation of burial or during tectonic uplift (Behl and Garrison, 1994; Behl et al., 2012). They also have very high permeability compared to other "normal" porcelanites, reaching 7-9 millidarcies (R. Behl, Pers. Comm., 2016).

5.3. Quartz-Phase Porcelanites

The three types of quartz-phase porcelanites that were analyzed display distinct pore system microfabrics and properties. They are: 1. detrital-poor laminated quartz porcelanite; 2. detrital-poor massive quartz porcelanite; 3. detrital-rich quartz porcelanite.

5.3.1. Detrital-Poor Quartz Porcelanite (Laminated)

Microscopically, the rock is heterogeneous with marked difference in porosity, pore shape and pore connectivity. The high- and low-porosity lamination zones are discussed separately below.

5.3.1.1. Detrital-poor quartz porcelanite (high-porosity lamination zones) with extremely large pores of high interconnection.

Highly porous zones (laminations) consist of very highly connected large (> 1 micron) pores with irregular shapes. They have

almost micrometer-scale pore-throat diameters (Figures 4.17. and 4.18.). Some pore surfaces display subhedral to euhedral crystal habits, whereas others are irregular or anhedral (Figures 4.17. and 4.18.). For this highly porous specimen, the pore size ranges from 0.4-3.0 micrometer (Figures 4.19 and 4.20., Table 5.4.). According to the shape descriptors, the pores are moderately circular and smooth as well as moderately concave with circularity of 0.672 and solidity 0.793 respectively (Figure 4.17. & 4.18.). Additionally, the large average size, relatively smaller aspect ratio of 2.03 and smaller perimeter over area of 6.13 μm^{-1} indicate smooth, wide pores that, along with the good connectivity, would positively affect permeability.

TABLE 5.4. Shape Descriptors of Detrital-Poor, Quartz Porcelanite (Laminated), with Extremely Large Pores of High Interconnection

Aspect Ratio	Roundness	Circularity	Solidity	Perimeter over area μm^{-1}
2.03	0.49	0.672	0.793	6.13

5.3.1.2. Detrital-poor quartz porcelanite (low-porosity lamination zones). The low-porosity laminations are spatially heterogeneous with zones of different pore-sizes and shapes (Figures 4.21). The poor apparent connectivity of this zone results in isolation of many pores. Areas with smaller pores have circular equivalent diameters that vary from 3-600 nm with low zonal porosity of 8.89 % and irregular shapes (Figures 4.22&23, and Table 5.5). The area with relatively larger pores has circular equivalent diameters that range from 17 nm to 2.254 micrometers and a zonal porosity of 24.82 % (Figures

4.24-26, and Table 5.6). Surrounding the large pores is nearly solid matrix with only dispersed and isolated smaller pores. (Figures 4.24 and 4.25). In general, circularity, smoothness and concavity are similar to that of the highly porous laminated zones described in section 5.2.1.1. However, the width of the low–porosity laminated zone pores and pore-throat diameter are smaller relative to the extremely highly porous laminated ones as they have similar aspect ratio (2.31 & 2.17), versus 2.03 for the highly porous lamination zones), but relatively larger perimeter/area (26.89 & 12.18, versus 6.13 for the highly porous lamination zones) plus larger average size of the highly porous lamination zones pores (Table 5.4-5.6).

TABLE 5.5. Shape Descriptors of Detrital-Poor, Quartz Porcelanite (Low-Porosity Lamination Zone), with Relatively Smaller Pores.

Aspect Ratio	Roundness	Circularity	Solidity	Perimeter over area μm^{-1}
2.31	0.43	0.647	0.818	26.89

TABLE 5.6. Shape Descriptors of Detrital-Poor, Quartz Porcelanite (High-Porosity Lamination Zone), with Relatively Larger Pores.

Aspect Ratio	Roundness	Circularity	Solidity	Perimeter over area μm^{-1}
2.17	0.46	0.696	0.858	12.18

Overall, the laminated detrital-poor quartz porcelanite is very good in terms of porosity, pore size & shape and interconnection, even though the high-connectivity is

primarily along the more porous laminations. The rock is highly porous with well interconnected, large, moderately smooth pores with large pore-throats, which would provide good effective permeability.

5.3.2 Detrital-Poor Quartz Porcelanites (Massive)

The macroscopically massive porcelanite beds with low detrital content frequently show patchy to indistinctly laminated fabric of detrital grains under SEM (Figures 4.27-4.29), giving rise to two distinct zones: 1. relatively pure quartz with only minor authigenic clays and 2. detrital-rich quartz porcelanite. This condition gives them a heterogeneous and discontinuous composition, microstructure and porosity. The massive matrix contains disconnected nano- to micropores having some authigenic clays within the angular, intercrystalline pores (Figures 4.36 and 4.37). The pores in the massive detrital-poor intervals tend to have sharp edges following the euhedral quartz crystal shapes (Figure 4.36.). The pores associated with the patchy to indistinct laminations of detritus are more irregular shapes and contain primary and authigenic clays.

Pores within the massive quartz porcelanite have circular equivalent diameter of 3-1715 nm with a low porosity of 16.62 % and irregular shapes. The nano- to micro-pores are only partially connected and are surrounded by a non-porous impermeable quartz (Figure 4.37). In contrast, the detrital-rich areas (patchy to indistinctly laminated areas) have 14.45 % porosity with pores of circular equivalent diameter of 5-758 nm that are partially connected (Figure 4.31). Pores within the detrital-rich zones relative to the massive part are less elongated, less circular, more ragged and thin (small-sized pore-width) as indicated by the aspect ratio, related to circularity, and perimeter over area (Tables 5.7 and 5.8.). Although, some of the pores are large size and connected, they are

mostly surrounded by matrix with only disseminated small size pores. Altogether, these factors would results in poor effective porosity. As indicated by circularity, perimeter over area, aspect ratio, etc., the massive zone with minor authigenic clays, has larger and smoother pores. However, the pores are poorly connected, rendering porosity ineffective and likely with poor permeability.

TABLE 5.7. Shape Descriptors of Detrital-Poor, Quartz Porcelanite (Massive)

Aspect Ratio	Roundness	Circularity	Solidity	Perimeter over area μm^{-1}
2.35	0.43	0.667	0.809	17.01

TABLE 5.8. Shape descriptors of Detrital-Poor, Quartz Porcelanite (Patchy or Lenticular Areas)

Aspect Ratio	Roundness	Circularity	Solidity	Perimeter over area μm^{-1}
1.96	0.51	0.603	0.775	66.68

5.3.3. Detrital-rich quartz-phase porcelanite

The microporosity of the detrital-rich quartz porcelanite is heterogeneous (Figure 4.40). The pores are of irregular shapes with anhedral crystals forming the pore walls. The pores are 50 nanometers to 2.25 micrometers in equivalent circular diameter (nanopore to micropore in size) and it has 21.88 % porosity (Figures 4.41-43) Pores are elongated with aspect ratio of 2.37 (Table 5.9.). Some large, ragged pores are connected

but are largely surrounded by impermeable quartz matrix layers (Figures 4.40-41.) likely resulting in ineffective porosity and low permeability.

TAbLE 5.9. Shape Descriptors of Detrital-Rich, Quartz Porcelanite

Aspect Ratio	Roundness	Circularity	Solidity	Perimeter over area
2.37	0.42	0.566	0.756	16.64

5.4 Synthesis

This study has provided new information and insight into the evolution of pore structure of siliceous sedimentary rocks with diagenesis that help understand differences in the reservoir performance of opal-CT and quartz-phase porcelanites. According to previous work, the porosity reduction is controlled largely by composition and silica-diagenesis (Isaacs, 1981; Chaika C. and Dvorkin (2000); Chaika C. and Williams 2001and Schwalbach et al. 2009). According to Isaacs, porosity in carbonate-free rocks decreases from 55-70% in diatomaceous rocks to 25-40% in opal-CT to 10-20% for quartz-phase rocks with low-detritus siliceous rocks generally having higher porosities and lower bulk densities than detrital-rich siliceous rocks (Figure 5.3). These changes in porosity are associated with large changes in permeability and hydrocarbon saturation (Table 5.10). Chaika and Dvorkin (2001) and Schwalbach et al., (2009) quantified quartz porosity 12-26% and 15-30%, respectively (Table 5.11).

Porcelanites are important reservoir rocks in California that demonstrate great differences in producibility despite similar bulk physical characteristics. Schwalbach et

al. (2009) observed that quartz-phase porcelanites have an order-of-magnitude higher permeability than opal-CT porcelanites in spite having lower porosities (Table 5.10). Based on mercury injection capillary pressure measurements, they suggested that the indication of higher permeability in quartz porcelanites could be due to pore-throat size with the pore-throat size range from 0.01-0.10 for opal-CT and 0.1-1.0 μm for quartz-phase porcelanite (Table 5.10.). According to these workers, the increase of pore-throat diameter substantially enhances capillary properties of the rock resulting in much higher hydrocarbon saturation for quartz-phase rocks than opal-CT.

The paradox of lower porosity, but higher permeability in quartz-phase porcelanites is the main reason for undertaking this microfabric study as it could be due to pore size, shape or degree of interconnectivity. Understanding this complex difference between opal-CT and quartz-phase porcelanites is a major bottleneck to potentially unlocking additional large oil potential and lower permeability in previously unreached reservoir rocks. Schwalbach et al. (2009) realized that strata are thinly bedded and extremely heterogeneous therefore making it difficult to sufficiently characterize the rocks using standard subsurface bulk analysis techniques.

This study addressed this issue using highly advanced petrographic sample preparation and analysis techniques applied over the nanometer to millimeter scale instead of bulk whole-rock analysis. We identified and quantified significant differences in pore size, shape and complexity between opal-CT and quartz-phase porcelanites, but also between rocks of the same silica phase with distinctly lenticular or laminated sedimentary fabric. The pore shapes and pore fabrics likely have important influence on permeability differences in these rocks, as discussed below.

The permeability of the detrital-poor, lepispheric opal-CT porosity with high porosity is likely affected by size, shape and form identified in this study. Although the rock porosity is within the range of previous studies (Isaacs, 1981; Chaika C. and Dvorkin (2000); Schwalbach et al., (2009), the micro-structure displays a previously unknown heterogeneity with interlepisphere zones likely having good effective porosity and relatively good permeability with smooth and moderately wide and concave pores, whereas the core's porosity is isolated from the rest of the rock although it would have relatively good local interconnection (permeability) within the isolated zone. Because of this areal separation, the whole-rock permeability would be minimized due to the ineffective porosity of the isolated core-pores by the virtually impermeable mantle. The effective porosity and apparent permeability of detrital-rich opal-CT porcelanites would be poor due to the small pore sizes and poor connectivity of pores in the rock. The transition zone opal-CT porcelanite rocks with extremely high porosity and large and highly connected vuggy pores has excellent effective porosity and high permeability.

The detrital-poor, laminated quartz porcelanite consists of two zones – one with extremely high porosity and the other with low porosity; both of them have moderately smooth and concave pore-shapes. The extremely high porosity laminations consisting of highly connected, moderately smooth, very large pores and pore-throats would produce high bedding-parallel permeability and moderately high effective porosity. This coincides with the observations of quartz-phase porcelanites by Schwalbach et al., (2009).

In comparison, the total porosity of detrital-poor opal-CT porcelanite is high relative to detrital-poor quartz porcelanite. However, the laminated quartz porcelanite has

a much better effective porosity and potential for permeability than the opal-CT porcelanite due to the size, and connectivity of the lepispheric opal-CT porcelanite.

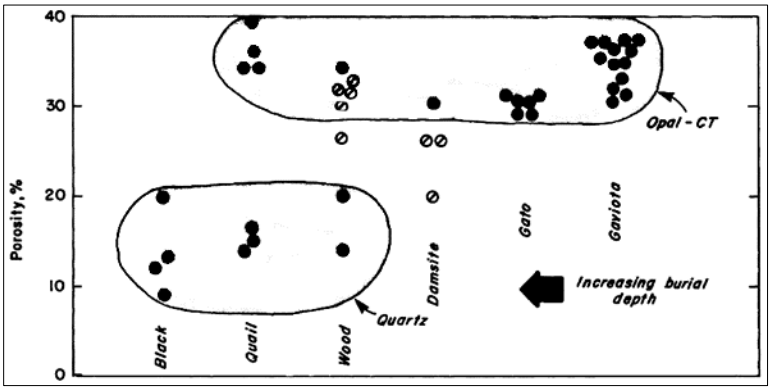

FIGURE 5.3. Porosity reduction in siliceous rocks (> 50 % silica) from upper member of Monterey along the Santa Barbara coast with transition from opal-CT to quartz with greater burial to west towards Black Canyon. Θ = samples with both opal-CT and diagenetic quartz.

TABLE 5.10. Porosity Parameters of Opal-CT and Quartz Porcelanites. Schwalbach et al., (2009).

	Typical Porosity (%)	Grain Density (g/cc)	Permeability (air, md)	Pore-throat Diameter (microns)	Oil Saturation (%)
Opal-CT	25-40	2.25-2.35	0.01-0.1's	0.01-0.1	0-30
Quartz	15-30	2.55-2.65	0. 1-1.0's	0. 1-1.0	30-60

The results presented herein are within the range of previous studies with opal-CT phase porcelanites having 18-35% porosity and quartz-phase porcelanites having 9-29 % though the data is limited to few samples and very small areas of analysis within those samples (Table 5.11). In addition, we find that porosities of porcelanites have positive

correlation with biogenic/diagenetic silica content, confirming the previous studies (Table 5.12). However, this study is the first to document the unique and heterogeneous distribution of pores and pore types in porcelanites of different silica phase and detrital composition, and provide insight into how and why permeability may significantly vary within this one general rock type.

TABLE 5.11. Typical Reservoir Parameters of opal-CT and Quartz Porcelanites. Isaacs (1981); Chaika C. and Dvorkin (2000); and Schwalbach et al. (2009)

	Opal-CT Porosity (%)	Quartz Porosity (%)
Isaacs	25-40	9-22
Chaika and Dvorkin	<43	12-26
Schwalbach	25-40	15-30
This study	18-35	9-29

TABLE 5.12. The Positive Correlation of Porosities of Porcelanites with Biogenic/Diagenetic Silica Content of Porcelanites

	Detrital-poor Lepispheric Opal-CT	Detrital-rich Opal-CT	Detrital-poor Opal-CT (Transition-zone)	Detrital-poor Quartz (Laminated)	Detrital-poor Quartz (Massive)	Detrital-Rich Quartz
Silica-content	>75 %	<65%	>75%	>80%	>80%	<65%
Porosity (%)	26-34	19	>55	9-29	14-17	22

Table 5.13 presents the differences in silica content, pore shape and size of the analyzed samples and organizes them according to their apparent effective porosity and permeability. Although previous publications have found an order-of-magnitude larger

TABLE 5.13. Summary Table of Specimen Silica Content, Pore Size and Pore-Shape Descriptors.

	Silica content	Pores: % Area	Circular equivalent diameter (nm)	Aspect ratio	Roundness	Circularity	Solidity	Perimeter over area μm^{-1}
Effective Porosity								
Opal-CT								
Detrital-poor Interlepisphere	>75 %	25.19	10-440	2.28	0.44	0.684	0.867	41.71
Detrital-poor transition-zone	>75 %	55	1000's	-	-	-	-	-
Quartz								
Detrital-poor laminated-highly porous laminations	>80 %	28.50	400-3000	2.03	0.49	0.672	0.793	6.13
Ineffective Porosity								
Opal-CT								
Detrital-rich opal-CT	<65%	18.82	3-180	1.96	0.51	0.729	0.828	124.58
Quartz								
Detrital-poor massive quartz	>80 %	16.62	3-1715	2.35	0.43	0.667	0.809	17.01
Detrital-rich quartz	<65%	21.88	50-2250	2.37	0.42	0.566	0.756	16.64

permeability in some quartz-phase porcelanites than in opal-CT porcelanites in spite of decreased total porosity, we wished to test if pore size and shape (roughness) also differed between the rocks of the different phases and may contribute to the differences in reservoir behavior. This study finds a significant difference between opal-CT and quartz phase rocks in their pore size (<few 100 nm vs. up to a few 1000 nm), but no important differences in pore shape descriptors (aspect ratio, roundness, circularity, solidity or perimeter over area) based on silica phases alone. Overall, determined ranges of shape descriptors overlap and have no significant differences between phases, indicating that variation in pore roughness or smoothness is not an important factor. Instead, we find the

greatest potential control of permeability and effective porosity to be the spatial microfabric of the rock, secondarily modified by pore size. The detrital-rich opal-CT, massive detrital-poor quartz and detrital-rich quartz porcelanites have ineffective porosity due mainly to the poor interconnectivity of their distributed pores, and consequently low permeability and storage capacity. On the other hand, the detrital-poor opal-CT interlepispheric zone, detrital-poor opal-CT transition-zone porcelanite and the detrital-poor laminated quartz porcelanite have well-connected pore systems providing good effective porosity and better permeability.

Even within this better group, there are differences in pore structure between even the porcelanites with good effective porosity that would affect permeability. Although pores in the extremely porous zone of the laminated detrital-poor quartz and the interlepispheric zone of the detrital-poor opal-CT porcelanite have very similar shape descriptors (Table 5.13.), the laminated detrital-poor quartz porcelanite would have better permeability because of its larger pores (400-3000 nm to 10-440 nm), wider pore-throats (up to 1 microns see Figures 4.17 and 4.18) and more continuous lateral connectivity. Therefore, the laminated detrital-poor quartz porcelanite would have higher permeability in quartz porcelanites versus the detrital-poor interlepisphere is due to pore-size and pore-throat diameter, though the pore-throat is observed from the images rather than quantification. Furthermore, the transition zone has high permeability even though it has ragged surface due to its extremely large and well-connected pores and large pore-throats. Although the massive detrital-poor quartz have large size and similar circularity (Table 5.13) to the extremely porous zone of the laminated detrital-poor quartz, their low interconnectivity makes them poor in effective porosity and permeability. As to the

detrital-rich opal-CT and detrital-rich quartz porcelanites, there is a difference of pore-size (Table 5.13) but their poor permeability is mainly due to their interconnectivity.

CHAPTER 6

CONCLUSIONS

This study demonstrated that the argon ion milling method for sample preparation is optimal and appropriate for analysis of sub-micron pores in porcelanite samples. This method provides highly polished surfaces with large (mm-scale area) representative x-section free from curtain effect, artifacts and distortion that can be imaged at high resolution by SEM. With the polishing and imaging methods employed, a quantitative petrographic microfabric analysis of 2-dimensional pore shape with sub-micron pore-size and structures of different siliceous rocks is presented and quantified.

Although limited to a few samples that may not be representative of the broad range of compositions, we measured opal-CT phase porcelanites having 18-35% porosity and quartz-phase porcelanites having 9-29% These findings, using imaging methods at the micrometer-scale, obtained porosity values for opal-CT and quartz-phase porcelanites of various compositions that are consistent with previous studies using traditional methods of bulk, whole-rock measurement (Isaacs, 1981; Chaika and Dvorkin, 2000; Chaika and Williams, 2001; Schwalbach et al., 2009). This study also confirms the positive correlation of porosity with biogenic/diagenetic silica content that has been previously reports by the workers cited above.

Opal-CT porcelanite displays three different microfabrics: two in detrital-poor (>75%) and one in detrital-rich (<60%) porcelanite:

The detrital-poor opal-CT porcelanite sample has high bulk porosity of 48.7% according to the conventional core porosity analysis. We find that it has a lepispheric structure and the distribution of pores and their size, shape and form are controlled by the lepispheric fabric. Lepispheric cores and interlepisphere zones each comprise ~1/2 of the total porosity The larger interlepisphere pores are formed by larger, crosscutting and radiating equant to bladed crystals, and themselves are tabular and smooth, and interconnected with other pores of adjacent lepispheric rims and have equivalent diameters of 3-440 nm. Pores in the lepispheric cores are virtually isolated by the impermeable mantle. Therefore, the interlepispheric zone has good effective porosity and possibly relatively good permeability, but the whole-rock permeability is minimized due to the virtual ineffective porosity of the core pores.

The detrital-rich opal-CT specimen contains lower porosity than the detrital-poor samples, but that consists of small, irregular pores with narrow width and poor apparent connectivity pores. The isolation of pores and their poor connectivity results in poor effective porosity and poor permeability for the rock.

The third opal-CT group, the “Transition-zone” opal-CT porcelanites have extremely high porosity (bulk porosity 51.8 %) for opal-CT phase rocks – as high as common in pure diatomites. They have large 1-10 micrometer, well interconnected, dissolution vuggy pores. Their very high porosity and highly connected pores result in good effective porosity and good effective permeability.

In quartz porcelanites, we identified three microfabrics with different micropore systems:

The laminated detrital-poor quartz porcelanite (bulk porosity 35.3%) possesses a heterogeneous micropore system with alternating bands that are highly porous with interconnected, smooth micropores and wide, smooth pore-throats. Although dramatically reduced in total porosity from similar composition, detrital-poor opal-CT samples, larger pore size, connectivity and smoothness can explain the increased permeability indicated by mercury injection capillary pressure tests.

The detrital-poor, macroscopically massive quartz-phase porcelanite has a patchy to indistinctly laminated microfabric that forms a heterogeneous and discontinuous microstructure and porosity. Overall, there is poor connectivity except within isolated, but more porous patches producing poor bulk effective porosity and poor permeability. In general, the pore size, distribution and poor interconnection of the massive porcelanite gives it poorer effective porosity and permeability than the laminated detrital-poor quartz-phase porcelanite.

The detrital-rich quartz porcelanite has a heterogeneous microporosity of nanopores to micropores of irregular shape. Pores are poorly connected with some large, elongated, ragged pores connected but these large pores are largely surrounded by impermeable layers quartz matrix. Overall, this detrital-rich quartz porcelanite would have ineffective, isolated porosity and low permeability

This study finds a significant difference between opal-CT and quartz phase rocks in pore size (<few 100 nm vs. up to a few 1000 nm), but no overall important differences in pore shape descriptors (aspect ratio, roundness, circularity, solidity or perimeter over area) based on silica phases alone. Instead, we find the greatest additional control of permeability and effective porosity to be the spatial microfabric of the rock. The detrital-

rich opal-CT, massive detrital-poor quartz and detrital-rich quartz porcelanites have ineffective porosity due mainly to the poor interconnectivity of their unevenly distributed pores. On the other hand, the detrital-poor opal-CT interlepispheric zone, detrital-poor opal-CT transition-zone porcelanite and the detrital-poor laminated quartz porcelanite have well-connected pore systems providing good effective porosity and better permeability.

In conclusion, the results of this study show an important difference between opal-CT and quartz phase rocks in their pore size (<few 100 nm vs. up to a few 1000 nm). However, the differences in pore shape descriptors (aspect ratio, roundness, circularity, solidity or perimeter over area) are insignificant based on silica phases alone. Generally, the determined ranges of shape descriptors overlap and they don't show significance differences between phases, showing that difference in pore roughness or smoothness is not an important factor. Instead, we demonastrated that the greatest potential control of permeability and effective porosity to be the spatial microfabric of the rock, which is secondarily modified by pore size. The detrital-rich opal-CT, massive detrital-poor quartz and detrital-rich quartz porcelanites have ineffective porosity due chiefly to the poor interconnectivity of their d pores distribution, and resulting in low permeability and storage capacity. On the other hand, the detrital-poor opal-CT interlepispheric zone, detrital-poor opal-CT transition-zone porcelanite and the detrital-poor laminated quartz porcelanite with its well-connected pore systems provides good effective porosity and better permeability.

Furthermore, even within this good effective porosity group, there is variation in pore structure between the porcelanites that would ultimately affect permeability.

Although pores in the extremely porous zone of the laminated detrital-poor quartz and the interlepispheric zone of the detrital-poor opal-CT porcelanite having very similar shape descriptors the permeability of the laminated detrital-poor quartz porcelanite would have better because of its extremely larger pores, wider pore-throats and the continuity of lateral (along-lamination) connectivity. In addition, even though the pores of the transition-zone opal-CT porcelanite have ragged surfaces it has high measured permeability due to its extremely large and well-connected pores and large pore-throats. The patchy distribution and low interconnectivity would critically decrease the effective porosity and permeability of the massive quartz rock though the pores of these rocks are as large and circular as those in the extremely porous zone of the laminated detrital-poor quartz. Irrespective of their variation in pore-size, both opal-CT and quartz-phase detrital-rich porcelanites would have poor permeability due to the absence of pore-interconnectivity.

REFERENCES

REFERENCES

Atwater, T., 1970, Implications of plate tectonics for the Cenozoic tectonic evolution of western North America: Geological Society of America Bulletin, v. 81, p. 3513-3536.

Atwater, T., 1989, Plate tectonic history of the northeast Pacific and western North America: The Geology of North America, The Eastern Pacific Ocean and Hawaii: The Geological Society of America, v. N, p. 21-72.

Atwater, T., and Molnar, P., 1973, Relative motion of the Pacific and North America plates deduced from se-floor spreading in the Atlantic, Indian, and South Pacific Oceans, in Proceedings of the conference on tectonic problems of the San Andreas fault system: Stanford University Publications Geological Sciences., v. 13, p. 136-148.

Atwater, T., and Stock, J., 1998, Pacific-North America plate tectonics of the Neogene southwestern United States: An update, International Geology Review, v. 40, p. 375-402.

Barron, J.A., 1986, Paleoceanographic and tectonic controls on deposition of the Monterey Formation and related siliceous rocks in California: Palaeogeography, Palaeoclimatology, Palaeoecology, v. 53, p.27-45.

Behl, R.J., 1992, Chertification in the Monterey Formation of California and Deep-Sea sediments of the West Pacific [Ph.D. thesis]: Santa Cruz, University of California, 287 p.

Behl, R.J., 1998, Relationships between silica diagenesis, deformation, and fluid flow in Monterey Formation cherts, Santa Maria Basin, California, *in* Eichubl, P., ed., Diagenesis, deformation, and fluid flow in the Miocene Monterey Formation: Pacific Section, SEPM (Society for Sedimentary Geology) Special Publication 83, p. 77-83.

Behl, R.J., 1999, Since Bramlette (1946), the Miocene Monterey Formation of California revisited: Geological Society of America, Special Paper, p. 301-313.

Behl, R.J., and Garrison, R.E., 1994, The origin of chert in the Monterey Formation of California (USA), *in* Iijoma, A., Abed, A., and Garrison, R., eds., Siliceous, phosphatic and glauconitic sediments of the Tertiary and Mesozoic: Utrecht, International Geological Congress Proceedings, Part C: p. 101-132.

Biddle, K.T., 1991, The Los Angeles Basins: An overview, in Biddle, K.T., ed., Active margin basins: Association of Petroleum Geologist Bulletin Memoirs 52, p.1-24.

Blake, M.C., Campbell, R.H., Dibble, JR., T.W., Howell, D.G., Nilsen, T.H., Normark, W.R., Vedder, J.C., and Silver E.A., 1978, Neogene Basin Formation in relation to Plate-Tectonic Evolution of San Andreas Fault System, California: The American Association of Petroleum Geologist Bulletin, v. 62, p. 344-372.

Bramlette, M.N., 1946, The Monterey Formation of California and the origin of its siliceous rocks: U.S. Geological Survey Professional Paper 212, p. 57.

Burst, J.R., 1969, Diagenesis of Gulf Coast Clayey Sediments and its possible Relation to petroleum Migration: American Association of Petroleum Geologist Bulletin, v. 53, p. 73-93.

Canfield, C.R., 1939, Subsurface stratigraphy of Santa Maria Valley oil field and adjacent parts of Santa Maria Valley, California: American Association of Petroleum Geologist Bulletin, v. 23, p.45-81.

Chaika, C.J., and Dvorkin, J., 2000, Porosity reduction during digenesis of diatomaceous rocks: American Association of Petroleum Geologist Bulletin, v. 84, p.1173-1184.

Chaika, C.J., and Williams, A., 2001, L.A., Density and mineralogy variations as a function of porosity of Monterey Formation oil and gas reservoirs in California: American Association of Petroleum Geologist Bulletin, v. 85, no. 1, p. 149-167.

Chalmers, G., Bustin, R.M., and Powers, I., 2009, A pore by any other name would be as small: The importance of meso- and microporosity in shale gas (abs.): American Association of Petroleum Geologists Search and Discovery article 90090, 1p.:www.searchdiscovery.com/abstracts/html/2009/annual/abstracts/chalmers.htm accessed March 14,2001).

Choquette, P.W., and Pray, L.C., 1970, Geologic nomenclature and classification of porosity in sedimentary carbonates: Association of Petroleum Geologists Bulletin, v. 54, p. 207-244.

Creager, J.S., Scholl, D.W., and others, 1973, eds., Initial reports of the Deep Sea Drilling Project: Washington, D.C., U.S. Government Printing Office, v. 19, p. 897-913.

Crouch, Bachman, and associates, 1991, Structure and Stratigraphy of the Monterey Formation and adjacent rocks, central California: A field seminar, Part I: Descriptive text and guidebook, in Lewis, L., Hubbard, P., Heath, E., and Pace, A., Southern Coast Ranges, Annual field trip guidebook 15, Santa Ana, South Coast Geological Society, p. 189-217.

Dibblee, T.W., 1989a, Geologic map of the Point Sal and Guadalupe quadrangles, Santa Barbara County, California, Dibble Geological Foundation map Df-25, scale 1:24,000.

Dibblee, T.W., 1989b, Geologic map of the Casmalia and Orcutt quadrangles, Santa Barbara County, California, Dibble Geological Foundation map Df-24, scale 1:24,000.

Dunkel, C.A., and Piper, K.A., 1997, 1995 National assessment of United States oil and gas resources: Assessment of the Pacific Outer Continental Shelf Region: U.S. Department of the Interior Minerals Management Service.

Eichhubl, P., and Behl, R.J., 1998, Diagenesis, deformation, and fluid flow in the Miocene Formation, in Eichhubl, P., ed., Diagenesis, deformation, and fluid flow in the Miocene Monterey Formation: Pacific Section, SEPM (Society for Sedimentary Geology) Special Publication 83, p. 5-13.

Florke, O.W., Hollmann, R., Von Rad, U., and Rosch, H., 1976, Intergrowth in opal-CT lepispheres: Contributions to mineralogy and petrology, v. 58, p. 235-242.

Gorsline, D.S., and Emery, K.O., 1959, Turbidity current deposits in San Pedro and Santa Monica basins off California: Geological Society of American Bulletin, v. 70, p 279-290.

Hein, J.R. Scholl, D.W. Barron, J.A., Jones, M. G., and Miller, J., 1978, Diagenesis of Late Cenozoic diatomaceous deposits and formation of the bottom simulating reflector in the southern Bering Sea: Sedimentology, v. 25, p 155-181.

Hesse, R., and Schacht U., 2011, Early diagenesis of deep-sea sediments, *in* Heiko Hunke and Thierry Mulder, editors: Developments in Sedimentology, Amsterdam: The Netherlands, v. 63, p. 557-713.

Hoskins, E.G., and Grifiths, S.R., 1971, Hydrocarbon potential of northern and central California offshore, *in* Cram, I.H., ed., Future petroleum provinces of the United States-Their geology and potential: American Association of Petroleum Geologists Memoir 15, v.1, p.212-228

Ingle, J.C., Jr., 1981a, Cenozoic depositional history of the northern continental borderland of southern California and the origin of associated Miocene diatomites, in Isaacs, C.M., ed., Guide to the Monterey formation in the California coastal area, Ventura to San Louis Obispo: Los Angeles, Pacific Section, American Association of Petroleum Geologists Special Publication: 52, p. 1-8.

Ingle, J.C., Jr., 1981b, Origin of Neogene diatomites around the north Pacific rim, in Garisson, R.E., and Douglas, R.G. eds., The Monterey Formation and related siliceous rocks of California: Los Angeles, Pacific Section, Society of Economic Paleontologists and Mineralogist, p. 159-179.

Ijeoma, I.O., 2014, A test of diagenetic ordering in siliceous lithofacies, Monterey Formation, Southwestern Casmalia Hill, Santa Maria Basin, California, M.S. thesis: California State University, Long Beach, 161p.

Isaacs, C.M., 1980, Diagenesis in the Monterey Formation examined laterally along the coast near Santa Barbara, California [Ph.D. thesis]: Stanford, California, Stanford university, 329 p.

Isaacs, C.M., 1981, Porosity reduction during diagenesis of the Monterey Formation, Santa Barbara coastal area, California, *in* Garrison, R.E., and Douglas, R.G., eds., Isaacs, C.M., 1982,The Monterey Formation and related siliceous rocks of California: Los Angeles, Pacific Section, Society of Economic Paleontologists and Mineralogists, p.257-271.

Isaacs, C.M., 1982, Influence of rock composition on kinetics of silica phase changes in the Monterey Formation, Santa Barbara area, California: Geology, v. 10, p. 304-308.

Jobe, T.D., 2014, Non-traditional Techniques for Microporosity Evaluation in a Low-Permeability Carbonate Reservoir offshore Abu Dhabi, U.A.E: Search and Discovery Article # 41270.

Kastner, M., Mertz, K., Hollander, D., and Garrison, R., 1984, The association of dolomite-phosphatic-chert: Causes and possible diagenetic sequences, in Garrison, R.E., Kastner, M., and Zenger, D.H., eds., Dolomites of the Monterey Formation and organic-rich units: Los Angeles, Pacific Section, Society of Economic Paleontologists and Mineralogists, p 75-86.

Keller, G., and Isaacs, C., 1985, An evaluation of temperature scales for silica diagenesis in diatomaceous sequence including a new approach based on the Miocene Monterey Formation, California: Geo-Marine Letters, v. 5, p. 31-35.

Lee, H.J., 1973, Measurements and estimates of engineering and other physical properties, Leg 19, in Creager, J.S., Scholl, D.W., and others, eds., Initial reports of the Deep Sea Drilling Project: Washington, D.C. U.S. Government Printing Office, v. 19, p 701-719.

Loucks, R.G., and Reed, R.M., Ruppel, S.C., and Jarvie, D.M., 2009, Morphology, genesis, and distribution of nanometer-scale pores in siliceous mudstones of the Mississipian Barnett Shale: Journal of Sedimentary Research, v. 79, p. 848-861, doi: 10.2110/jsr.2009.092.

Loucks, R.G., and Reed R.M., Ruppel S.C., and Hammes, 2010, Preliminary classification of matrix pores in mudrocks: Gulf Coast Association of Geological Societies Transactions, v. 60, p. 435-441.

Loucks, R.G., Reed, R.M., Ruppel, S.C., and Hammes, U., 2012, Spectrum of pore types and networks in mudrocks and a descriptive classification for matrix-related mudrocks pores: American Association of Petroleum Geologists Bulletin, v. 96, no. 6, p.1071-1098.

MacKinnon, T.C., 1989, Petroleum geology of the Monterey Formation in the Santa Maria and Santa Barbara coastal and offshore areas, in Mackinnon, T.C., ed., Oil in the California Monterey Formation: Fieldtrip guidebook T311: Washington, D.C. American Geophysical Union, p. 11-27.

Montgomery S.L., and Morea M.F., 2001, Antelope shale (Monterey Formation), Buena Vista Hills field: Advanced reservoir characterization to evaluate CO_2 injection for enhanced oil recovery: American Association of Petroleum Geologists Bulletin, v. 85, no. 4, p661-585.

Murata, K.J., and. Larson, R.R., 1975, Diagenesis of Miocene siliceous shales, Temblor Range, California: U.S. Geological Survey Journal of Research, v. 3, p. 553-566.

Murata, K.J., and Nakata, J.K., 1974, Cristobalitic stage in the diagenesis of diatomaceous shale: Science, v. 184, p. 567–568.

Nicholson, C., Sorlien, C.C., Atwater, T., Crowell, J.C., and Luyendyk, B.P., 1994, Microplate capture, rotation of the Western Transverse Ranges, and initiation of the San Andreas transform as a low-angle fault system: Institute of Crustal Studies and Department of Geological Sciences, University of 93106-110, Santa Barbara, California, Geology, v. 22, p. 491-495.

Pisciotto, K. A., 1981, Notes on Monterey rocks near Santa Maria, California: Pacific Section, American Association of Petroleum Geologists, v. 52, p. 73-81.

Pisciotto, K. A., and Garrison, R. E., 1981, Lithofacies and Depositional Environments of the Monterey Formation, California, in Garrison, R. E., and Douglas, R. G., eds., The Monterey Formation and related siliceous rocks of California: Los Angeles, Pacific Section, Society of Economic Paleontologists and Mineralogists, p. 97–122.

Rouquerol , J., Avnir D., Fairbridge, C.W., Everett, Haynes, D.H., Pernicone, N., Sing, J.D.F., and Unger, K.K., 1994, Recommendations for the characterization of porous solids: Pure and Applied Chemistry, v. 66., P. 1739-1758, doi: 10.1351/pac 199466081739.

Schwalbach, J.R., Gordon, S.A., O'Brien, C.P., Lockman, D.F., Benmore, W.C., and Huggins, C.A., 2009, Reservoir characterization of Monterey Formation siliceous shales: tools and applications: Pacific Section, AAPG publication MP48, p. 119-146.

Taylor, J.C., 1976, Geologic appraisal of the petroleum potential of offshore southern California: The borderland compared to onshore coastal basins: United States Geological Survey Circular 730, p. 43.

Tennyson, M.E., and Isaacs, C.M., 2001, Geologic setting and petroleum geology of Santa Maria and Santa Barbara Basins, coastal California, *in* Isaacs C.M., and Rullkotter J., eds., The Monterey Formation-From Rocks to Molecules: New York, Columbia University Press, p. 206-229.

Toronyi, R.M., 1997, Advanced reservoir characterization in the Anthelope Shale to establish the viability of CO2 enhanced oil recovery in California's Monterey Formation siliceous shales: Chevron USA production company, Bakersfield, California, Annual report, 46 p.

Tseng, A.A., 2008, Nanofabrication Fundamentals and application: World Scientific, Arizona state University, USA, 573 p.

Woodring, W.P., and Bramlette, M.N., 1950, Geology and paleoecology of the Santa Maria District, California: U.S. Geological Survey Professional Paper 222, 185 p.